Search for Supernova Relic Neutrino at Super-Kamiokande

Takashi Iida
Department of Physics, School of Science,
The University of Tokyo

December 18, 2009

Abstract

Supernova relic neutrinos (SRN) are the diffuse supernova neutrino background from all the past supernovae. No experiments have succeeded in detecting SRN yet. This thesis describes a search for SRN using Super-Kamiokande (SK), which is a large water cherenkov detecter in Kamioka, Japan.

In 2003, SK published its first result of SRN search using SK-I data with an energy threshold of 18 MeV. This analysis includes 1496 days of SK-I data, 791 days of SK-II data and 548 days of SK-III data. This is the first result of SRN search using SK-II and SK-III data.

We improved the analysis with a detailed investigation of background events and improvement to the event reduction. These improvements enable us to lower the analysis energy threshold to 16 MeV. The combined analysis of the three phase of data taking gives a flux upper limit between < 2.0 - 2.2 /cm^2 /sec ($E_\nu > 17.3$ MeV) for nine SRN models.

Acknowledgments

I am deeply grateful to my adviser, Prof. Masayuki Nakahata giving me the opportunity of studying supernova relic neutrino. I have learned a lot of things under his excellent guidance. This thesis would never exist without his close support and encouragement.

I would like to express my gratitude to Prof. Y. Suzuki, the spokesperson of the Super-Kamiokande experiment. He gave me useful advise related to the experiment and the analysis. I never forget those who worked with me on the analysis, K. Bays and Dr. M. Smy. This thesis would never be completed without their help. I would like to express my great appreciation to Dr. Y. Koshio. I received generous support from him related to the calibration and the analysis.

I am grateful to those who worked for Super-Kamiokande experiment, especially Prof. Y. Takeuchi, Prof. M. Vagins and Prof. S. Moriyama. They gave me a great advise and encouraged me in many cases. I want to thank all the LOWE members, Dr. A. Takeda, Dr. H. Sekiya, Dr. S. Yamada and Dr. B. Yang. I have greatly benefited from them.

I would like to thank to all other ICRR staffs who worked with me, Prof. T. Kajita, Prof. K. Kaneyuki, Prof. M. Shiozawa, Prof. Y. Hayato, Prof. M. Yamashita, Dr. M. Miura, Dr. Y. Obayashi, Dr. J. Kameda, Dr. K. Abe, Dr. H. Ogawa, Dr. K. Kobayashi, Dr. K. Okumura, Dr. S. Nakayama, Dr. C. Saji, Dr. I. Higuchi, Dr. N. Tanimoto, Dr. Y. Shimizu, Dr. H. Kaji, Dr. A. Minamino, Dr. Y. Takenaga, Dr. G. Mitsuka, and Dr. H. Nishino.

I'm also deeply appreciative of my friends who supported me all the time,

M. Ikeda, K. Ueshima, C. Isihara, D. Ikeda, N. Okazaki, T. Tanaka, Y. Idehara, Y. Furuse, K. Ueno, Y. Nakajima, S. Hazama, D. Motoki, Y. Yokosawa T. Yokozawa, Y. Kozuma, H. Nishiie, A. Shinozaki, K. Iyogi, T.F. McLachlan and Maggie.

Special thanks to Dr. J. Raaf, A. Renshaw and Dr. R. Wendell for their useful advices in writing this thesis. I gratefully acknowledge the financial support by the Japan Society for the Promotion of Science.

I would like to extend my gratitude to all the people who supported and encouraged me during my time in graduate school.

Finally, I wish to express my deep gratitude to my friends and family.

Contents

Chapter 1

Physics of Supernova explosion and Supernova Relic Neutrinos

On 23 February 1987, a supernova SN1987A appeared in the Large Magellanic Cloud at a distance of ~ 50 kpc was observed. This was the first observation by naked eye after Kepler's supernova (SN1604). At that time, neutrinos originating from the supernova were also observed at Kamiokande [1, 3], which is the predecessor of Super-Kamiokande, and at IMB[2, 4]. This was the first observation of a stellar object outside the solar system without optical observation method; it was an epoch-making event. Thereby this observation is said to be the birth of the neutrino astronomy.

But supernovae are very rare events which are expected to happen once per several tens of years per galaxy. In this thesis, we focus on the supernova relic neutrinos which originated from all of the past supernovae since the beginning of the universe.

In this chapter, stellar evolution and general physics description of supernovae are presented. Then physics and old experimental results of supernova relic neutrinos will be described.

1.1 Supernova explosion

Supernova explosions are the last stage of stellar evolution of large stars. Heavy elements (above helium) up to iron are generated in the middle stage of stellar evolution and emitted by supernova at the end of the evolution. There are several processes of stellar evolution which depend on the stellar mass as follows.

Figure 1.1: Supernova 1987A happen in Feb. 1987.

1.1.1 Stellar evolution

1. Protostar formation

   The origin of a star starts with the formation of the core by gravitational contraction of interstellar gases. This core becomes larger as more surrounding interstellar matter is absorbed. The kinetic energy of absorbed matter is transformed into thermal energy and therefore the inner pressure of the star starts to rise. If the surface temperature exceeds 2000 degrees, light emission spectrum is in the visible light region and the protostar starts shining. Hydrogen burning starts when the core temperature is over 10^7[K], but a star whose mass is less than $0.08M_\odot$ cannot reach this stage and such a star becomes a planet like Jupiter.

2. Main sequence stars

   In stars larger than $0.08M_\odot$, energy is supplied from hydrogen burning which keeps the inner pressure in a state of thermodynamic equilibrium with gravitation. Although there are several hydrogen burning process, basically it is expressed by equation 1.1.

$$4p \rightarrow^4 He + 2e^+ + 2\nu \tag{1.1}$$

   The Q value for this reaction is 26.73MeV, with the neutrinos carrying $2\times$ 263keV away from the stars, therefore leaving 26.20keV in real thermal energy[1]. Figure 1.2 shows the solar neutrino flux for each reaction mode.

   Temperature and pressure are balanced in the state of hydrogen burning if there is no degeneracy pressure. For example, if the temperature is

[1]This is the case of PP chain I. The energy carried away is different for each reaction mode.

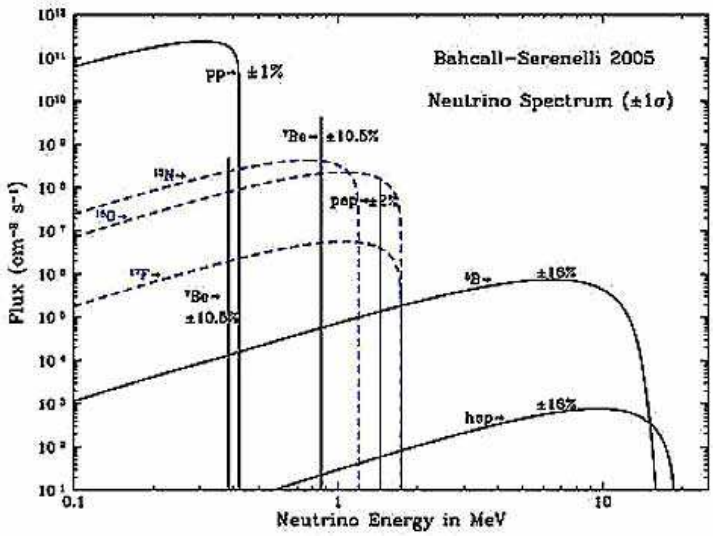

Figure 1.2: Flux of solar neutrino. X-axis is neutrino energy and Y-axis is expected flux in Bahcall-Serenelli 2005 SSM.

changed, the radius of the star is also changed in order to keep dynamical equilibrium, this is called the self stabilization effect. Most stars, including the sun, are in this step, which we call the main sequence. Although PP chain interactions dominate other nuclear fusion process in the sun whose core temperature is 1.5×10^7[K], other more massive, hotter stars can have the CNO cycle as a dominant reaction mode. Light stars, whose mass is less than $M < 0.46M_\odot$, end their life by becoming white dwarves with helium core because they cannot move onto the next step of nuclear fusion.

3. He burning

   Stars with mass greater than $0.46M_\odot$ start to gravitationally contract again once the hydrogen burning has ceased and core temperature then begins to increase. If the core temperature exceeds $\simeq 10^8$ degrees, helium burning is started. There are no stable nuclei in the case of atomic number 5 and 8, so the next step in the nuclear reaction is the process of making ^{12}C from ^4He (α particle) through ^8B nuclear. This process is called the triple alpha process.

$$3^4He \rightarrow^{12} C + \gamma \tag{1.2}$$

$$Q = 7.27\text{MeV} \tag{1.3}$$

   Once helium burning has started, the pressure in the center of core becomes very high. The whole star then expands and the temperature of the stellar penumbra decreases until finally the star becomes a red giant

star. Stars as massive as the solar mass stop their growth, blasting off their penumbra and leaving the core behind to become a white dwarf.

In the case that this helium burning occurs under degenerate pressure, the nuclear reaction burns up. Degenerate pressure does not depend on temperature, so contraction cannot start even after the ignition of helium burning. However, the core temperature will increase even in that case, thus causing the helium burning to proceed explosively. This temperature increase continues until the star is no longer under degenerate pressure. This peculiar process is called helium flash.

4. Heavy ion burning

   Helium burning in stars with masses between $4M_\odot$ and $8M_\odot$ proceeds in the absence of degenerate pressure until the generated C-O core starts burning. Carbon deflagration is caused due to the same principle as helium flash. This is the mechanism of type Ia supernovae.

   More massive stars, $12M_\odot > M > 8M_\odot$, make Ne-Mg cores by carbon burning under the degenerate pressure.

   Stars with mass greater than $12M_\odot$ do not reach degenerate pressure, so finally Mg burning produces an iron core. Iron, ^{56}Fe, is the most stable element; further burning is impossible.

5. End of the massive star

   Core temperature and pressure increase only by gravitational contraction because iron core does not supply energy. At the final stage, the iron core photodisintegration begins and this endoergic reaction accelerates the gravitational contraction. The stars finally end their life with a supernova explosion. Details of the supernova explosion are described in the next subsection.

1.1.2 Type I Supernova

Type I supernovae are distinguished by the lack of hydrogen absorption lines in their spectrum. Type I supernovae can be classified into three different types based on their spectrum. Type Ia include a large Si absorption line. Type Ib can be distinguished by the lack of both hydrogen and Si absorption lines. Type Ic spectra don't have any hydrogen, helium and silicon lines.

Type Ia is caused by carbon deflagration occurring in the condition of degenerate pressure. In the case that the white dwarf of a binary system receives some mass from the other star of the binary system, core collapse starts as long as the white dwarf mass exceeds the Chandrasekhar mass ($1.4M_\odot$). It also causes carbon deflagration and eventually a big explosion. It is by this process which everything gets blown to pieces so that nothing can exist after the explosion. Although type Ia supernovae appear in every type of galaxy (e.g., elliptic galaxies, spiral galaxies, etc.), their rate of occurrence is lower than type II supernovae, which are described in the next subsection.

Because the absolute light intensity of type I supernovae are almost constant, they are called "standard candle" and are used for measurement of the distance to the galaxy including the type I supernova. They also enable us to measure the cosmological constant.

Type Ib and Ic are formed through a different process. They are basically the same as a type II supernova which is caused by core collapse of massive stars. But type I supernovae don't include the hydrogen absorption lines, so the explosion should happen with the outer layer absent of hydrogen. The details of type Ib and Ic are not understood yet.

1.1.3 Type II Supernova

General description of type II Supernova

Type II supernovae are caused by iron core collapse of massive stars whose masses are larger than $8M_{\odot}$. This kind of star can form an iron core as well as burning the silicon at $T \simeq 3.4\times10^{9}$ K. If the mass of the iron core is greater than the Chandrasekhar mass ($M_{ch} \simeq 1.4M_{\odot}$ with $Ye \simeq 0.4$;where Ye is the fraction of the electrons per nucleon), gravitational core collapse and photodisintegration will happen within $\sim$ 10 sec, thus liberating a large amount of energy. Neutron stars or black holes are left after this process.

In the case when a neutron star is left, the released energy from this type II supernova is calculated to be as follows:

$$\Delta E = \left(-G\frac{M^2}{R}\right)_{GScore} - \left(-G\frac{M^2}{R}\right)_{NS} \tag{1.4}$$

$$= 2.7\times10^{53}\left(\frac{M}{M_{\odot}}\right)^2\left(\frac{R}{10\text{km}}\right)^{-1} \text{ [erg]} \tag{1.5}$$

Where GS and NS express giant star and neutron star and the first term is almost negligible.

Meanwhile, the energy expended by photodisintegration is estimated to be less than $1.4M_{\odot} \times 6 \times 10^{23} \times 3.2$ MeV $\simeq 1 \times10^{51}$ erg. The kinetic energy for the ejecta mass of Mej=$10M_{\odot}$ is on the order of E_{kin}=1/2Mej $\times v^2 \simeq 1 \times10^{51}$ erg, assuming v $\simeq$ 2000km/s. Optical energy and gravitational waves also carry away energy smaller than this order. Most of the energy, more than 99%, released by core collapse is carried away by neutrino emission.

To calculate neutrino flux from type II supernova, one may carry out a hydrodynamic calculation with neutrino transport. The core density is $> 10^{13}g/cm^3$, so the core is opaque to neutrino transport. The effective temperature of the core surface is estimated by the radiation law as follows.

$$T_{eff} = \left[\frac{\Delta E/\tau}{4\pi\sigma R_{eff}^2}\frac{1}{(7/8)g_{\nu}}\right]^{1/4} \tag{1.6}$$

where σ is Stefan-Boltzmann constant, g_ν is the number of neutrino species and R $\simeq$ several times 10 km. τ is the cooling time of the core whose order is 5-10 sec. Then the effective temperature is calculated $\simeq$ 4MeV and average neutrino energy $\epsilon_\nu = 3.15T_{eff} \simeq 10$MeV. The total neutrino flux can be estimated as follows.

$$\Phi_\nu = \frac{\Delta E}{\epsilon_\nu} \simeq 2 \times 10^{58} \tag{1.7}$$

Therefore, the neutrino flux of a supernova at the center of galaxy is

$$\phi_\nu = \frac{\Phi_\nu}{4\pi d^2} \simeq 1.6 \times 10^{12} cm^{-2} \ /burst \tag{1.8}$$

From this flux, we expect the event rate in a 1kt water detector for a galactic supernova:

$$\begin{aligned} \bar{\nu_e} \rightarrow e^+ n \ &: 170\text{events} \\ \nu_e \rightarrow \nu_e e^- \ &: 8\text{events} \end{aligned} \tag{1.9}$$

Time evolution of type II Supernova

If the contraction proceeds, the core density will become larger until the Fermi pressure of the electron increases. Large Fermi pressure accelerates the electron capture by iron with a Q value of 3.695MeV. The density threshold of electron capture is $\rho/\mu_e \simeq 0.53 \times 10^9 \mathrm{g/cm}^3$. The state just before core collapse is $\rho_{core} \simeq 10^9 - 10^{10} \mathrm{g/cm}^3$, $T_{core} \simeq 0.7$MeV and the radius of the sphere encircling the Chandrasekhar mass is $\sim$ 3000 km.

Once core collapse starts, free protons are generated by photodisintegration of iron as follows:

$$^{56}Fe + \gamma \rightarrow 13\,^4He + 4n - 124.4\text{MeV} \tag{1.10}$$

$$^4He + \gamma \rightarrow 2p + 2n - 28.3\text{MeV} \tag{1.11}$$

Because this process is an endoergic reaction, contraction of the massive core and electron capture proceed furthermore with free protons (electron capture on free protons has a larger cross section than iron). The number of electrons per nucleon (Ye) decrease by electron capture and it also reduces the Chandrasekhar mass (M_{ch}). The consumed proton is supplied through the photodisintegration process. This process produce a large number of neutrinos whose luminosity is $\simeq 10^{52}$ erg/sec for about $\sim$ 10 msec.

If $R > 10\lambda$, where R is the radius of the core and λ is the mean free path of neutrinos, the core becomes opaque to neutrinos.

A region whose density is larger than $10^{11} \mathrm{g/cm}^3$ forms a neutrino sphere whose radius is $\simeq$ 70km. This neutrino trapping increases the neutrino Fermi

gas pressure, thus electron capture is suppressed. The time scale of this process is about 25 ms.

These process described above cause the decrease of the inner supporting pressure so that core collapse is promoted further and core density becomes larger. Once the core density exceed the nuclear density of 3×10^{14}g/cm^3, the contraction is halted by the degenerated pressure of neutron. The outer core free-falls onto inner core and bound on the surface of inner core and the shock wave propagating outward is generated[6]. The time evolution of stellar shell is shown in Fig1.3.

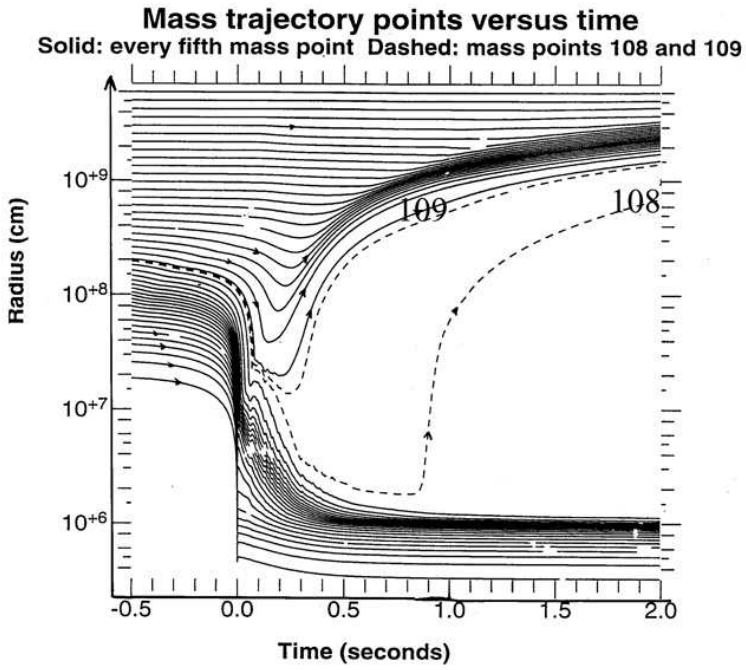

Figure 1.3: Time evolution of stellar shell. 0.0sec is the beginning of free-falling. [13]

Electron neutrinos remain trapped in the neutrino sphere until the shock wave reaches the sphere. Once it reaches, the matter temperature is heated up to T $\sim$ 10 MeV thereby protons and neutrons are liberated. This process promotes the electron capture drastically, generating large amount of electron neutrinos. This is called the deleptonisation burst (or electron neutrino burst) generally. The time scale of the burst is order of 10 ms and its liberating energy is a few times 10^{51} erg [7].

After this degenerate pressure, a shock wave heats the neutrino sphere and then an equal number of all species of neutrinos and anti-neutrinos are generated mainly from neutrino pair creation. Then a protoneutron star is formed, consisting of dense core and mantle, and it cools by emitting neutrino black body radiation in the neutrino diffusion time scale of $\sim$ 10 sec.

After the deleptonisation burst, neutrino luminosity is almost same for all the species of neutrino. The average energy of each neutrino species is:

$$\langle E_{\nu_e} \rangle < \langle E_{\bar{\nu_e}} \rangle < \langle E_{\nu_{\mu,\tau}} \rangle \tag{1.12}$$

where $\nu_{\mu,\tau}$ include their anti particles. $\nu_e\,(n,p)\,e^-$ has a lager opacity than $\bar{\nu_e}\,(p,n)\,e^+$ because neutrons are more abundant than protons. Therefore neutrino sphere of anti-electron is deeper and hotter than that of electron neutrino. Neutrino sphere of muons and tau neutrinos and their anti neutrinos is located still deeper because their interaction is only by a neutral current interaction. Generally the average energy for each species is given as follows:

$$\langle E_{\nu_e} \rangle \simeq 10 - 15\text{MeV} \tag{1.13}$$

$$\langle E_{\bar{\nu_e}} \rangle \simeq 12 - 18\text{MeV} \tag{1.14}$$

$$\langle E_{\nu_{\mu,\tau}} \rangle \simeq 20 - 25\text{MeV} \tag{1.15}$$

These calculations depend on the authors[9, 10, 11]. Time evolution of neutrino luminosity and their average energies are shown in Fig1.4. The sharp peak around 0.05sec is due to electron neutrino from deleptonisation burst. Time-integrated energy spectrum for each species are also shown in Fig1.5

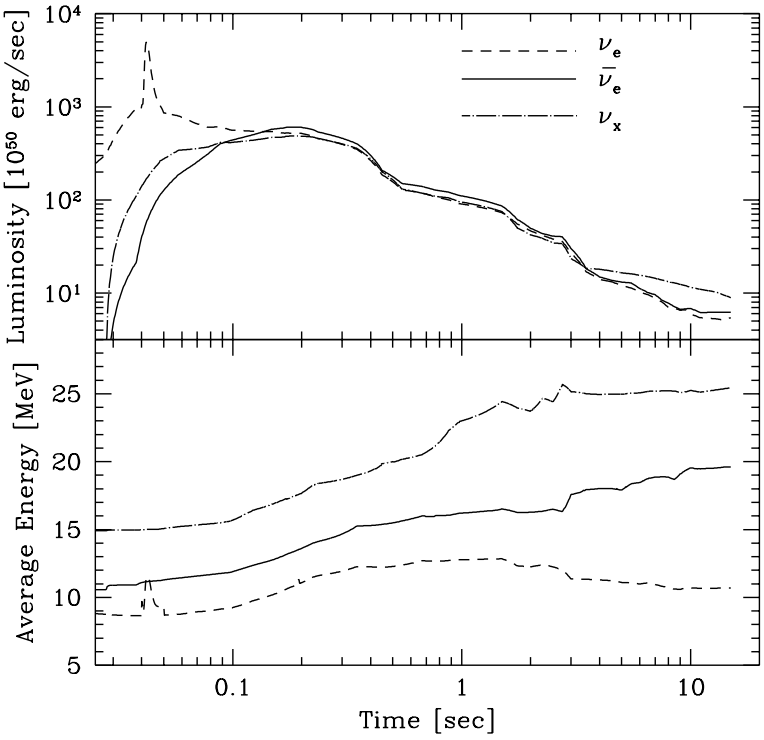

Figure 1.4: Time evolution of neutrino luminosities(upper) and their average energies (lower) [13]

1.2 Supernova Relic Neutrino

Kamiokande detected neutrinos from supernova SN1987A. This enabled us to investigate the mechanism of supernova explosion and also showed that neutrinos can be an effective tool for the space observation, especially for deep inside the stars. But supernovae are quite rare events, said to happen once per several tens of years per galaxy. In this thesis I focused Supernova Relic Neutrinos (SRN), which are the diffuse neutrino background originating from all the past supernova since the the beginning of universe. Measurement of supernova relic neutrinos enable us to know the history of supernova in the whole universe. For example, flux and spectrum of supernova relic neutrinos are related to the history of galaxy evolution and mass distribution in the universe. So the measurement of supernova relic neutrinos is very important for the astrophysics.

In this section, I discuss the supernova relic neutrino itself, followed by a discussion of the detection of SRN in Super-Kamiokande, and finally old experimental results for SRN will be described.

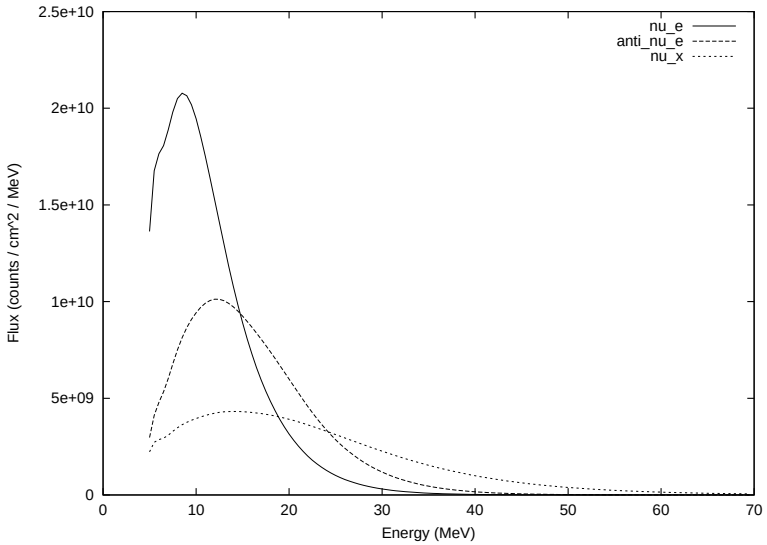

Figure 1.5: Time-integrated energy spectrum for each species

1.2.1 Supernova relic neutrino flux and prediction models

Supernova relic neutrinos are the diffuse supernova neutrino background and their origin is all the supernovae occurring between big bang and present day. Thus their neutrino spectrum is a superposition of the neutrino emission of each supernova explosion. Considering red shift caused by the overall expansion of the universe, we can calculate the SRN spectrum as follows:

$$\frac{dF_\nu}{dE_\nu} = \frac{c}{H_0}\int_0^{z_{max}} R_{SN}(z)\,\frac{dN_\nu\left(E'_\nu\right)}{dE'_\nu}\,(1+z)\,\frac{dz}{\sqrt{\Omega_m\,(1+z)^3+\Omega_\Lambda}} \tag{1.16}$$

where c is the speed of light, H_0 is the Hubble constant, z is the red shift parameter. Ω_m and Ω_Λ are the fraction of the cosmic energy density in matter and dark energy, respectively. R_{SN} is the supernova rate depending on the red shift parameters; at present it is $R_{SN}(0) \sim O(10^{-4})Mpc^{-3}yr^{-1}$. Observations indicate this rate increases with the red shift, it meaning that supernovae occurred more frequently in the earlier universe. The supernova rate depending on the red shift is expressed using $R_{SN}(0)$ and the red shift parameter z.

$$R_{SN}(z) \simeq R_{SN}(0)\,(1+z)^\beta \tag{1.17}$$

The best fit value for β is 3.28 up to red shift z $\sim$ 1 [31] and the rate becomes flat at large z. Fig 1.6 is the evolution of star formation rate density with redshift.

There are several models predicting supernova relic neutrino flux in this way. Even before SN1987A happened, SRN were predicted theoretically [17] and

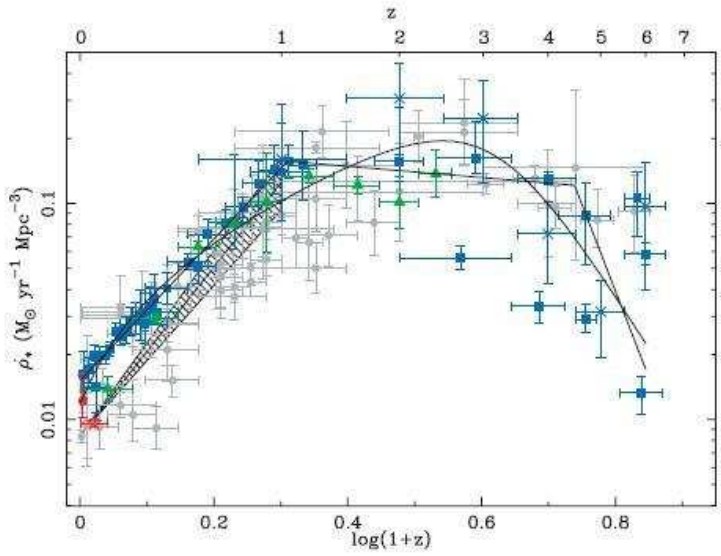

Figure 1.6: Evolution of star formation rate density with red shift. Solid line s are best fitting parametric forms. See [31] for the detail discussion.

the flux was also calculated [18, 19]. The models of an early date are calculated without any experimental data assuming the constant supernova rate. The models after SN1987A calculate the flux and spectrum precisely using advanced theoretical assumptions [20, 21, 22, 23, 24, 25, 26, 27, 28, 29, 30]. The SRN fluxes predicted in these theories range from $\sim 0.3 - 4.6 \bar{\nu_e} cm^{-2} s^{-1}$ above 17.3 MeV. The predicted spectra are shown in Fig 1.7.

- Constant SN rate [20] (Totani et al. 1995)

  An early paper on SRN was published in 1995 by Totani et al. in which the Supernova rate is hypothesized to be constant across all space and time. This model used supernova simulation and considered a cosmological constant for the first time. The absolute flux value was estimated using the abundance of oxygen, because oxygen should be generated in the star which can make the supernova explosion.

- Population synthesis [21] (Totani et al. 1996)

  The same author published another paper in 1996 using a population synthesis in the galaxy evolution. In this paper, the difference of supernova rate between elliptic galaxies and spiral galaxies are discussed and then supernova rate was estimated for each kind of galaxy. Although several cosmological parameters are used in this paper, we take the case of $(h,\Omega,\lambda)=(0.8,0.2,0.8)$ in this thesis. Here h is the Hubble constant, Ω is the density parameter[2] and λ is the cosmological constant.

[2]Ratio of density and critical density

- Cosmic gas infall [22] (Malaney et al. 1997)

  This paper, published in 1997 by Malaney et al., considers the density distribution of interstellar gas for the red shift parameter. Absorption lines of a quasi-stellar objects, QSO, were used. Generally the interstellar gas gets together to make the star and is then returned to the gas through an explosion. But according to this paper, it is only possible for this process to happen in the region z $\leq$ 2 so the flux becomes smaller than other models.

- Cosmic Chemical evolution [23] (Hertmann et al. 1997)

  This model is calculated using chemical evolution of the universe. Galactic halo and chemical evolution information are obtained from the observation of Damped Ly α system (DLA). They are used for the prediction of the global star-formation history. In this paper, they compare several models; for example, one considering time evolution of neutrino energy in the supernova explosion, one changing cosmological parameters, one changing the star formation rate and so on. In this thesis, we adopt the one with $\Omega = 1$ and without time evolution of neutrino energy, called "standard model".

- Heavy metal abundance [24, 25] (Strigari et al. 2004)

  In 2000, Kaplinghat et al. present the paper that predict the theoretical SRN flux upper limit using abundance of heavy elements. The flux prediction is updated in 2004 including the new star formation history from the Sloan digital sky survey. Supernova neutrino spectrum is typically modeled by a Fermi-Dirac spectrum with an effective chemical potential ($\equiv \mu_\nu/T_\nu$). Zero chemical potential and $T_{\bar{\nu_e}}$ are assumed in their paper. Neutrino oscillation effect inside a supernova is also considered with normal hierarchy.

- LMA neutrino oscillation [26] (Ando et al. 2002)

  This model considered the neutrino oscillation inside the stars in order to calculate the flux and spectrum of the SRN. Oscillation parameter used are those obtained from solar and atmospheric neutrino observation. Both SMA and LMA solutions are discussed in this paper but solar neutrino observation has revealed that the LMA solution is correct.

  If oscillation is considered, $\bar{\nu}_{\mu,\tau}$ whose energy is higher than that of $\bar{\nu_e}$, is mixed so the spectrum shifts to a higher region. The cross section of inverse beta decay interaction, discussed later, increase with the square of the energy. Therefore event rate in SK increase if the effect of neutrino oscillation is taken into account. The star formation rate used in this paper was increased by factor 2.56 in 2005 [27].

- Cosmic star formation history [28] (Horiuchi et al. 2008)

In this paper, SRN prediction is started with the cosmic star formation history of Hopkins and Beacom[31] and it's crosschecked by the measurement of core-collapse supernovae[32, 33, 34], the extragalactic background light (which records the total stellar emission overall time [35]), and the stellar mass density [36]. By crosschecking other measurements, the uncertainty of SRN spectrum originating from astrophysical input is found as $\sim \pm 40\%$. As an uncertainty of neutrino emission per supernova, effective temperature of 4, 6, and 8 MeV are adopted. In our analysis, the case of 6 MeV is used.

- Star formation rate constraint [29] (Fukugita, Kawasaki 2003)

  Star formation rate (SFR) is discussed with the old Super-Kamiokande SRN search result[16] in the paper published by Fukugita and Kawasaki. Obtained SFR constraint ($< 0.040\ M_{\odot}\ \mathrm{yr}^{-1}\ \mathrm{Mpc}^{-3}$) is about twice the SFR estimated from radio observations, and five times that estimated from Hα. In this paper, reducing uncertainty in neutrino spectrum was tried using the observation of 1987A neutrinos as a constraint for neutrino energy spectrum[4]. Although the minimum and maximum case are considered from the 90% CL for the IMB events, we took the average of minimum and maximum case.

- Failed supernova [30] (Lunardini 2009)

  This model considers supernova from core collapse with direct black hole formation (failed supernova). According to this paper, the average neutrino energy of a failed supernova is hotter than that of a normal supernova which makes neutron star. Although the fraction of failed supernova is considered as the uncertainty, our analysis adopted 22% case which is largest assumption.

These seven models were used in this thesis when we simulated the spectrum of SRN in SK as discussed later. The predicted SRN fluxes are listed in table 1.1.

1.2.2 Detection of Supernova relic neutrinos

Because Super-Kamiokande is a water Cherenkov detector, neutrinos are detected by their interaction with water molecules. Considering the cross section, the following three interactions are possible. Fig1.9 shows the expected event rate for each interaction mode.

1. Inverse beta decay

   Inverse beta decay is the charged current quasi elastic interaction of anti-electron neutrino on proton:

$$\bar{\nu_e} + p \rightarrow n + e^{+} \tag{1.18}$$

Model	Predicted flux
LMA neutrino oscillation	1.7 $\bar{\nu_e}$ /cm^2/sec
Constant SN rate	4.6 $\bar{\nu_e}$/cm^2/sec
Cosmic gas infall	0.3 $\bar{\nu_e}$/cm^2/sec
Heavy metal abundance	$0.4 - 1.8$ $\bar{\nu_e}$/cm^2/sec
Cosmic Chemical evolution	0.5 $\bar{\nu_e}$/cm^2/sec
Population synthesis	0.54 $\bar{\nu_e}$/cm^2/sec
Cosmic SF history	1.1-1.9 $\bar{\nu_e}$/cm^2/sec
SFR constraint	0.4-1.1 $\bar{\nu_e}$/cm^2/sec
Failed supernova	0.9-1.2 $\bar{\nu_e}$/cm^2/sec

Table 1.1: Predicted flux in each models (our analysis energy threshold of $E_\nu >$ 17.3MeV).

One water molecule has two free protons. An anti electron neutrino can interact with these protons by inverse beta decay and the cross section is largest of the interaction between neutrino and water [20]. In Super-Kamiokande, almost all the detectable events are originating inverse beta decay. In this interaction, emitted positron does not keep the direction information of original neutrino although cross section is very large.

The cross section of inverse beta decay can be simply calculated in first order approximation for $E_\nu <\sim 30MeV$ as follows.

$$\begin{aligned} \sigma &\simeq 9.52 \times 10^{-44} \frac{p_e E_e}{\mathrm{MeV}^2} \quad [\mathrm{cm}^2] \\ E_e &= E_\nu - \Delta \end{aligned} \tag{1.19}$$

Here p_e is the momentum of positron and E_e is the total energy of positron, both in unit of MeV. Δ is the mass difference between neutron and proton and it's about $\sim$ 1.3MeV. So the measurable e^+ energy is strongly correlated with the $\bar{\nu_e}$ energy.

Recently, a more precise calculation was also performed covering the higher energy region[57, 15]. We adopted the one which includes the dominant low energy effects in the calculation, as discussed in [15].

2. Neutral current interaction with oxygen / proton

$$\nu_x + {}^{16}O \rightarrow \nu_x + \gamma + X \tag{1.20}$$

This is a neutral current interaction for all types of neutrinos with oxygen nucleus or proton. In this interaction, the neutrino kicks out a nucleon from the oxygen in water and generate ^{15}O and ^{15}N. Nucleus in an excited state is generated and a gamma-ray of 5 - 10 MeV is emitted

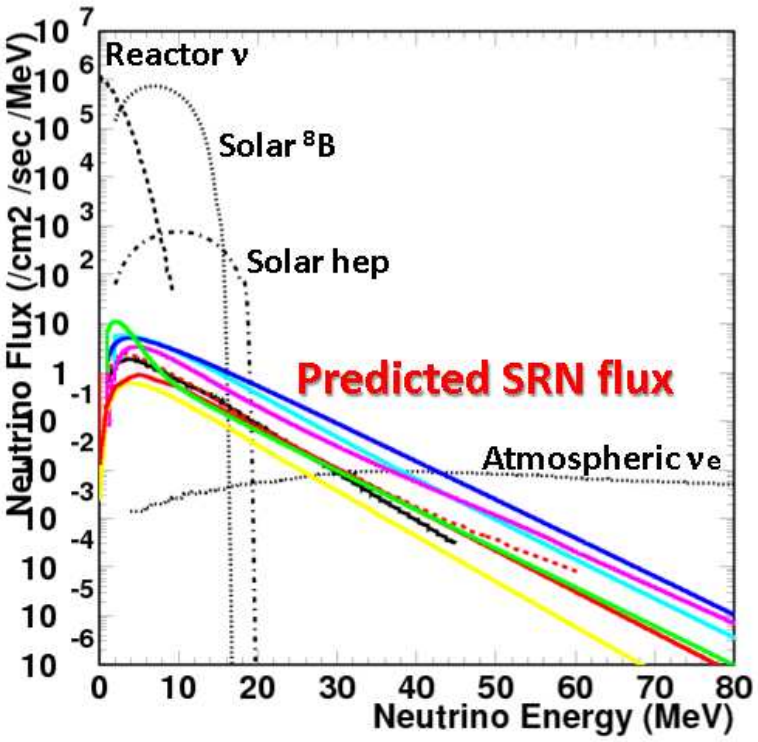

Figure 1.7: Colored line shows the predicted SRN spectrum in each model. Black lines are representing other background neutrinos.

simultaneously. These gamma rays are below our analysis threshold so that they cannot be used for SRN analysis.

3. Electron elastic scattering

$$\nu + e^- \rightarrow \nu + e^- \tag{1.21}$$

This is the neutrino-electron elastic scattering interaction. Recoiled electrons keep the direction information of the original neutrino, but it is not effective for the SRN search because SRN have no specific direction. In addition, the cross section of this interaction is negligibly small comparing with inverse beta decay.

According to the discussion above, the interaction modes other than inverse beta decay of $\bar{\nu_e}$ are negligible for SRN search. The predicted $\bar{\nu_e}$ spectra for theoretical SRN models are shown in Fig1.7. The energy region below $\sim$ 15MeV is not appropriate for SRN search because Solar neutrinos are dominant in this region. Also atmospheric neutrinos are much higher than SRN above several tens of MeV. Thus the search window for SRN is $\sim$ 15 - several tens MeV.

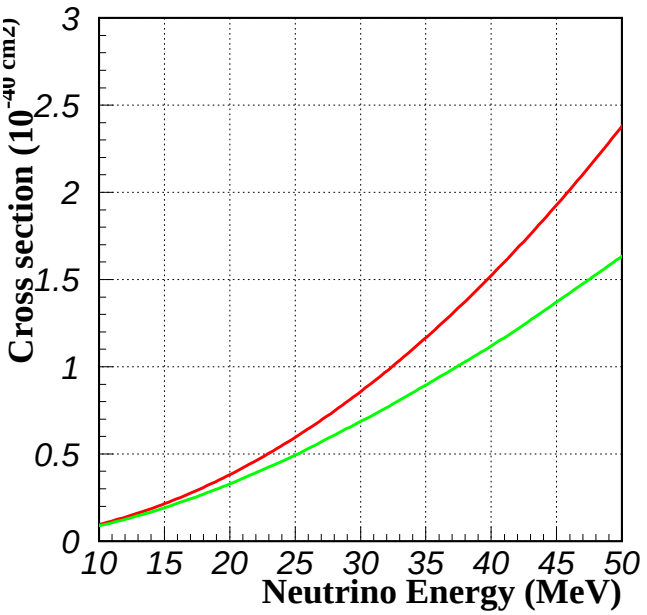

Figure 1.8: The calculated cross section of inverse beta decay as a function of neutrino energy. Red line is approximated cross section in equation 1.20. Green line shows the precise calculation by Strumia and Vissani[15].

1.2.3 SRN search in SK-I and other experiments

Kamiokande

The Kamiokande collaboration published the result of SRN search in 1988 [42]. Kamiokande was a water Cherenkov detector for nucleon decay and neutrino detection. This detector was located at the Kamioka mine at $\sim$ 1000m depth. It consists of a large steel water tank with 3000 tons of pure water and 1000 20-inch PMTs. Its fiducial volume was $\sim$ 680 tons.

Using 357 days of data, the upper limit on the SRN flux in the energy range between 19 - 35 MeV is obtained as 226 /cm^2/sec at 90% confidence level. Additional SRN flux upper limit obtained from 1040 days of Kamiokande-II data was set on the total SRN flux ($<$ 780 $\bar{\nu_e}$/cm^2/sec) [43]. This is corresponding to 50 $\bar{\nu_e}$/cm^2/sec in the energy region above 19 MeV.

SNO

Sudbury Neutrino Observatory (SNO) is a neutrino detector using heavy water; its first motivation is solar neutrino measurement. The SNO detector consist of an acrylic vessel filled with 1 kton heavy water surrounding 10,000 PMTs. Using heavy water, the SNO detector is sensitive to electron neutrinos through the charged current interaction as follows.

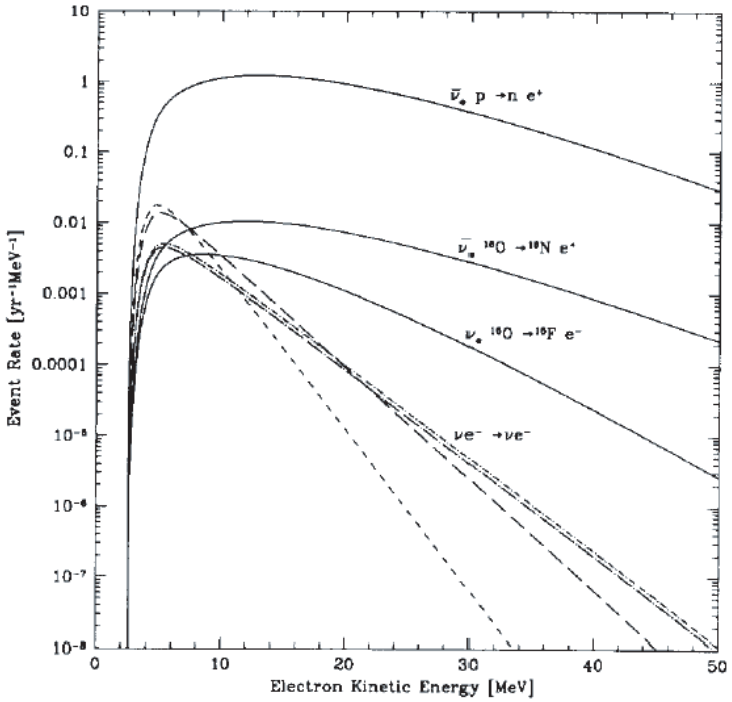

Figure 1.9: Expected event rate for each neutrino interaction modes inside the SK fiducial volume. A constant SN rate model is used for the SRN flux. The event rate of inverse beta decay is higher than that of other modes by two orders of magnitude. [20]

$$\nu_e + D \rightarrow P + P + e^- \tag{1.22}$$

The SNO collaboration published its result for SRN search in 2006 using their first phase data with an exposure of 0.65 $kton - years$ [44]. In their analysis, no events are observed in the neutrino energy range of 22.9 - 36.9 MeV, and consequently, the flux upper limit on the ν_e component of SRN was set to $< 70/\mathrm{cm}^2/\mathrm{sec}$ at the 90% confidence level.

Mont Blanc

The LSD liquid scintillation detector has been operating since 1985 in the Mont Blanc Laboratory. The detector consists of 90 tons of liquid scintillator, contained in 72 stainless-steel tanks and each counter is watched by three PMTs with 15 cm diameter. Since the amount of luminescence of liquid scintillator is large, LSD can detect the gamma-rays emitted by neutron capture so that $\bar{\nu_e}$ event can be separated from other background such as solar ν_e.

Anti neutrino limit flux of $< 8.2 \times 10^3/\mathrm{cm}^2/\mathrm{sec}$ are obtained. with 90% confidence level[45].

KamLAND

KamLAND is a 1 kton liquid scintillation detector located 1000m depth underground in Kamioka, Japan where is the same site as Super-Kamiokande. Because this detector consists of liquid scintillator, the gamma-rays from a neutron capture can be tagged and it enable us lower background rate and lower energy threshold.

The KamLAND result was obtained by searching inverse beta decay event originating from the sun and other sources. This flux limit can be applied for the SRN. From the KamLAND result, SRN flux limit of $\sim 10^2$ $/\mathrm{cm}^2/\mathrm{sec}$ are obtained in the energy region of 8 - 14 MeV[46].

SRN search in SK-I

1496 days of SK-I data were analyzed in the first SK analysis and no clear SRN signal was discovered [16]. Fig1.10 shows the energy spectrum for the real data and expected backgrounds and they are consistent. In the result of that analysis, most strict flux upper limit was obtained. In the energy region, $E_\nu >$ 19.3MeV, SK-I SRN flux upper limit of $< 1.2/\mathrm{cm}^2/\mathrm{sec}$ was obtained for all models and it's close to predicted SRN flux.

Note that this flux limit was obtained using the first order approximation expressed by equation 1.20. This cross section is $\sim$20% larger than latest calculation[15].

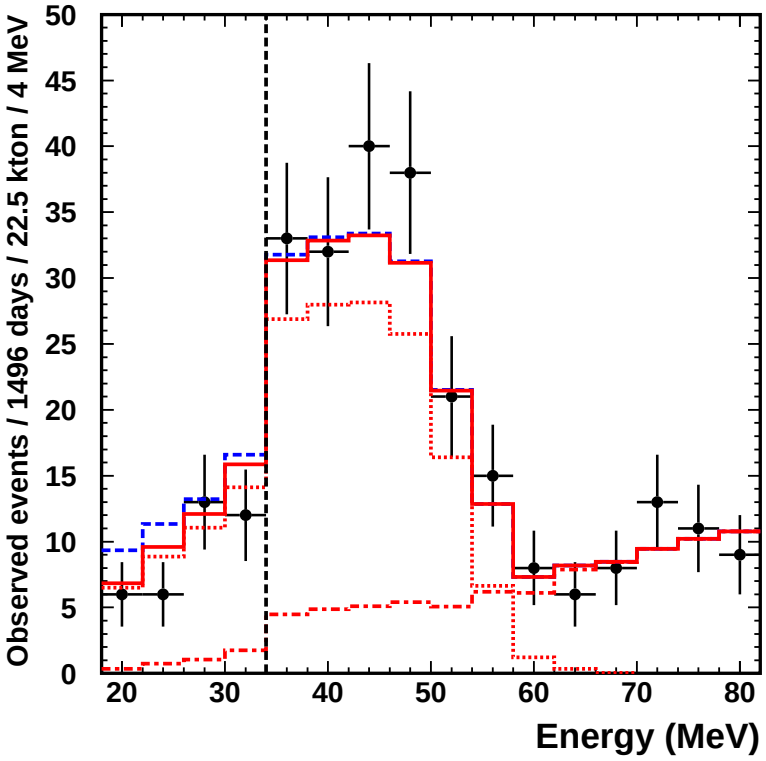

Figure 1.10: Spectrum of SK-I data and background of atmospheric neutrinos. Black points with error bars are data and the red solid histogram is best fit of atmospheric neutrino MC. Red dotted histogram which has a peak around 40MeV is the ν_μ component of atmospheric neutrinos and the other one is the ν_e component. Blue dotted line shows the sum of the total background and the 90% C.L. upper limit on the SRN flux signal.Black dotted line at 34 MeV is a boundary line where the efficiency changes.

Chapter 2

Super-Kamiokande Detector

Super-Kamiokande detector [51] is a 50,000 ton water cherenkov detector for neutrino observation (Kamioka Neutrino Detection Experiment) and nucleon decay (Kamioka Nucleon Decay Experiment) which is located 1000m depth underground of Ikenoyama, Japan as shown in Figure-2.1 in order to reduce cosmic ray muon background. It reduce the cosmic ray muons by 5 orders of magnitude. 50kton of water is filled in 39m diameter and 42m height cylindrical stainless steel water tank surrounded by more than 10,000 20-inch diameter PMTs. In this chapter, the principle of detection, photomultiplier, water tank, pure water system and data acquisition system are described.

2.1 Detection of neutrinos

2.1.1 Cherenkov light radiation

Super-Kamiokande detects relativistic charged particles by Cherenkov light which is emitted when the speed of a charged particle exceeds the speed of light.

When charged particle travels through a medium, charge polarization occurs. The charged particle exchanges photons with surrounding electric field but if the speed of the particle is faster than the speed of light in medium, photons cannot catch up with former particle. Those photons are emitted with the opening angle θ with the following equation. The basic concept of Cherenkov radiation is shown in Figure-2.2.

$$\cos\theta = \frac{1}{n\beta} \tag{2.1}$$

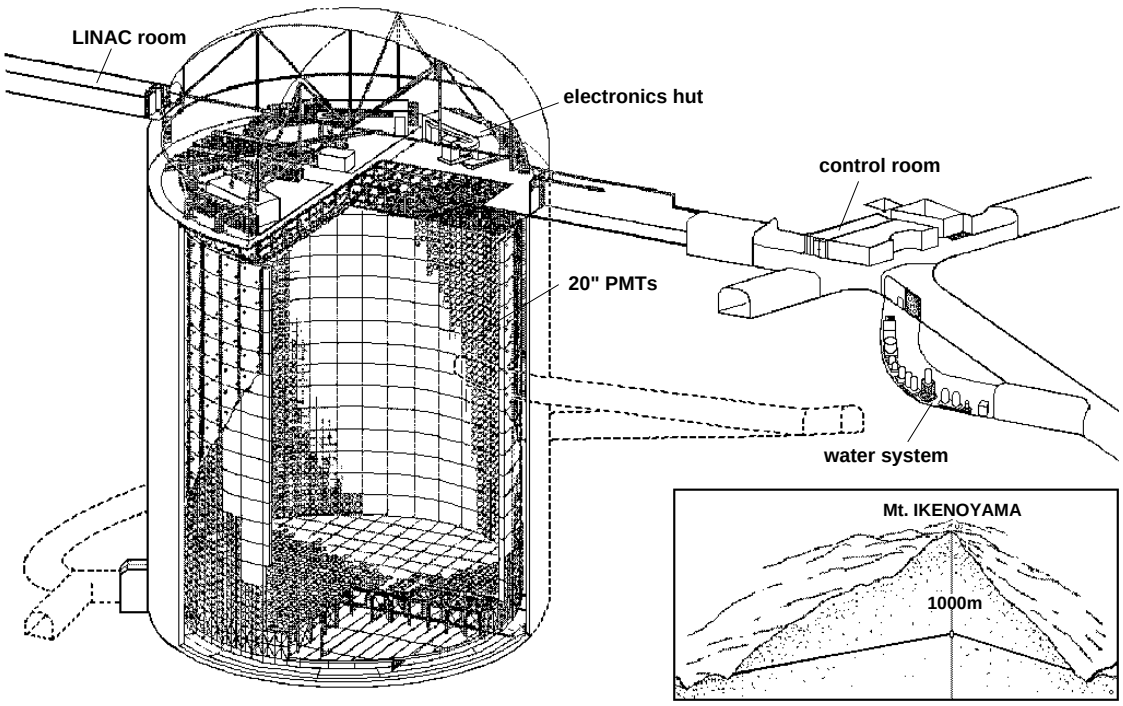

Figure 2.1: The overview of Super-Kamiokande detector.

Here β is v/c. The condition for Cherenkov light emission, $v \geq \frac{c}{n}$, is obtained from Equation-2.1 and $-1 \leq \cos\theta \leq 1$. The energy threshold of Cherenkov light radiation (E_{thr}) corresponds to a lower limit of the speed $\beta = \frac{1}{n}$ and it is expressed using the mass of charged particle m as follows:

$$E_{thr} = \frac{nm}{\sqrt{n^2 - 1}} \tag{2.2}$$

In the case of water, Cherenkov photons are emitted with an opening angle of 42 degrees because the refractive index is about 1.33. Then the Cherenkov radiation threshold, E_{thr}, for electron, muon and charged pion are 0.767, 157.4 and 207.9 [MeV], respectively as shown in Table-2.1.

particle	Threshold [MeV]
$e^{\pm}$	0.767
$\mu^{\pm}$	157.4
$\pi^{\pm}$	207.9

Table 2.1: Cherenkov radiation threshold

The Cherenkov radiation spectrum per unit path length dL can be obtained by following formula:

$$\frac{d^2 N_{photon}}{d\lambda dL} = \frac{2\pi\alpha Z^2}{\lambda^2}\left(1 - \frac{1}{n^2\beta^2}\right) \tag{2.3}$$

where N is the number of emitted photons, λ is wavelength of Cherenkov light and α is the fine structure constant ($\simeq 1/137$). Substituting $\cos\theta = \frac{1}{n\beta}$ for this formula, following equation is given:

$$\begin{aligned} \frac{dN_{photon}}{dL} &= 2\pi\alpha Z^2 \sin^2\theta \int_{\lambda_1}^{\lambda_2} \frac{d\lambda}{\lambda^2} \\ &= 2\pi\alpha Z^2 \sin^2\theta \left(\frac{1}{\lambda_1} - \frac{1}{\lambda_2}\right) \end{aligned} \tag{2.4}$$

Figure-2.3 shows the spectrum of Cherenkov radiation with the quantum efficiency of 20-inch PMTs used in SK. It indicates that the most sensitive region is between $300 \sim 600$nm. $\frac{dN_{photon}}{dL} \simeq 340$ [photon/cm] are emitted within this region with $\theta = 42^\circ$ 、 $Z = 1$.

2.1.2 Detection method

In this section, how the Super-Kamiokande detector detects Cherenkov light and gets the neutrino information is described.

Super-Kamiokande detects the particles which is emitted from the interaction between neutrinos and protons/^{16}O nuclei in water. We get the Cherenkov ring information with photo multiplier tubes (PMTs) placed uniformly surrounding the water tank like Figure-2.4. The event vertex is reconstructed from

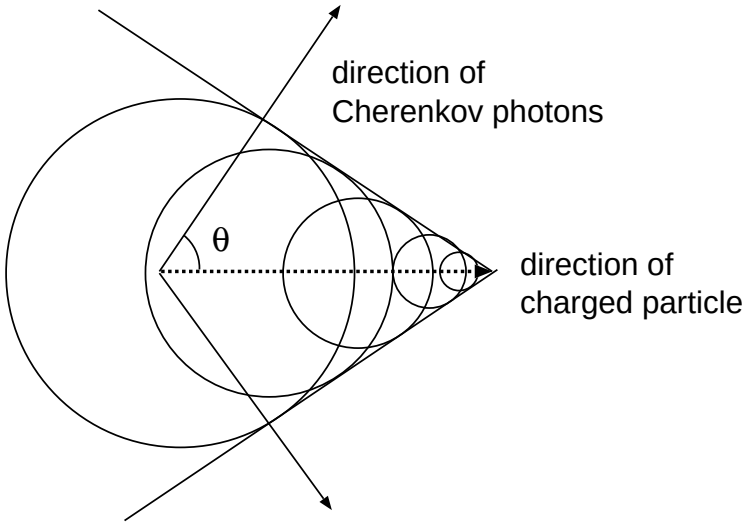

Figure 2.2: Emitted direction of Cherenkov photons.

PMT hit timing information and the energy is reconstructed from the number of hit PMTs. The direction of charged particle is also reconstructed from Cherenkov ring pattern. Details of the detector are described in next section.

2.2 Super-Kamiokande detector

The Super-Kamiokande detector is a large water Cherenkov detector consisting of a cylindrical stainless water tank, 39m radius and 41.4m height, filled with 50ktons of pure water, a purification system for water and air, photomultiplier tubes, electronics and data acquisition system, etc. The detector is located at coordinates of 36° 25'N in latitude, 137° 18'E in longitude and 1000m underground, 2700 meters water equivalence. In order to reduce cosmic ray muons, the detector is located deep underground; the muon rate in Super-Kamiokande is about 2 Hz which is reduced five orders of magnitude compared with that of on surface. Detector construction started from 1991 and completed in 1995. After filling with pure water and test operation, neutrino observation was started from April, 1996.

2.2.1 Inner detector and outer detector

The Super-Kamiokande detector consists of an inner detector (ID) and an outer detector (OD). The ID and OD are separated by an array of steel frames called super module (SM) like figure 2.5. In each SM, twelve 20-inch PMTs are set inward on SM and two 8-inch PMTs are outward on SM. The purpose of the OD is to reduce the γ-ray background from surrounding rocks and to distinguish the cosmic ray muons from neutrino signal.

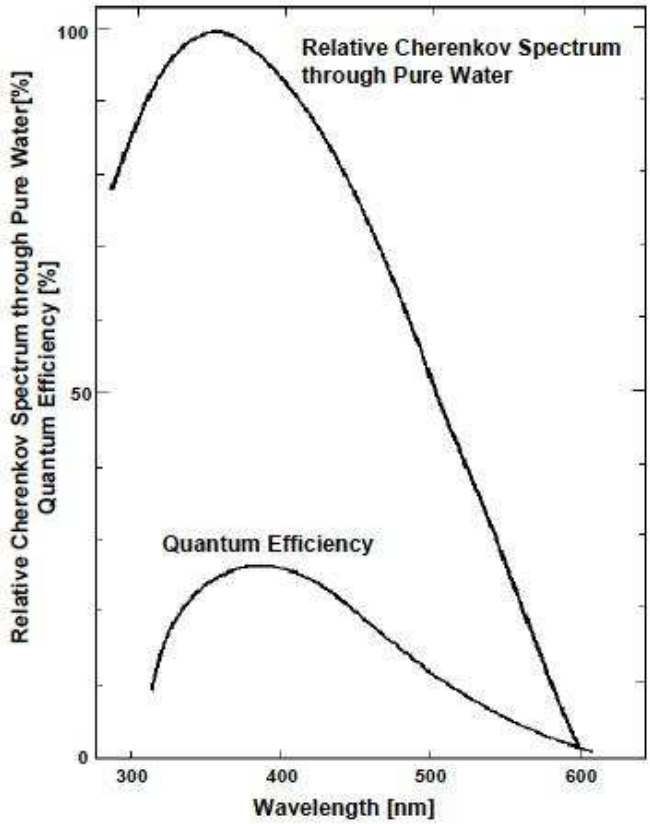

Figure 2.3: The spectrum of Cherenkov radiation and the quantum efficiency of 20 inch PMT

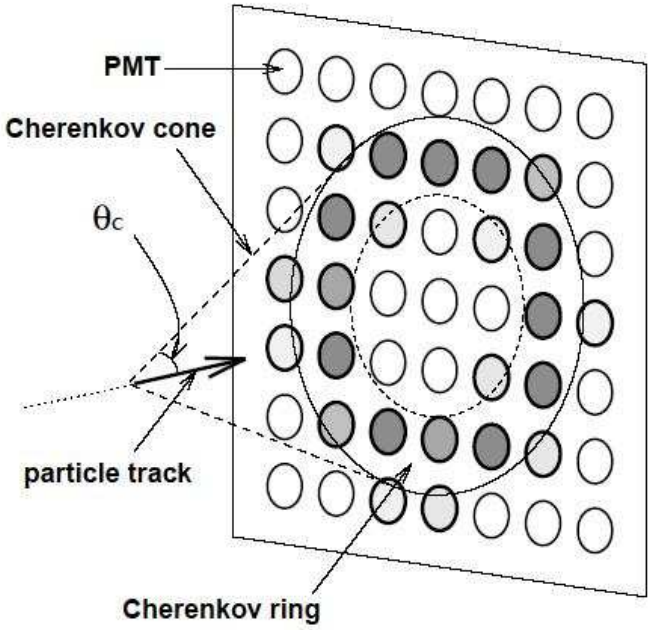

Figure 2.4: Detection method of Cherenkov radiation

8-inch PMTs, Hamamatsu R1408, are used in the outer detector. A 60cm × 60cm wavelength shifter plate is placed around the photocathode of each PMT in order to extend and increase the light collection efficiency. In addition, the OD wall is covered with white tyvek sheet whose reflectance is $\sim$ 80%.

On the other hand, the ID wall is covered with black sheet to prevent a mis reconstruction. 20-inch PMTs are mounted on the ID wall with about 40% photo coverage. This is described in the next section.

2.2.2 20 inch photomultiplier tube

The 20-inch PMT (Figure-2.6) was originally developed by Hamamatsu photonics in cooperation with the Kamiokande collaboration[50]. For the Super-Kamiokande experiment, this PMT was improved in order to achieve better timing resolution and single photo-electron detection. The specifications of the 20-inch PMT are summarized in Table 2.1. The photocathode of the PMT is coated with Bialkali (Sb-K-Cs) so that the sensitive region is 300nm$\sim$600nm and quantum efficiency is maximum ($\sim$22%) at 390nm as shown in Figure-2.3.

The dynode structure was optimized to achieve high collection efficiency which results in a good 1 p.e. distribution and timing resolution. Figure-2.8 shows the charge distribution for the single photo-electron (1p.e.) signal. 1p.e. peak is clearly separated from dark current peak. The average dark rate is

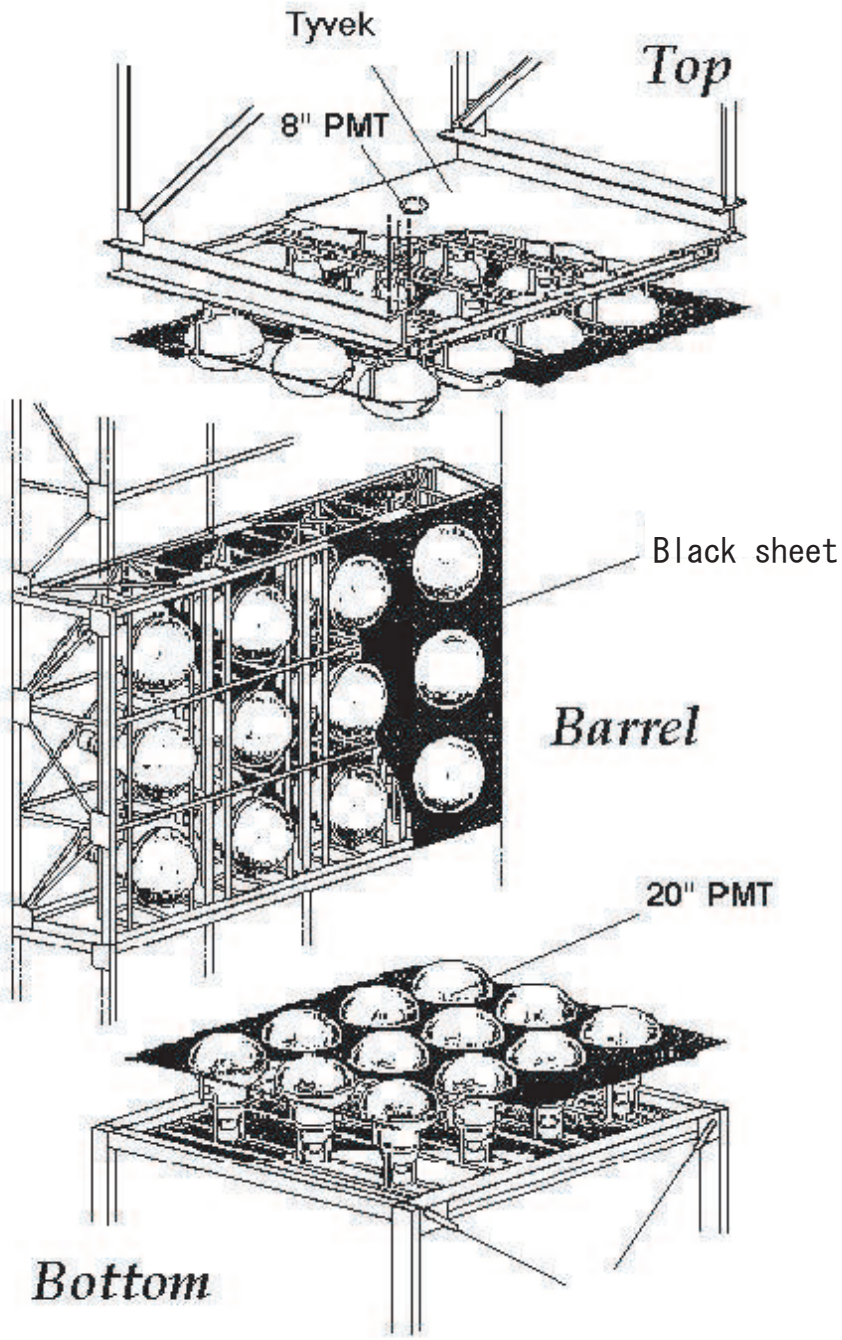

Figure 2.5: PMT frame used in Super-Kamiokande (super module)

about 3.5 kHz at the threshold of 0.3p.e. Timing resolution is about 2.2 nsec as shown in Figure-2.9.

Product name	R3600
Photocathode shape	Hemispherical
Photocathode area	50cm diameter
Photocathode material	Bialkali (Sb-K-Cs)
Dynode	11 stage Venetian bind type
Quantum efficiency	22% @390nm
Gain	10^7 at $\sim$ 2000 V
Dark rate	$3.5kHz$
Timing resolution	2.2ns RMS @1p.e.
Weight	13kg
Pressure tolerance	6kg/cm^2 water proof

Table 2.2: The specifications of the 20 inch PMT

Figure 2.6: 20 inch PMT used in Super-Kamiokande

2.2.3 PMT case

The inside of the PMT is vacuum for preventing discharge and accelerating photo-electrons effectively. Therefore, if the glass tube is broken, it causes a strong shock wave. The accident which occurred in 2001 was caused by chain reaction started from one PMT breakage. In oder to avoid such a cascade of implosions of PMTs, all of the ID PMT are covered by acrylic covers and fiber

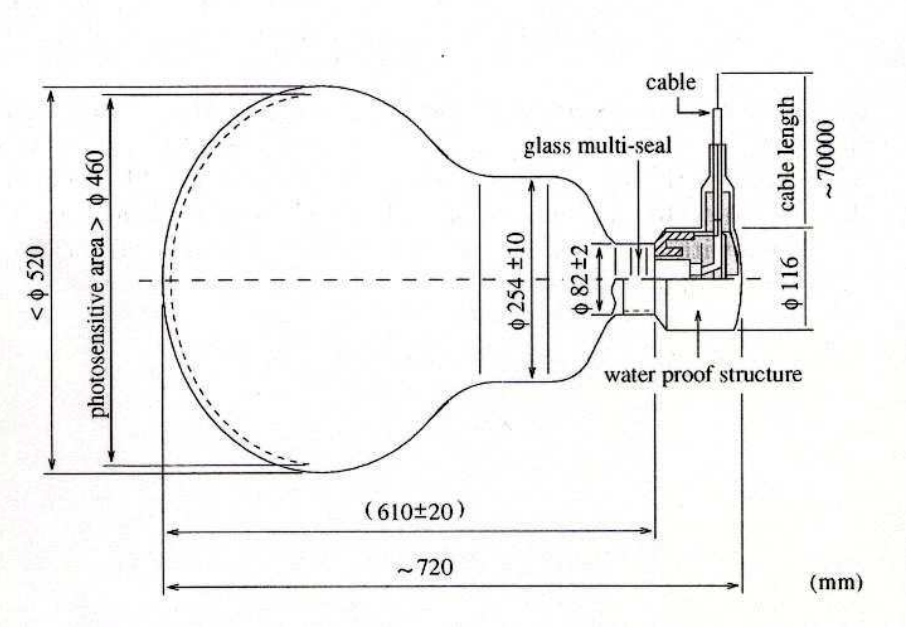

Figure 2.7: The structure of 20 inch PMT

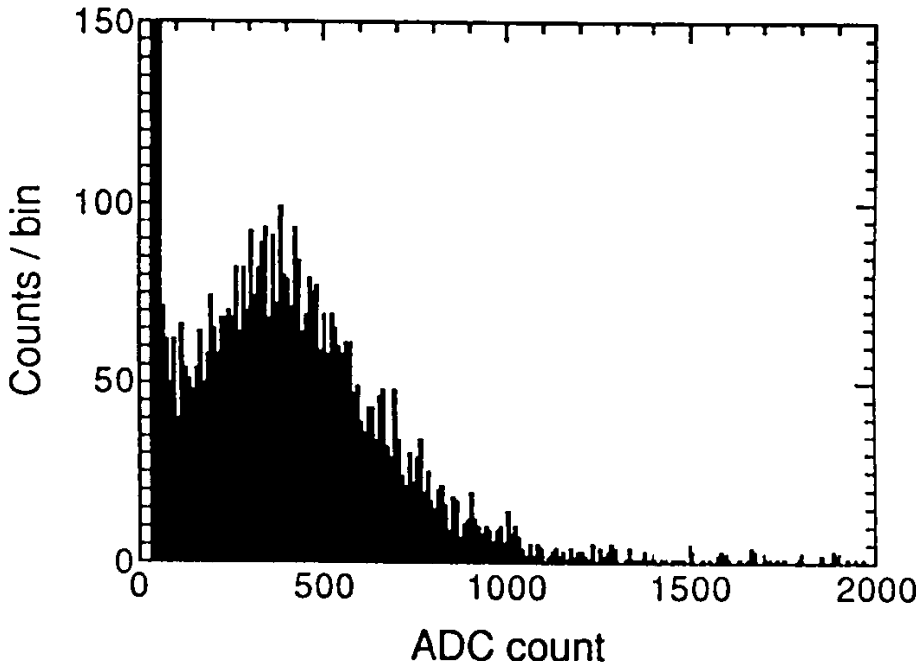

Figure 2.8: The single photo-electron charge distribution of 20 inch PMT

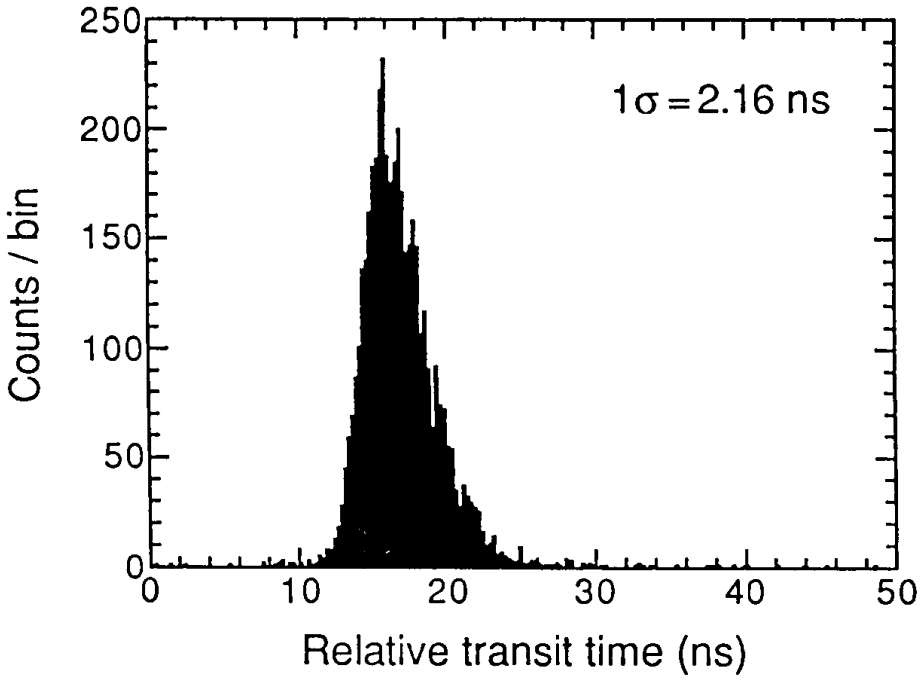

Figure 2.9: The single photo-electron timing distribution of 20 inch PMT

reinforced plastic cases (Figure-2.10) since the beginning of SK-II. Figure-2.11 shows the transparency of the acrylic case as a function of wavelength. It is more than 96% at 350 nm of wavelength. The optical effect of the acrylic cover is confirmed to be small.

2.2.4 Comparison of SK-I, SK-II and SK-III

The main differences of SK-I, SK-II and SK-III are the number of PMTs and PMT cases. In this section, differences in detector configuration are described.

SK-I was started from April, 1996 with 11146 20-inch PMTs ($\sim$ 40% photo coverage). After 5 year of observation, bad PMTs (high dark rate, discharge etc.) were replaced in 2001. After the replacement the accident happened when the tank was being filled with pure water in Novenber, 2001. One of the bottom PMT was broken at that time and 6777 PMTs in the ID and 1100 PMTs in the OD were broken by the chain reaction.

After the accident, all of the PMTs were covered with PMT cases and replaced in the tank. The SK-II period was started from October, 2002 with 5182 ID PMTs which corresponds to photo coverage of $\sim$ 19%.

Full reconstruction took place from July, 2005 to June, 2006 in order to recover the initial photo coverage of PMTs. 11129 PMTs were equipped in the ID tank during the SK-III period. Photo coverage was recovered back to $\sim$ 40% and detector performance, especially energy resolution, was also recovered to

Figure 2.10: PMT case used in SK-II and SK-III

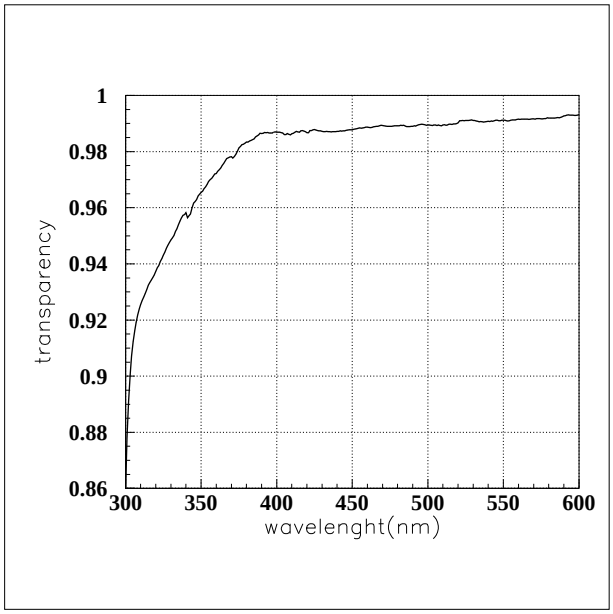

Figure 2.11: The transparency of the acrylic case

the level of the SK-I period. Table-2.2.4 shows the comparison of SK-I, SK-II and SK-III.

	SK-I	SK-II	SK-III
Start of data taking	April, 1996	October, 2002	July, 2005
livetime[1]	1496 days	791 days	548 days
PMT case	No	Yes	Yes
Number of ID PMT	11146	5182	11129
Number of OD PMT	1885	1885	1885
Photo coverage	40%	19%	40%
Energy resolution @10MeV	14%	21%	14%
Position resolution @10MeV	87cm	110cm	87cm
Angular resolution @10MeV	26°	28°	26°
Energy threshold (solar ν analysis)	5MeV	7MeV	4.5MeV

Table 2.3: The features for each phase in Super-Kamiokande

2.3 Water purification system

The 50 ktons of pure water, used in Super-Kamiokande are taken from underground water in Kamioka mine. Small dust, ions, and bacteria are included in the original underground water. These impurities not only shorten the light attenuation length, but also can be a background source for low energy neutrino observation. Therefore, it is crucial to remove impurities from the water as much as possible before filling the detector.

Figure-2.12 is an overview of the water purification system in Super-Kamiokande. The tank water is constantly circulated through the water purification system with a flow rate of about 30 $\sim$ 60 tons per hour. The water circulation process is as follows:

1. Water Filter

   Removes large contaminants ($\sim$ 1 μm) such as dust. ^{222}Rn attached to the dust is also removed.

2. Heat Exchanger

   The water heated by the pumps of the water purification system cause an increase of bacteria. Also, any temperature gradient in the tank may cause strong convection which result in poor water transparency. Water temperature is kept constant after the heat exchanger.

3. Ion Exchanger

   Removes metallic ions (Fe^{2+},Ni^{2+} etc.) using a resin which has ion-exchange group with a 3 dimensional retiform structure.

4. UV sterilizer

   Kills bacteria by irradiating ultraviolet light.

5. Rn-free-air dissolving system

   Dissolves radon free air into the water to improve the radon removal capabilities of the vacuum degasifier.

6. Reverse Osmosis filter

   Filter out dissolved gases and contaminants heavier than mass of 100 molecular weight using a high performance membrane.

7. Vacuum Degasifier system

   Removes dissolved gases (96% removal efficiency for radon and 99% for oxygen) from the water.

8. Cartridge Ion Exchanger

   Further high performance ion-exchange resins selectively remove ions with 99% elimination efficiency.

9. Ultra Filter

   Removes contaminants down to several nanometers using the filter which has a few nanometers hole.

10. Membrane Degasifier

    Further removes dissolved radon and oxygen gases by membrane degasifier.

This water purification system reduces the radon concentration from $10^4 Bq/m^3$ to $10^{-3} Bq/m^3$. The light attenuation length in this pure water is $80 \sim 90m$. It's longer than our detector size of 40m.

2.4 Data Acquisition system

There are central hut and 4 peripheral huts on the Super-Kamiokande tank. The trigger system and control electronics are placed in the central hut, and front-end electronics and high voltage systems are placed in peripheral huts. PMT output signals come to the peripheral hut through a 70m long cable. The analog PMT signal is converted to digital signal by electronics. Two workstations are placed in each hut, which collect data from electronics and send to the host computer in the control room.

2.4.1 Inner detector data acquisition system

Figure-2.14 shows the schematic view of the ID data acquisition system. Output signals from the ID PMTs come into the front-end electronics, called ATM (Analog Timing Module), which were developed based on the TKO (Tristan KEK Online) standard for Super-Kamiokande experiment [47, 48]. Integrated

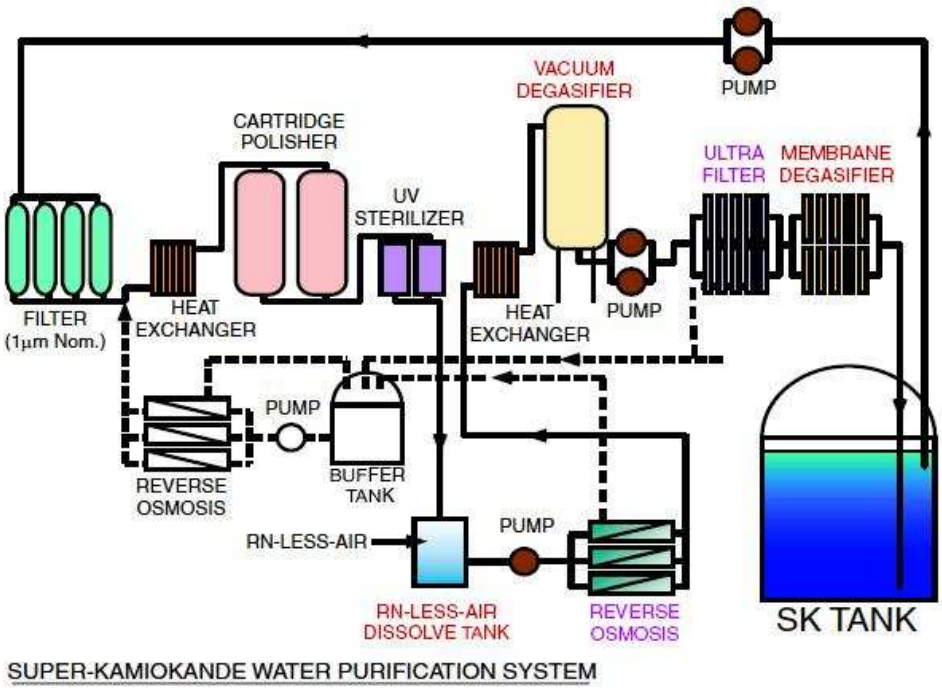

Figure 2.12: Overview of the water purification system in Super-Kamiokande

charge and the arrival time informations are recorded and digitized by the ATM module with a 12-bit ADC (Analog to Digital Converter). One ATM board can treat 12 PMT signals, thus 934 ATM boards are used in total.

The block diagram of the analog input part of the ATM is shown in Figure-2.13. The input signal to ATM is amplified 100 times and divided in the hybrid IC (integrated circuit) as follows.

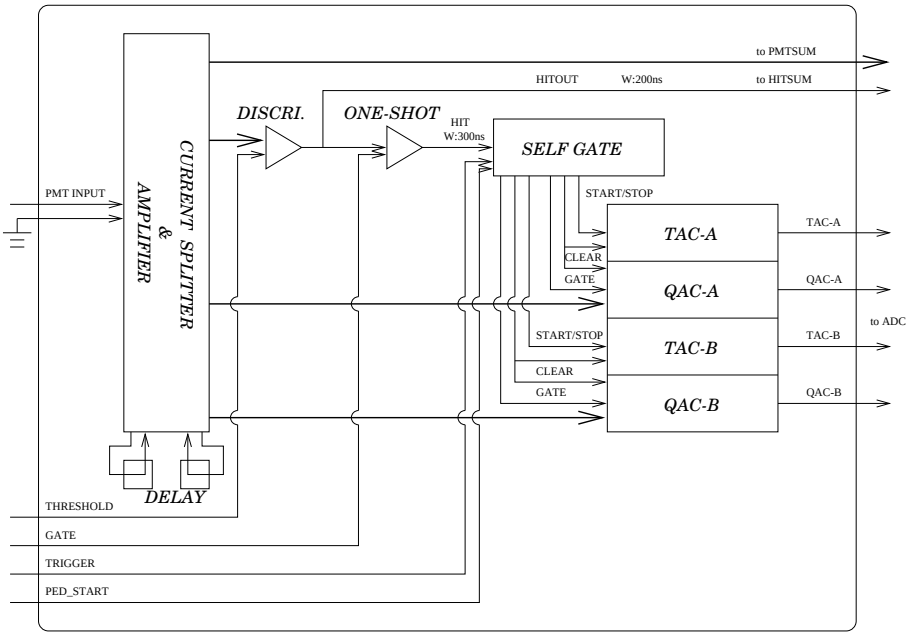

Figure 2.13: The block diagram of the analog input part of the ATM

1. HITSUM

   In the case that the signal from PMT is over the threshold of 0.3 photo-electron, a HITSUM signal, 200 nsec width and -15 mV height, and HIT signal, 900 nsec width and -15 mV height, are output from the front panel of the ATM board. A HITSUM signals are integrated to be used for the global trigger which is the definition of an 'event' in Super-Kamiokande. HIT signals are sent to QAC and TAC through the self gate in order to get charge and timing information of each PMT.

2. PMTSUM

   PMTSUM signal is the sum of input signals for one ATM board. This output signal goes into a Flash ADC that records the waveform information.

3. TAC/QAC

   When the pulse height of the input signal exceeds the threshold, QAC (Charge to Analog Converter) starts integrating the charge for 400 nsec

and TAC (Time to Analog Converter) also starts integrating the charge proportional to hit timing. If the global trigger signal is generated, the TAC stops the charge integration and the integrated charge in QAC and TAC are digitized by the ADC. If a global trigger is not generated within 1.3 μsec, the information in QAC and TAC are cleared. Because it takes 5.5 μsec for ADC to process one channel, each channel of the ATM has two switching pairs of QAC and TAC so that two close events, such as the muon and its decay electron, can be processed.

The digitized signal through the above process is read out by SCH (Super Control Head) and sent to VME memory modules called SMP (Super Memory Partner). The data on SMPs are transferred to online host computer via high speed network.

2.4.2 Outer detector data acquisition system

Figure-2.15 shows a schematic view of the OD data acquisition system [49]. The paddle cards distribute high voltage from the mainframe to the OD PMTs. A coaxial cable is used to supply the high voltage from the mainframe to the OD PMTs. These paddle cards also can receive the PMT signal through a high voltage capacitor.

The signals from the OD PMTs are sent to QTC (Charge to Time Converter) modules which is consist of LeCroy MQT200 chips and comparators. The QTC module converts the PMT signal to a rectangular pulse whose width is proportional to the input charge. At the same time, a HITSUM signal is also generated by the QTC module and sent to the global trigger module. The threshold of the QTC module is same as that of the ATM module. Once the global trigger is generated and received by OD electronics, the leading edge and the width of the rectangular pulse are converted to timing and charge information respectively by the LeCroy 1877 multi-hit TDC module. The TDC module can record 8 QTC signals and its resolution is 0.5 nsec. The digitized data stored in the TDC module are read by a slave computer through a VME memory module, called DPM (Dual Port Memory), and sent to the online host computer.

2.4.3 Trigger system

The HITSUM, 200 nsec width and -15mV height, signal from each PMT is collected at the central hut through a TKO crate, from each electronics hut. If sum of HITSUMs exceeds the threshold, a global trigger is generated. The width of the HITSUM signal is 200 nsec because the event duration time in Super-Kamiokande is up to 200 nsec (in the case of an event which goes through the tank diagonally). A deadtime is produced between 400 nsec and 900 nsec from the HIT signal in order to remove the signal reflection noise (which comes 700 nsec later).

There are three types of global triggers depending on energy: the high energy trigger (HE), the low energy trigger (LE) and the super low energy trigger (SLE).

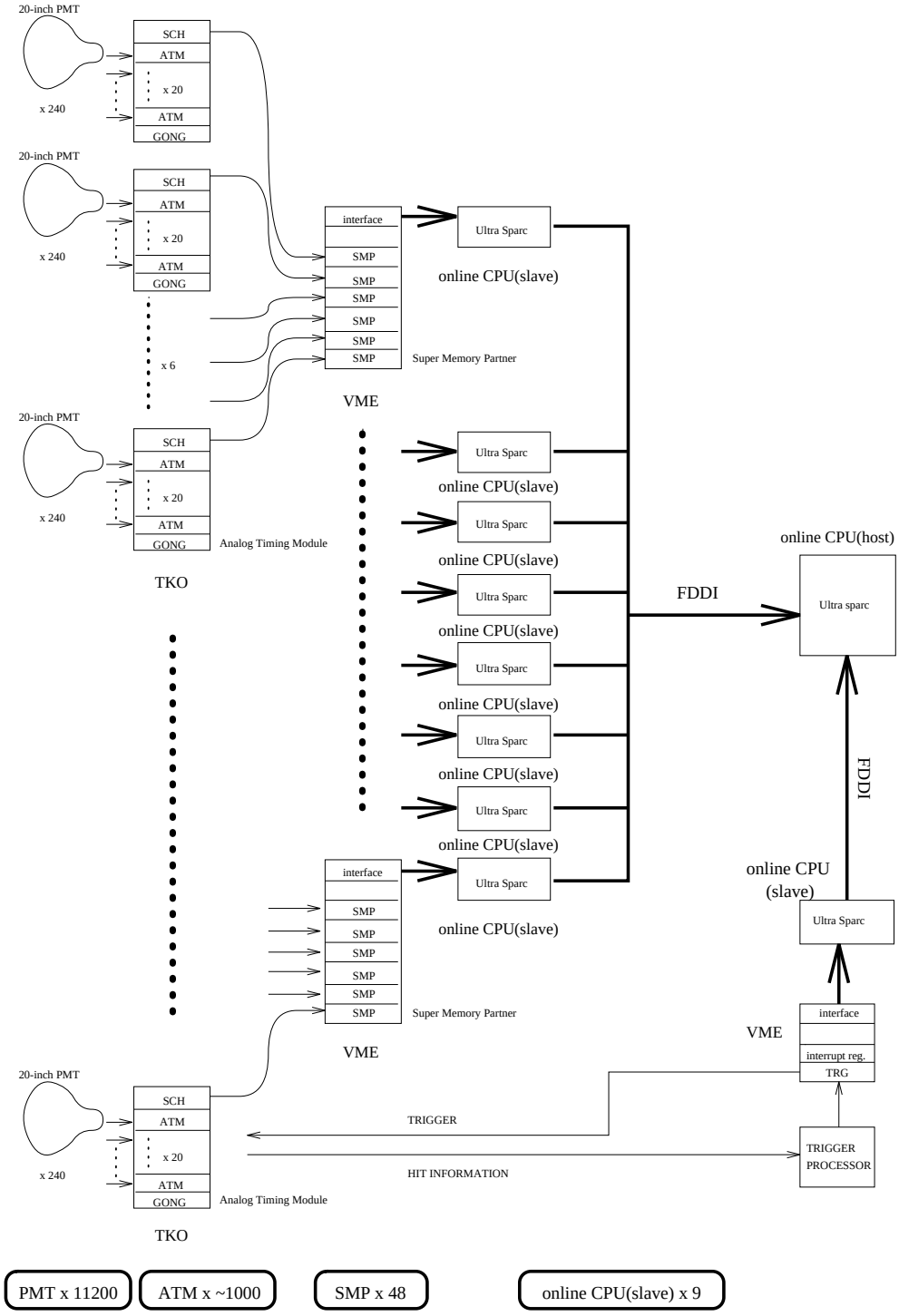

Figure 2.14: Schematic view of ID data acquisition system

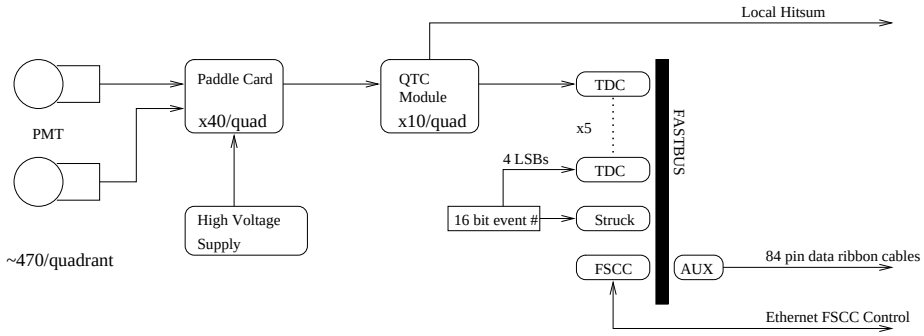

Figure 2.15: The schematic view of OD data acquisition system

At the end of SK-I period, HE, LE and SLE trigger required 34 mV (after 1/10 attenuation), 320 mV and 186 mV respectively. The SLE trigger threshold of 186 mV is equivalent to 4.6 MeV threshold in total electron energy. Each trigger condition in each period are summarized in Table-2.4.

Because of very low threshold, the SLE trigger rate is quite high due to the gamma-ray background from surrounding rocks and PMTs. Therefore, in order to reduce the huge number of SLE triggered events, a software trigger which removes events outside of the fiducial volume, is also applied.

	SK-I	SK-II	SK-III
SLE	186mV	110mV	186mV
LE	320mV	152mV	302mV
HE	34mV	18mV	32mV

Table 2.4: Trigger threshold in each data taking period.

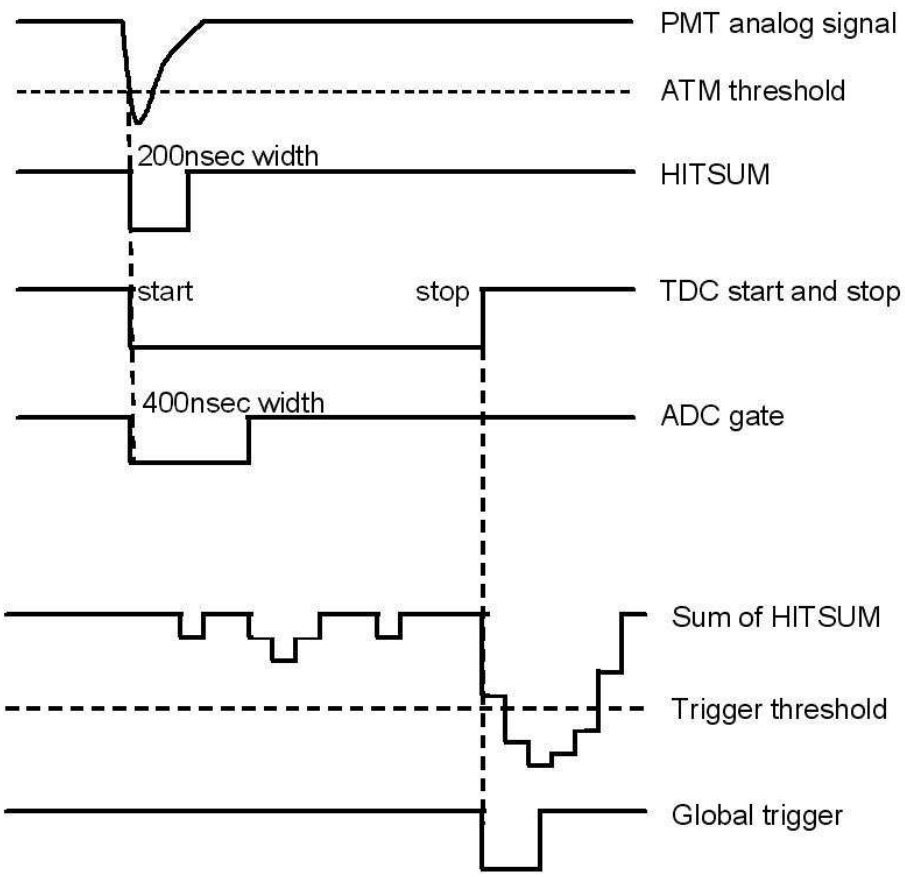

Figure 2.16: The overview of the global trigger generation

Chapter 3

Detector Calibration

Super-Kamiokande consists of 11000 PMTs and 50ktons of pure water for detecting Cherenkov light from charged particle. The particle informations are reconstructed from PMT output, so calibration is very important. Gain and quantum efficiency calibration affects the energy determination and timing calibration affects the vertex reconstruction. We performed a precise calibration on the gain, quantum efficiency (QE), and timing for each PMT individually. Also water transparency measurement is done. In this chapter, details of Super-Kamiokande detector calibration are described. Since calibration methods used in SK-I, SK-II, SK-III are almost similar, in this chapter calibration for SK-III is mainly described.

3.1 PMT HV determination

The gain of PMTs must be uniform in order to achieve a uniform response over the whole SK tank and small systematic error of energy reconstruction. We determine the high voltage value (HV) to be supplied to each PMT using Xe lamp and scintillator ball located in the SK tank.

First of all, we define QE and gain. QE (quantum efficiency) is a probability of photo-electron emission when photon hit the PMT photo cathode. In our definition, CE (collection efficiency), a probability that an emitted photo-electron reaches the PMT dynode, is also included in QE. "Gain" is defined to be an amplification factor in PMT dynodes simply.

We use the output charge of PMT (Q_{obs}) to determine the high voltage (HV). Q_{obs} is defined as follows:

$$Q_{obs}(i) \propto N_{photon}(i) \times QE(i) \times Gain \qquad (3.1)$$
$$i = 1, ..., \quad PMT sequential number$$

where N_{photon} is the number of photons which hit the photo cathode.
The gain of each PMT is given using HV as follows:

$$Gain(i) = \alpha_i \times HV(i)^{\beta_i} \tag{3.2}$$

where α and β is the parameter for each PMT. In our calibration in Super-Kamiokande, we adjusted the HV to give same Q_{obs} for the same N_{photon}.

The SK tank is 40m diameter cylindrical shape and light intensity has ∼20% non-uniformity for Z direction even if we make a perfectly uniform light source. The number of photons that reach each PMT depends on the position of the PMT in the tank. This is a problem when we determine HV value because Equation-3.1 include the number of photons.

To solve this problem we provided "standard PMTs" whose gain is adjusted within a few %. These standard PMTs are located as in Figure-3.4 and the PMTs which have the same geometrical relation to the light source, are grouped. Each PMT gain are determined to the standard PMT gain in its group. In this way, the effect of the asymmetry described above and water scattering can be canceled.

3.1.1 Precise gain adjustment

A schematic view of our setup for the standard PMT calibration is shown in Figure-3.1.

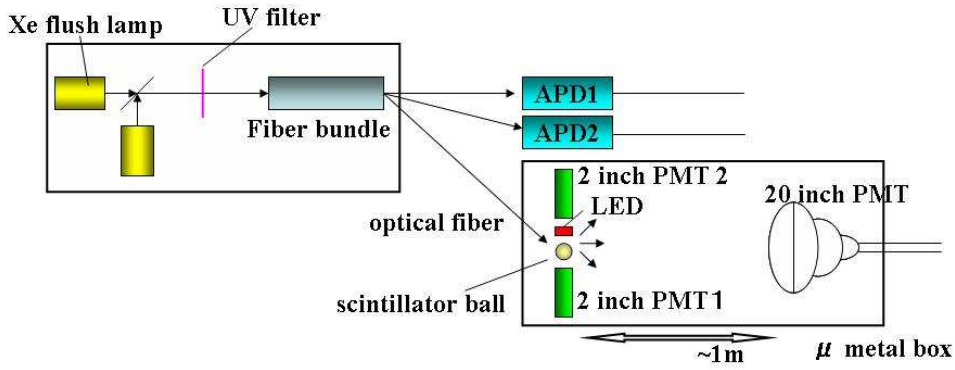

Figure 3.1: The schematic view of our setup for the precise PMT gain measurement. Xe flash lamp are placed inside a box and emitted light input optical fibers through a fiber bundle. Fiber go into the box in which 20 inch PMT is set.

We made 420 standard PMTs using a Xe lamp as the light source. The Xe lamp (L4634-01) made by Hamamatsu photonics is an optimum light source whose instability of output intensity is 5% at maximum and lifetime is 5 $\times 10^8$ flash. Its time constant is 200nsec and light emitting rate is up to 100Hz. Light output from Xe lamp goes through a UV filter which passes only UV light and is then divided into three optical fibers. One goes to the scintillator ball placed in the dark box. The other two fiber go into APD modules, which monitor the

light intensity of the Xe lamp. The scintillator ball include 15ppm of POPOP and 2000ppm of MgO to make the light emission uniform. The dark box which the PMT and scintillator ball are put in is made of μ metal to reduce the effect of geomagnetism to less than 20mG.

Using this setup we adjusted the gain to 10^7 for 420 PMTs. To do this we measured the output charge at four different HV values and determined the parameter α_i and β_i given in Equation-3.2. The output charge is corrected by monitor APD counts and the HV supplied to each PMT is set so that it returns the same output charge within 1%.

As a result, the supplied HV for 420 PMTs are determined with 0.4% RMS. Figure-3.2 shows the ratio between the mean of output charge and target charge of 10^7 gain. To check the reproducibility of our measurement, we selected 50 PMTs randomly from the 420 PMTs and performed the same measurement again. Figure-3.3 shows the result of second measurement. We confirmed good reproducibility with an accuracy of 1.3% RMS.

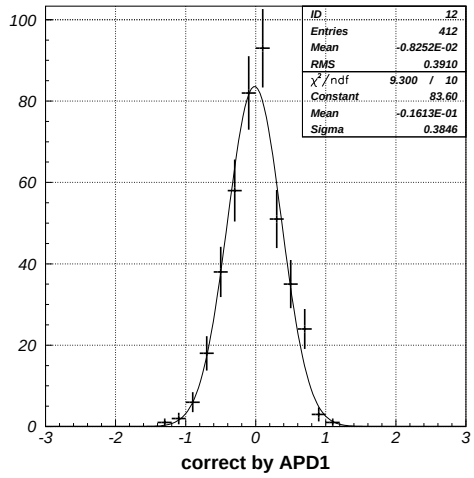

Figure 3.2: Gain dispersion after the HV determination. Applied HV for 420 PMTs are determined within 1%.

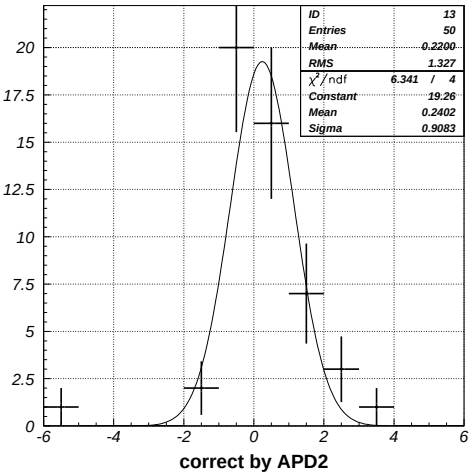

Figure 3.3: Result of the reproducibility measurement in the gain determination. Reproducibility are checked for 50PMTs and confirmed with 1.3% level.

3.1.2 HV determination in SK tank

Here HV determination in SK tank using standard PMTs whose gain are adjusted within 1% is described.

Setup for HV determination in SK

The standard PMTs are mounted in SK tank as shown in Figure-3.4. The scintillator ball, which is the light source of our calibration, is placed at the

tank center. PMTs are grouped depending on their geometrical groups with the scintillator ball. All the 11129 PMTs are divided into 17 groups for barrel PMTs and 8 groups for top and bottom PMTs, as shown in the Figure-3.5. Each group includes 9 - 12 standard PMTs.

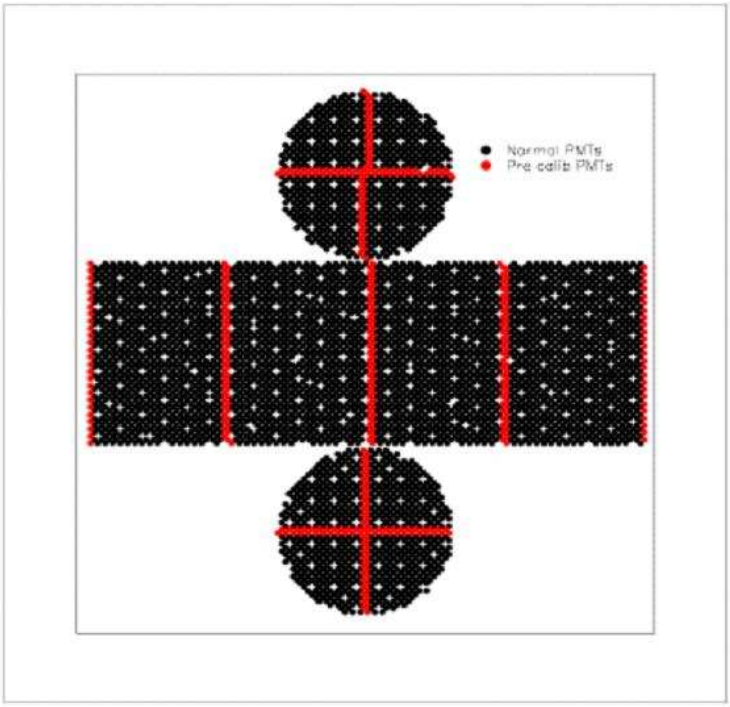

Figure 3.4: The standard PMT setup inside SK tank. The standard PMT setup inside SK tank are shown. Red points are representing standard PMTs.

Figure-3.7 shows a schematic view of the HV determination calibration system. Light emitted from the Xe lamp goes into the scintillator ball at the SK tank center through the UV pass filter. The scintillator ball diffuses input light uniformly and the observed photo-electrons in each PMT are around 50p.e in this system. Another optical fiber goes to a monitor PMT and generates a calibration trigger.

Result of HV determination

The measurement is performed several times, rotating the scintillator ball to cancel the ball non-uniformity. Observed charge is corrected by the distance from the ball to PMT and acceptance as follows:

$$Q_{corr} = \frac{Q_{obs} \times r^2}{f_{accept}(\theta)} \tag{3.3}$$

Mean of Q_{corr} is calculated for all of the PMT and supplied HV is determined

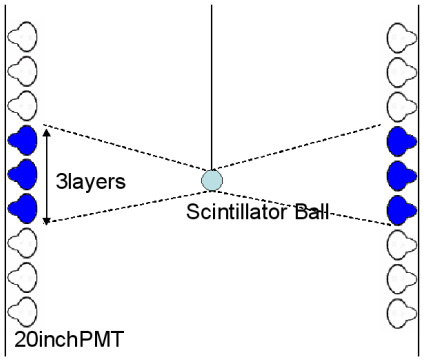

Figure 3.5: Definition of PMT grouping method (Barrel). Barrel PMTs are grouped for three layer; there are 17 groups.

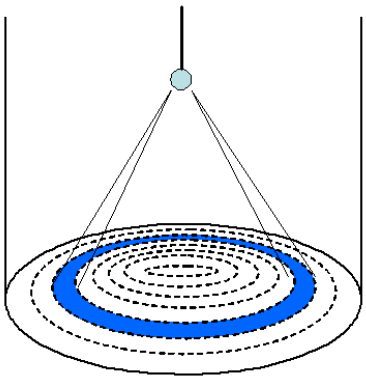

Figure 3.6: Definition of PMT grouping method (Top, Bottom). Top (Bottom) PMTs are grouped by distance from tank center; there are 8 groups for each.

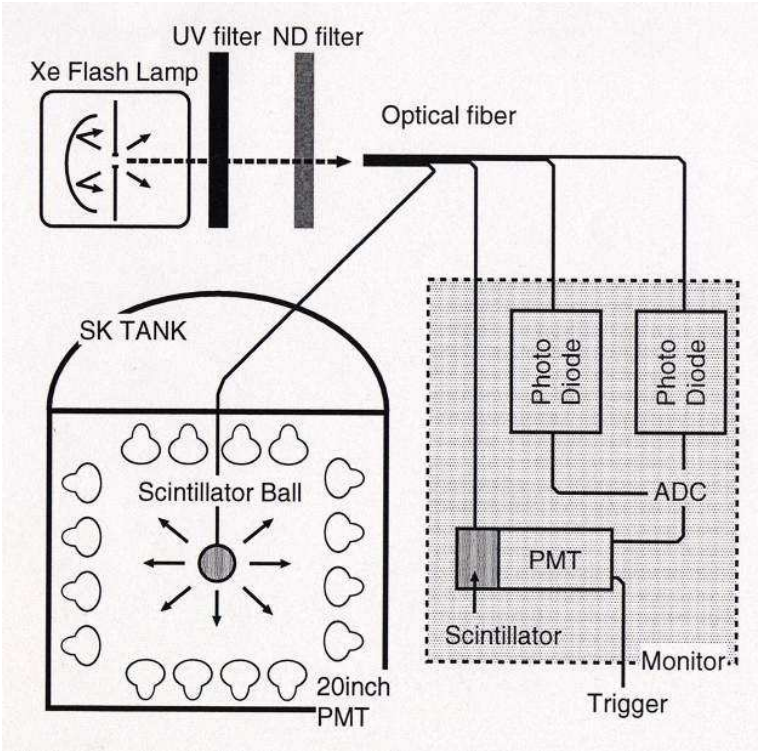

Figure 3.7: A schematic view of the setup for gain calibration using Xe lamp. Same tools as standard PMT calibration are used in this setup.

to make Q_{corr} equal to the Q_{corr} mean of the standard PMTs in each group (target charge). After HV determination, output charge relative to the mean of the standard PMT is measured for all PMTs. Figures-3.8 and 3.9 shows the ratio between Q_{corr} and its target charge.

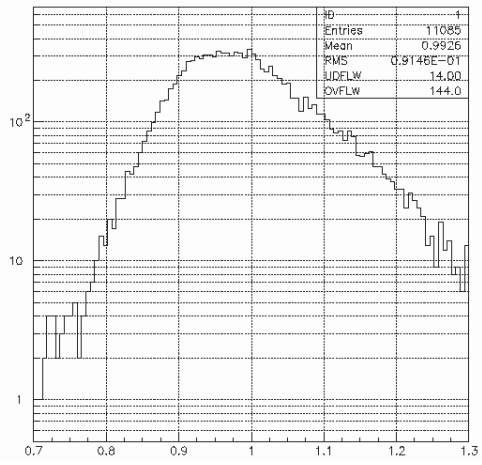

Figure 3.8: The difference from target charge output before HV determination. The distribution has a width of 9% RMS.

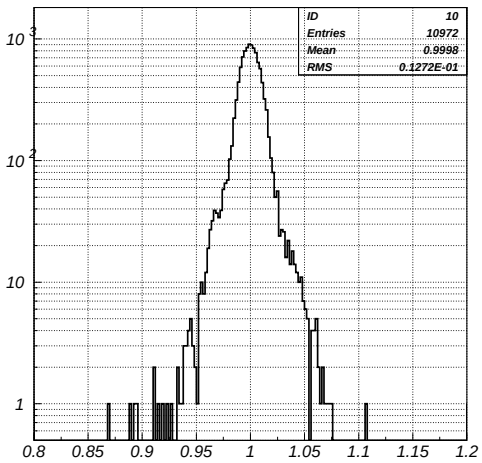

Figure 3.9: The difference from target charge output before HV determination. The distribution has a width of 1.3% RMS.

As a result, the relative output charge can be adjusted to within 2% in SK-II and SK-III, though it was ∼9% before HV determination. Since we don't have precalibrated PMTs in SK-I, data were taken by changing the light source position to reduce the effect of a difference of acceptance for each PMTs. Using this method, the gain spread in SK-I was 7%.

3.2 QE measurement

The quantum efficiency (QE) is different for each PMTs. Especially the PMTs used in SK-II have an asymmetry between top and bottom due to manufacturing term. Especially for low energy analysis, since we use the number of hit PMTs for energy determination, this effect is quite important. We need to measure the QE value for individual PMTs and its difference must be corrected to reduce the systematic error due to top-bottom asymmetry.

Ni-Cf light source

For the light source of QE measurement, we used a radio isotope make from Ni and ^{252}Cf as a gamma-ray source. As shown in Figure-3.10, the ^{252}Cf source is put in the center of the vessel. This vessel has a cylindrical shape

with 20cm height and diameter and it is filled with Ni wire and water. ^{252}Cf causes α decay (97% branching ratio) or spontaneous fission with a lifetime of 2.645 years. When a spontaneous fission occurs, 3.8 neutrons are emitted on the average. Emitted neutrons are captured by surrounding Ni wire after it is thermalized by water in $\sim 200\mu$sec and gamma-rays with 6 - 9MeV are emitted. These gamma-rays give their energy to electrons in water by Compton scattering with a typical scattering length of $\sim$ 50 cm. The electron emits Cherenkov light if its energy is above Cherenkov threshold. The light intensity at each PMT is 0.004 p.e/PMT so that more than 99% of observed light is due to a single photo-electron origin. We used this light source for the QE measurement and absolute gain calibration.

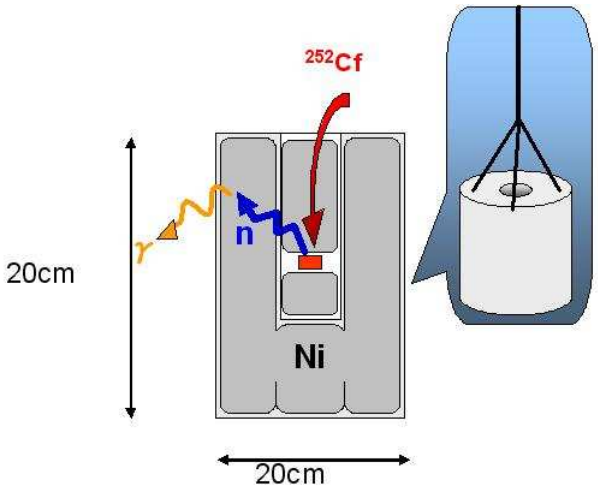

Figure 3.10: A schematic view of Ni-Cf gamma ray source.

Result of QE measurement

The number of hits in each PMT is given by the following like Q_{obs} given in Equation-3.1:

$$Nhit(i) \propto N_{photon}(i) \times QE(i) \tag{3.4}$$

We can measure the relative QE value by measuring the number of hit for each PMT and correcting for the geometrical effect on number of photons. The one dimensional distribution of measured QE is shown in Figure-3.11. Figure-3.12 shows the position dependence of QE measurement. The QE value has a $\sim$ 7% dispersion throughout the SK tank and there is a top-bottom asymmetry due to their manufacturing term as described before.

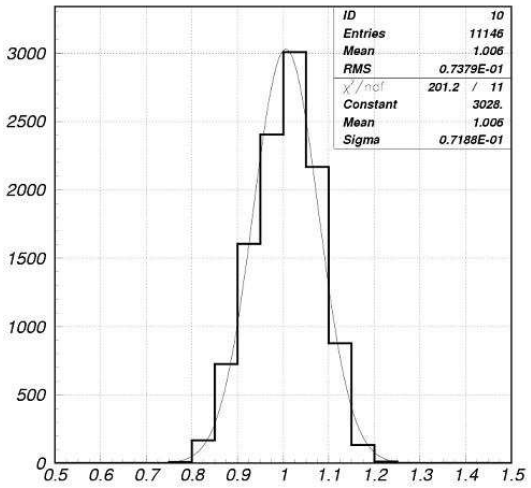

Figure 3.11: The distribution of measured QE for each PMTs

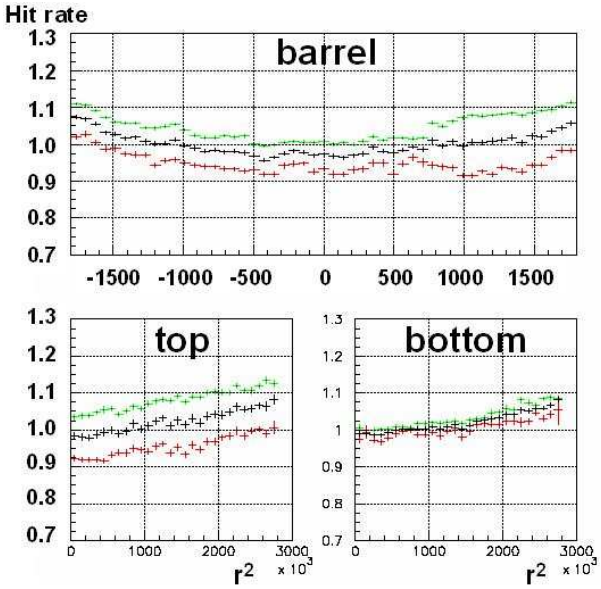

Figure 3.12: Position dependence of QE. Red is for the PMT used in SK-II, Green is the PMT newly added in SK-III and Black is for all

3.3 Absolute gain measurement

PMT gain can be expressed as the product of global gain of the SK detector (conversion factor from photo-electron to pC) and a relative gain of each PMTs like in Equation-3.6. They were measured individually in Super-Kamiokande.

$$Gain = global\ gain \times relative\ gain(i) \qquad (3.5)$$
$$i = 1, ..., \quad \#\ of\ PMT$$

Using the same Ni-Cf light source as for QE measurement, we measured the absolute gain in Super-Kamiokande. The mean of the 1p.e. charge distribution was used to obtain an absolute gain. Figure-3.13 shows the charge distribution for SK-II and SK-III PMTs. As shown in this figure, SK-III PMT which were newly mounted at the beginning of SK-III (SK-III PMT) have lower gain than PMTs that were used during SK-II period (SK-II PMT). This is caused by the effect of QE difference between SK-II and SK-III PMT. It clearly appears also in the relative gain measurement as described later.

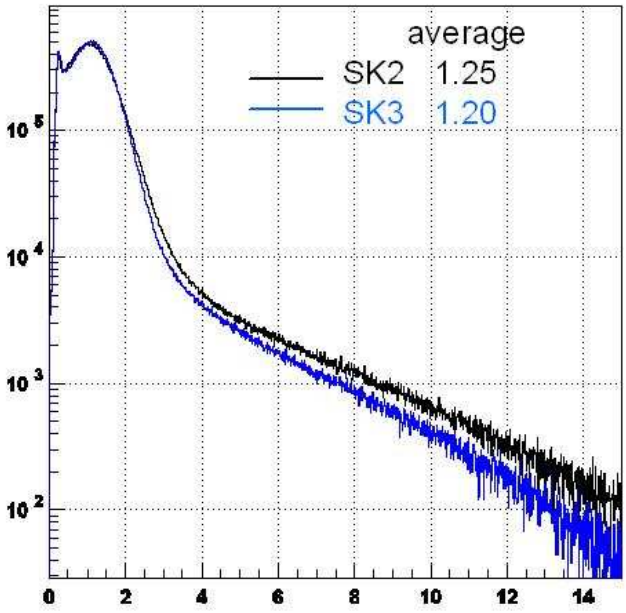

Figure 3.13: Measured charge distribution from Ni calibration. Horizontal axis is number of photo-electrons. Black is SK-II PMT and Blue is SK-III PMT.

From the mean of 1p.e. charge distribution, we obtained charge to photo-electron transformation factor for all three phase of SK and they are shown in Table-3.1.

SK phase	Absolute gain [pC/p.e.]
SK-I	2.055
SK-II	2.297
SK-III	2.243

Table 3.1: Charge to count transformation factor obtained from absolute gain measurement using Ni source in each SK data taking phase.

3.4 Relative gain measurement

From the 1p.e. measurement by Ni-Cf source, absolute gain was obtained but it's not for individual PMT. So we measured the relative gain for all ID PMTs and made the correction table. This value should have inverse correlation with QE according to Equation-3.1.

3.4.1 Method and setup for relative gain measurement

According to Equation-3.1 and Equation-3.4, we can get the relative gain by taking a ratio between Q_{obs} and N_{hit} as follows.

$$\frac{Q_{obs}(i)}{N_{hit}(i)} \propto gain(i) \tag{3.6}$$

We took the data for this measurement using laser with two different light intensity (Figure-3.19). Using exactly same setup except light intensity and taking ratio, all the effect, e.g. water transparency and magnetic field, can be canceled.

The result of relative gain measurement is shown in Figure-3.16. As seen in this figure, RMS of relative gain is 5.9%. Position dependence of relative gain is shown in Figure-3.15. Top SK-II PMT have higher gain than bottom SK-II PMT because of QE difference.

3.5 Timing calibration

The relative timing calibration is essential for the vertex reconstruction of SRN candidates. Ideally timing response of each PMT are same after subtracting time-of-flight from the vertex position to each PMT. However there are difference of PMT response due to the length of the PMT signal cable and the response time of electronics. The effect of the electronics depend on a detected charge because of the time-walk effect of discriminators [1] as shown in Figure-3.18.

A laser calibration system, shown in Figure-3.17, is used for the timing calibration in Super-Kamiokande. N_2 laser generate the high intensity light

[1]The PMT that are exposed to larger light intensity exceed their discriminator threshold sooner. This is called "TQ-map"

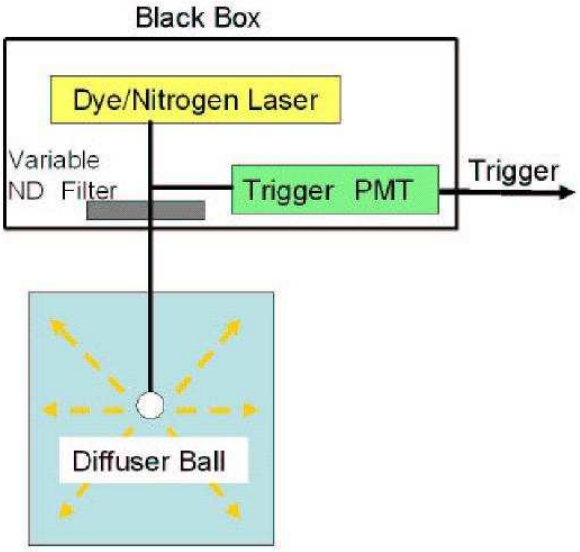

Figure 3.14: A schematic view of the laser calibration setup for relative gain measurement.

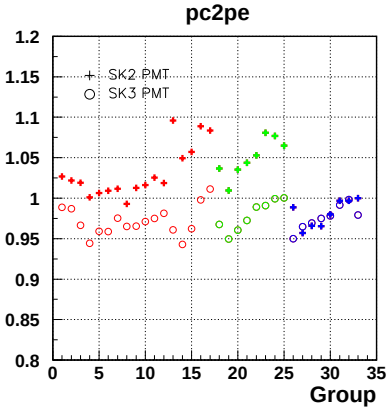

Figure 3.15: An average of measured relative pc2pe value in each group + : SK-II PMT、○ : SK-III PMT Red : Barrel, Green : Top, Blue : Bottom

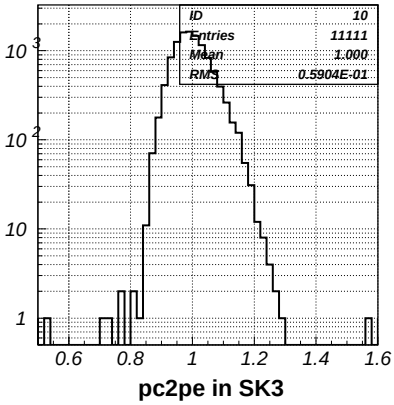

Figure 3.16: relative gain distribution. Mean value of this distribution is one.

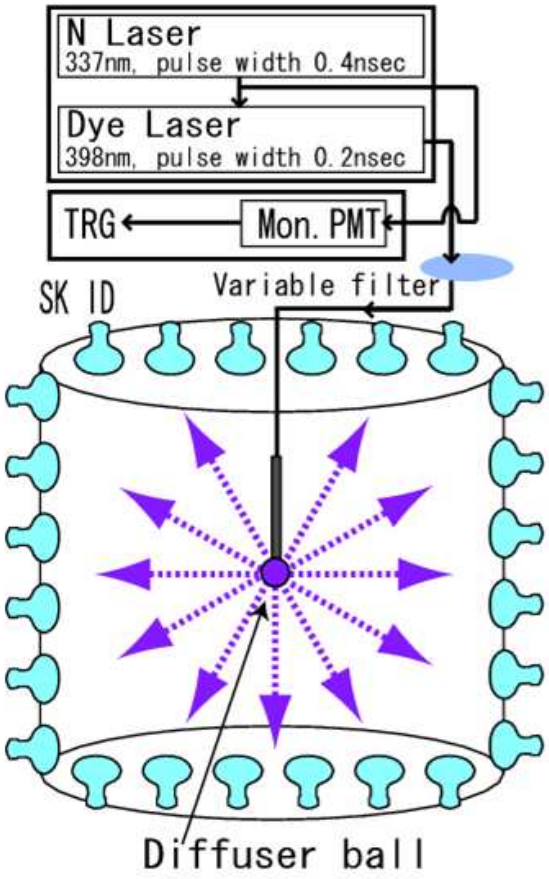

Figure 3.17: A schematic view of the timing calibration system using laser. The diffuser ball is placed at the center of the tank.

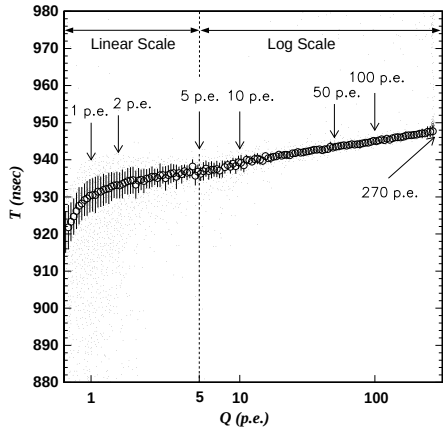

Figure 3.18: A typical TQ-map distribution are plotted as a two dimensional plot of timing vs. charge distribution. Larger value in the vertical axis is corresponding to earlier hits. Data is taken by a laser setup shown in Figure-3.17.

within $\sim$ 3 nsec whose wavelength is 337 nm. Emitted light go into a dye laser module which convert the wavelength of 384 nm, similar to the Cherenkov light. The light intensity can be controlled using the variable attenuation filter from 1 photo-electron level to several hundred of photo-electrons. The light pass through the filter is injected into a diffuser ball, set at the center of the tank, via an optical fiber. In order to provide the uniform light emission, injected light is first diffused by a TiO_2 and then further diffused by the LUDOX, which is a silica gel composed of 20 nm glass fragments in SK-I calibration system.The acrylic diffuser ball containing MgO powder is used in SK-II and SK-III system for the purpose of better uniformity of the light.

3.6 Water transparency measurement

Water transparency in the SK tank affect the number of photons arrive at the PMT so that it can be an important parameter to characterize detector response especially for energy determination. There are two method of water transparency measurement. The scattering and absorption parameter is measured by N_2 laser changing the dye of the laser. Furthermore the transparency is independently measured using decay electron from the stopping muons.

3.6.1 Light scattering measurement by a laser

The light attenuation length in water can be described as follows.

$$L = \frac{1}{(\alpha_{abs} + \alpha_{Rayliegh} + \alpha_{Mie})} \tag{3.7}$$

Where α_{abs}, $\alpha_{Rayliegh}$ and α_{Mie} are the absorption , Rayliegh scattering and Mie scattering coefficients, respectively. Rayliegh scattering occur if the light wavelength is longer than scattering particle. This scattering effect dominate in shorter wavelength region as shown in . Mie scattering is the case that particle is equivalent to the wavelength.

Each coefficient is separately measured by a N_2 laser. Figure-3.19 shows the setup of the water parameter measurement in Super-Kamiokande. The laser light is injected into this detector from top of the tank toward the bottom direction. Each laser whose wavelength is 337, 371, 400 and 420 fires every six seconds during usual data taking period for the measurement.

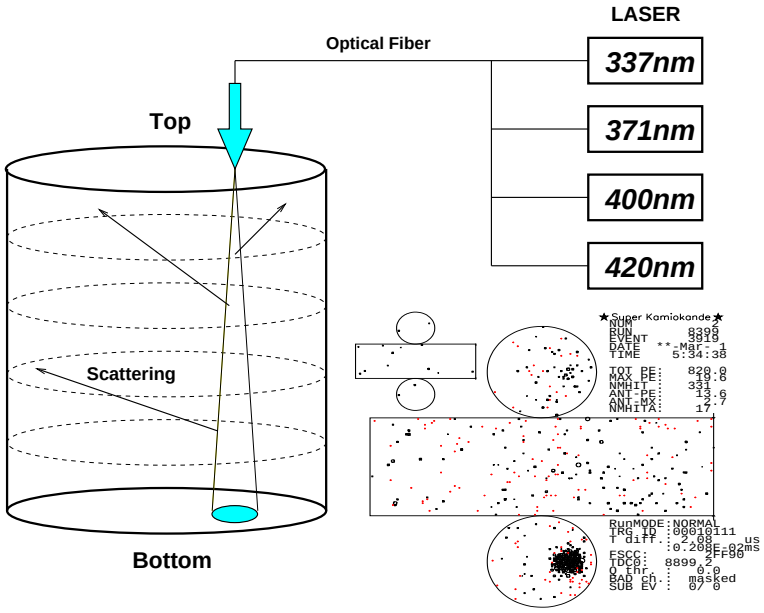

Figure 3.19: A schematic view of the scattering and absorption parameter measurement using the laser.

The barrel part of the detector is separated into 5 groups as shown in Figure-3.19. the PMT hit timing distribution in each region for the calibration data are shown in Figure-3.20. There are PMT his in top and barrel due to the scattering by water molecule or due to the reflection by the bottom PMTs or black sheets. The absorption and scattering coefficients are tuned to make the hit timing distribution of MC simulation agree with the calibration data.

The attenuation coefficients obtained by this method are shown in Figure-3.21. The lines are showing the tuned parameter for each attenuation coefficient determined by fitting to the data.

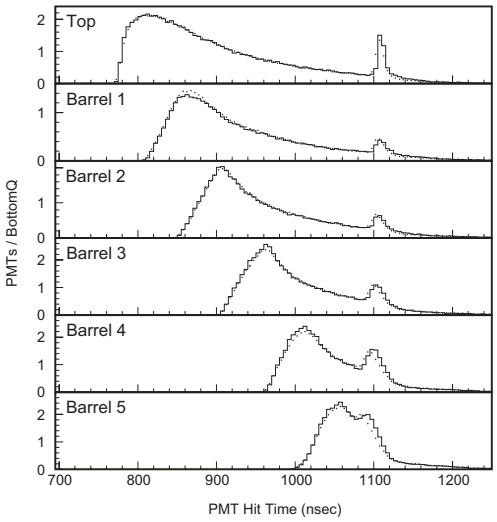

Figure 3.20: PMT hit timing distributions in each groups defined as shown in Figure-3.19. The points shows data and lines shows the MC simulated events. The first peak and second peak are corresponding to the photons scattered in water and reflected on the surface of the bottom PMTs.

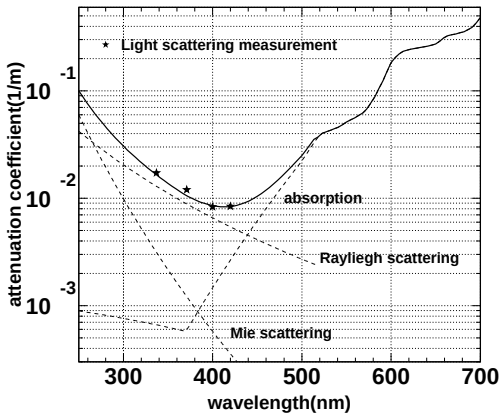

Figure 3.21: Attenuation coefficients as a function of wavelength. Star markers show the result obtained by the water scattering measurements. Lines are representing the expected one tuned by this measurement.

3.6.2 The water transparency by decay electron from stopping muons

The water transparency in SK is monitored continuously by using the decay electrons (positrons) from cosmic ray muon events stopping inside the SK tank. As mentioned in section 7.1, decay electron from muons has a spectrum following a Equation-7.3. Since this physics process is well known, decay electron events can be used for monitoring the water transparency.

At the depth of 1000m underground of SK site, approximately 6000 muons per day stop inside the SK tank and produce a decay electron. In order to select the decay electron events, following selection criteria are applied.

1. The time difference between decay electron candidate and preceding stopping muon is in the range of 2.0 μsec - 8.0 μsec
2. The reconstructed vertex of the candidate event is within 22.5 kton fiducial volume
3. Number of hit PMT greater than 50

By applying these criteria, $\sim$1500 events are selected in one day and it's enough statistics to measure the time variation of water transparency.

To remove the effect of scattered and reflected photons, hit PMTs are selected by following criteria.

1. Hit timing must be within 50 nsec time window after time-of-flight subtraction
2. PMTs must be within a come of opening angle 32 - 52 degrees with respect to the reconstructed direction

A plot of the number of hit PMT is made using the selected PMTs and is fitted with linear function. The inverse of the slope gives the water transparency. Figure-3.22 (top) shows the time variation of water transparency during SK-I period.

The selected decay electron sample are also used for monitoring the energy scale stability. The average number of hit PMT in one week is plotted as a function of time in Figure-3.22. The energy scale variation was within 0.5% during SK-I period.

3.7 Energy scale calibration

For the supernova relic neutrino analysis, energy scale calibration is one of the most important calibration because energy spectrum fitting will be done at the final stage of our analysis. The effective number of hit PMT (N_{eff}) is used to determine the energy of positron in our analysis. We measured conversion factor from N_{eff} to energy within $\sim$ 1% level using two calibration sources. In this section these energy calibration systems are described.

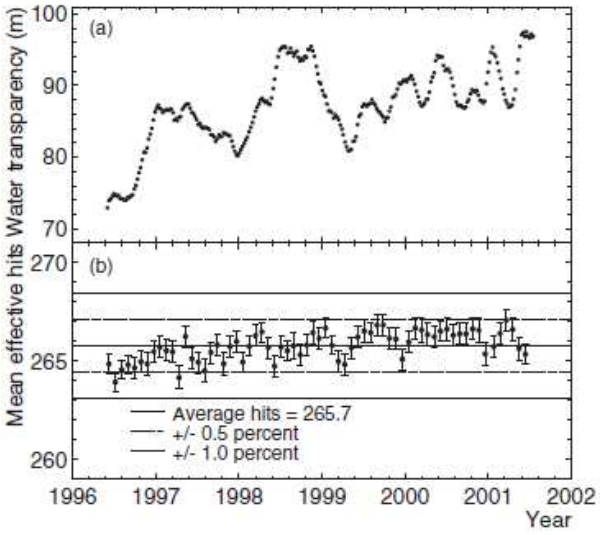

Figure 3.22: Time variation of the measured water transparency (top) and stability of the energy scale as a function of time(bottom). Both of them are measured using decay electron events.

3.7.1 LINAC calibration

To better determine the energy, electron linear accelerator (LINAC) is used to generate energetic electron for the energy scale calibration in Super-Kamiokande[52].

Setup of LINAC system

The LINAC used in SK is a Mitsubishi ML-15MIIII LINAC which was originally made for medical purposes. The specifications of our LINAC system are summarized in Table-3.2.

Accelerator tube	1.69m length and 26mm diameter
Frequency of micro wave	2.856 [GHz]
Electron intensity	MAX 200 μA
Max beam intensity	$\sim 10^6/pulse$ @end of accelerator tube
Beam momentum	5 -18 [MeV/c]
Pulse width	1-2 [μsec]
Pulse rate	10-66 [/sec]
Spread of the beam momentum	$< \pm 0.3\%$

Table 3.2: The specifications of LINAC

The LINAC accelerate electrons using microwave of 2.8656GHz generated by the klystron. The length of one pulse is about 2μsec and its rate is 10 - 66 Hz.

The required electron beam intensity is one electron per one pulse. To achieve this, 10^6 electron in one pulse is required at the exit point of the acceleration tube.

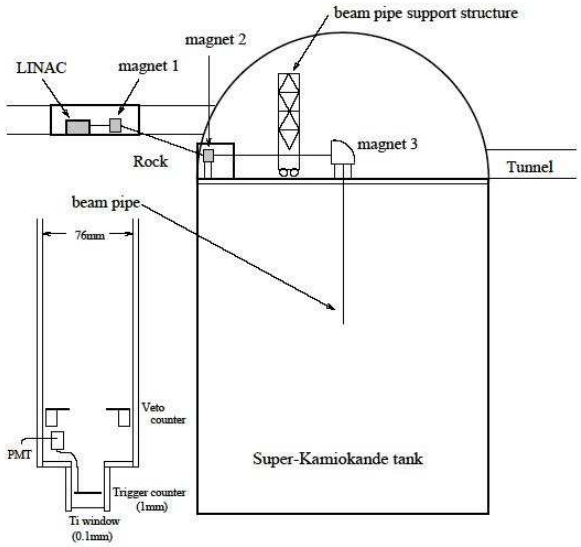

Figure 3.23: Setup of LINAC calibration system at Super-Kamiokande.

The LINAC system produce some background noise such as X-ray and gamma-ray. The mainframe of LINAC is located far from the SK tank in order to prevent those background from affecting data. Electrons, accelerated by LINAC, go into SK tank through the stainless beam pipe whose maximum length is 60m. Inside of the beam pipe is surrounded by μmetal[2] for the purpose of reducing the effect from external magnetic field. Also inside of the beam pipe is vacuated down to 10^{-4} Torr so that electron beam can reach end of pipe without any effect from scattering by air.

The beam pipe is installed to the SK tank from calibration hole on the top of the SK tank. The end of pipe is capped by the titanium cap with 100μm thickness as shown in Figure-3.24. Set of scintillator and PMT is placed at the end of beam pipe for making the LINAC trigger as well as scintillator and PMT for making VETO.

There are 8 dipole and quadratic magnets along the beam line to bend the beam direction and to narrow the beam width. The quadratic magnets control the beam width within $\sim$6mm and 3mrad spread. See Figure-3.25 through 3.27 for a schematic view of magnet setting.

[2] μmetal is a nickel-iron alloy that has very magnetic permeability.

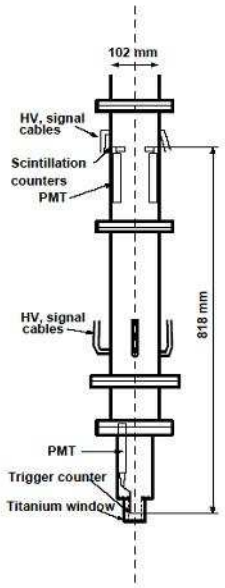

Figure 3.24: The end-cap of the LINAC beam line. A scintillation counter is located above titanium window, used for the trigger.

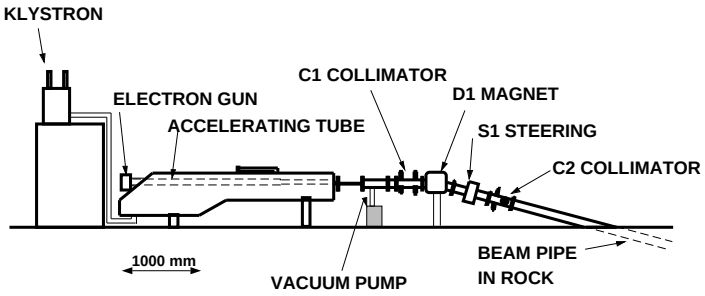

Figure 3.25: The first bending magnet (D1). This magnet determines the beam momentum.

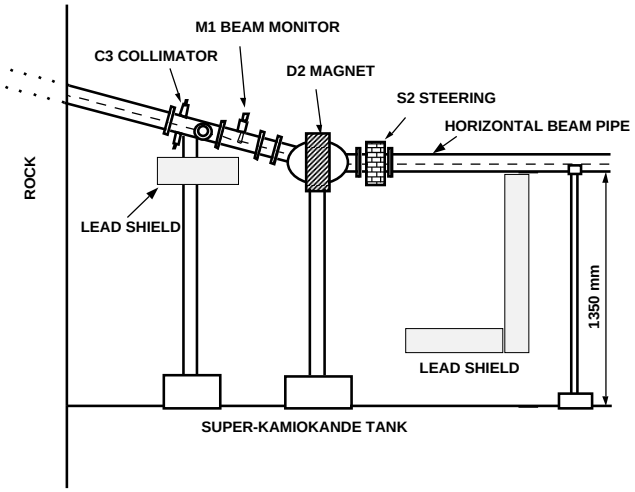

Figure 3.26: The second bending magnet (D2).

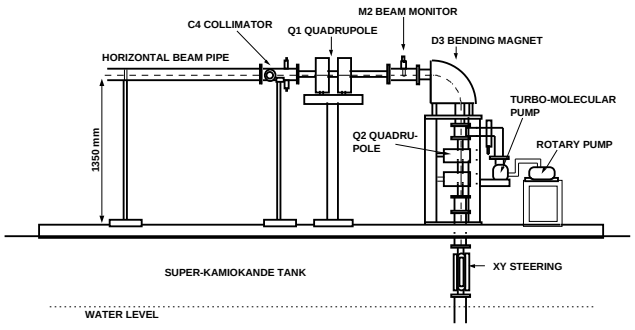

Figure 3.27: The quadratic magnets (Q1, Q2) and 90° bending magnet (D3).

Germanium detector

It is very important to know the electron momentum accurately. The germanium detector, negative type semiconductor detector, is used for the electron momentum measurement. Germanium in the detector is the cylindrical pure crystal with a 57.5mm diameter and a 66.4mm length.

Because the ionization energy of germanium is very small (2.96ev), a lot of carriers are generated so that germanium detector can provide a very good energy resolution. Germanium detector not only has a good resolution but also has a good output linearity for input particle energy. This is also very important because the calibration gamma sources for germanium detector are up to 9MeV.

Figure-3.28 shows the output charge of the germanium detector as a function of gamma-ray energy from calibration source with a fitting result by a linear function. The deviation from fitting result at each point is shown in Figure-3.29. Although deviation is larger in very low energy region, it is still less than 1% in all points.

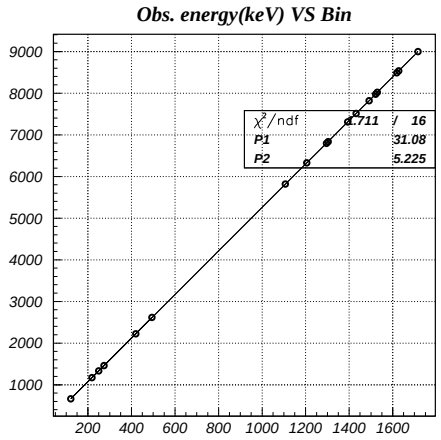

Figure 3.28: The linearity of the Germanium detector. X-axis is the output from the Germanium detector [count] and Y-axis is the energy of the calibration gamma ray source [MeV].

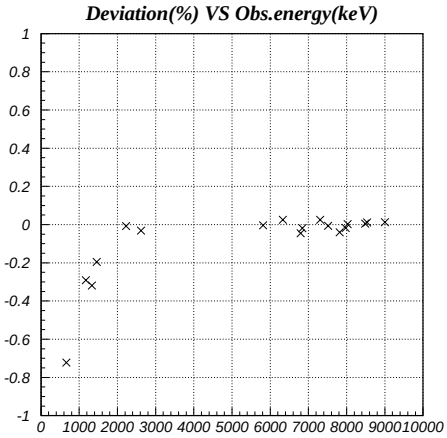

Figure 3.29: Deviation of the output of Germanium detector from the fitted line. X-axis is energy of gamma ray source [MeV]. Y-axis is the deviation of the data point from the fitted line [%].

Result of LINAC calibration

LINAC data are taken at six position changing X (-12m, -4m) and Z (-12m, 0m, +12m); X and Z is the defined axis in SK. For every position data was taken with four momenta (5.1MeV, 8.8MeV, 13.6MeV, 18.9MeV). In SK-I and SK-II, LINAC beam momentum is limited at ∼16MeV due to the power of the

bending magnet. We replaced D3 magnet which bend the beam by 90degrees in order to obtain higher energy beam. By this improvement we succeeded to make the upper limit of LINAC beam up to 18.9MeV in SK-III.

N_{eff} distribution of 8.8MeV and 18.9MeV electron at each six positions are shown in Figure-3.30 and Figure-3.31. Black is LINAC real data and red is simulated N_{eff} using Monte Carlo method (MC). Their consistency seems very good.

The relation between total energy of electron accelerated by LINAC and N_{eff} is shown in Figure-3.32. Total energy is measured by germanium detector with accuracy of +/-20keV. Conversion function from N_{eff} to energy is obtained from this result. The difference between data and MC are shown in bottom two figures. As shown in this figure, position dependence of the energy scale in SK fiducial volume is less than 0.5%. Resolution of N_{eff} is also compared with MC and the result is shown in Figure-3.33. Difference of resolution of 2.5% is obtained.

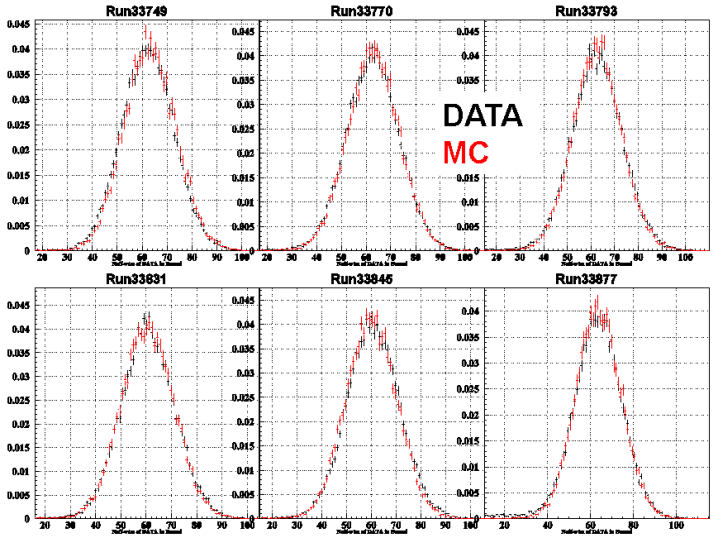

Figure 3.30: N_{eff} distribution of 8.8MeV and 18.9MeV electron at each six positions. Black is data and red is MC.

3.7.2 DT generator calibration

The Deuteron-Tritium Generator (DTG) [53] which is a device to generate neutrons, is used for the cross check of energy scale calibration by LINAC. LINAC beam always move in a downward direction because beam pipe can be installed only from top of the tank. DT generator provide uniform direction source using the decay of ^{16}N so that it can be used to check the directional dependence of the energy scale.

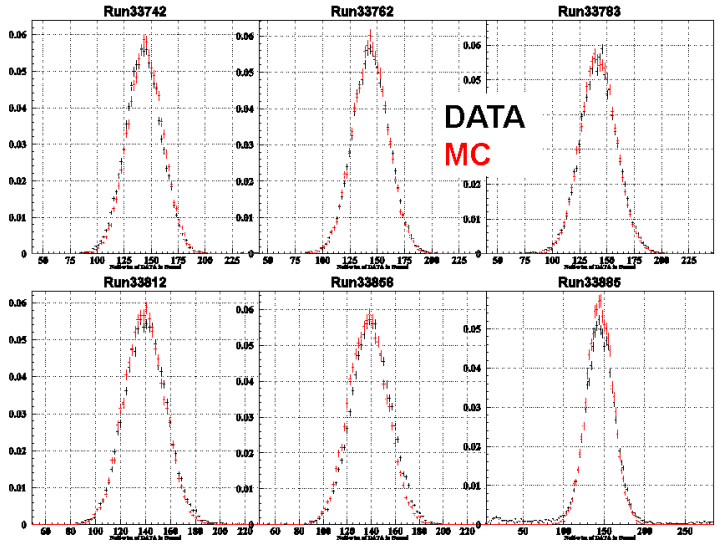

Figure 3.31: N_{eff} distribution of 18.9MeV electron at each six positions. Black is data and red is MC.

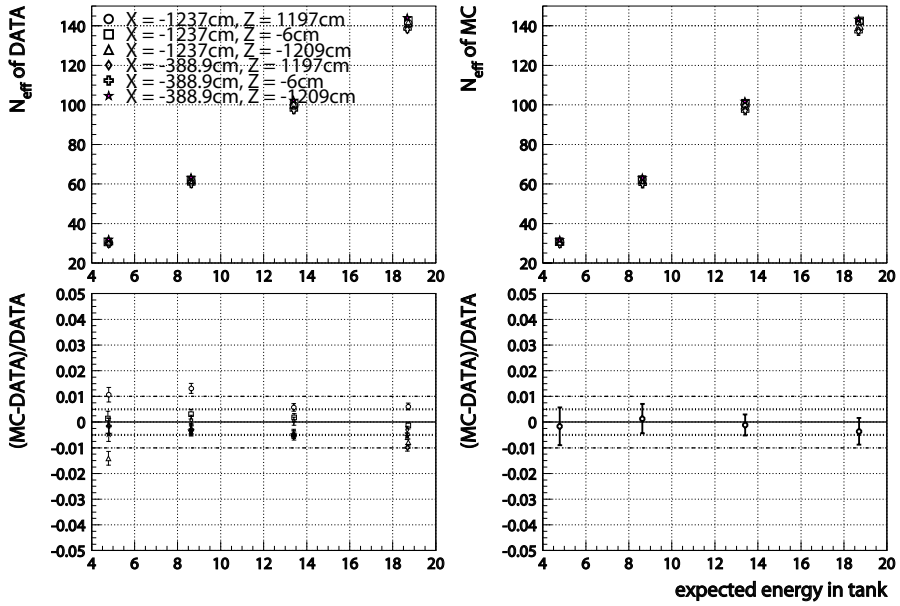

Figure 3.32: The relation between total energy of electron accelerated by LINAC and N_{eff}. Top two figures are N_{eff} .VS. total energy and left top figure shows data and right top figure shows MC. Bottom two figures are MC - data divided by data. Left figure shows each point and right figure shows average of all points.

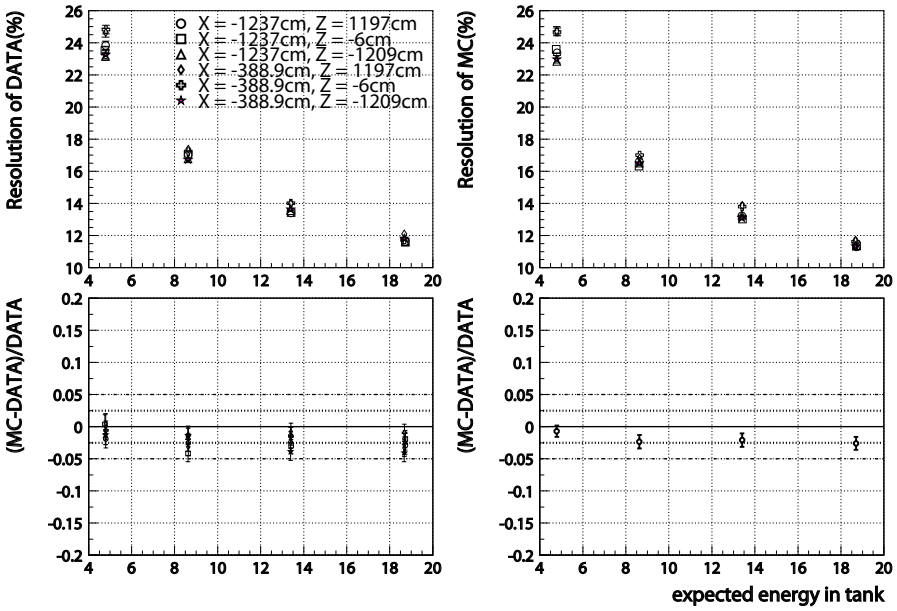

Figure 3.33: Resolution of N_{eff} compared the LINAC data with MC. Top two figures are Resolution .VS. energy and left top figure shows data and right top figure shows MC. Bottom two figures are MC - data divided by data. Left figure shows each point and right figure shows average of all points.

Setup of DTG system

At first DTG starts with a collision of deuterium and tritium inside the generator to create ^4He and neutron. 10^6 neutrons with the 14.2MeV are created at one pulse of collisions. The neutrons interact with ^{16}O and generate ^{16}N and proton, ^{16}o(n,p)^{16}N. ^{16}N decays with the half-life of 7.13 seconds with a Q value of 10.4MeV. The decay products are mainly 6.13 MeV gamma rays and 4.29 MeV beta particles (66.2% fraction) as well as 10.4 MeV beta (28.0%fraction).

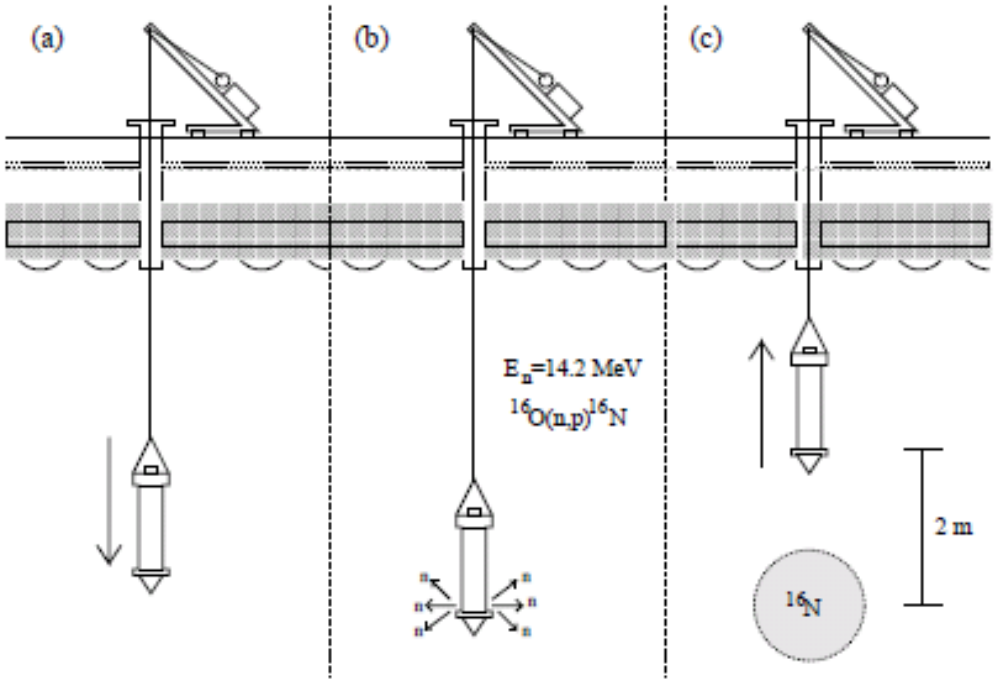

Figure 3.34: A schematic view of the setup of DT generator

Overview of DTG data taking is shown in Figure-3.34. When we take data at SK, the DTG is lowered to the position where data is to be taken. Next the DTG is fired creating neutrons and these neutrons generate ^{16}N surrounding the DTG. Once DTG is fired, it is withdrawn 2 meters to remove the generator from the area of ^{16}N. After the fire of DTG, it takes ∼10 seconds to withdraw apparatus completely, and ∼60% of ^{16}N has decayed.

While the crane is moving, we don't take the data to prevent electrical noise from containing the data. Once the crane stop moving, data are collected for 40 seconds.

Result of DTG calibration

Data from the DTG calibration are reconstructed using the same analysis tools as SRN analysis and then they are compared with MC simulation. Figure-3.35 is the direction dependence of reconstructed energy of DTG event. From this figure, direction dependence of energy scale is almost less than 0.5%.

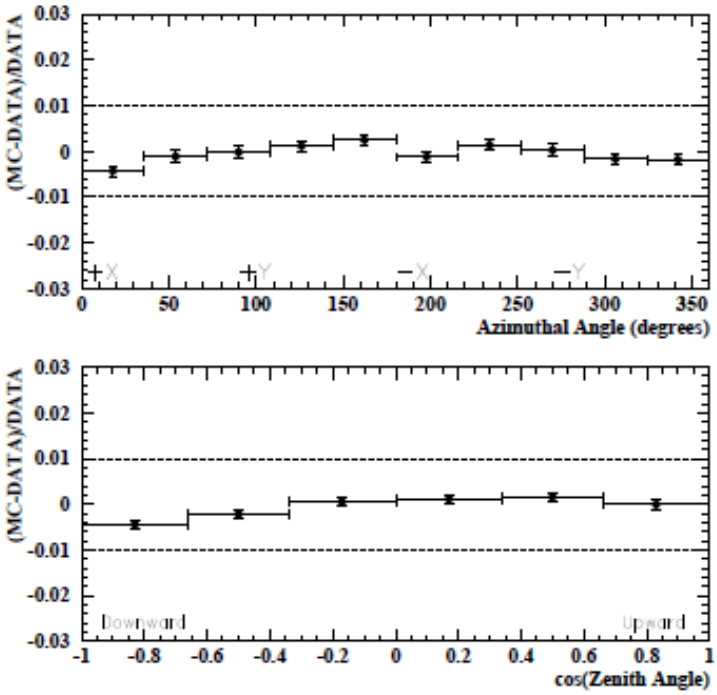

Figure 3.35: The direction dependence of reconstructed energy from DT calibration data from a position-weighted average over all positions in fiducial volume. Horizontal axis is azimuthal angle [degrees] (top figure) and $cos(zenithangle)$ (bottom figure).

Next, position dependence of energy scale is checked using DTG calibration data. Since DTG is relatively smaller than LINAC, data can be taken in many positions and then it's better calibration tool for checking the position dependence of energy scale. Figure-3.36 shows Z (R) dependence of energy scale. Difference between data and MC is very small in small X region (near tank center). Although it's become larger in outer region as shown in Figure-3.36, difference is less than 2% at a maximum in the fiducial volume. Even outside of fiducial volume (X=15m), energy scale difference is 3% level.

At last the DT generator data and the LINAC data are compared as shown in Figure-3.37 and very good consistency can be seen. If we select downward DTG events, energy scale differences LINAC and DTG are less than 0.5% and it's within statistical error. Even if we use all direction of DTG events, energy

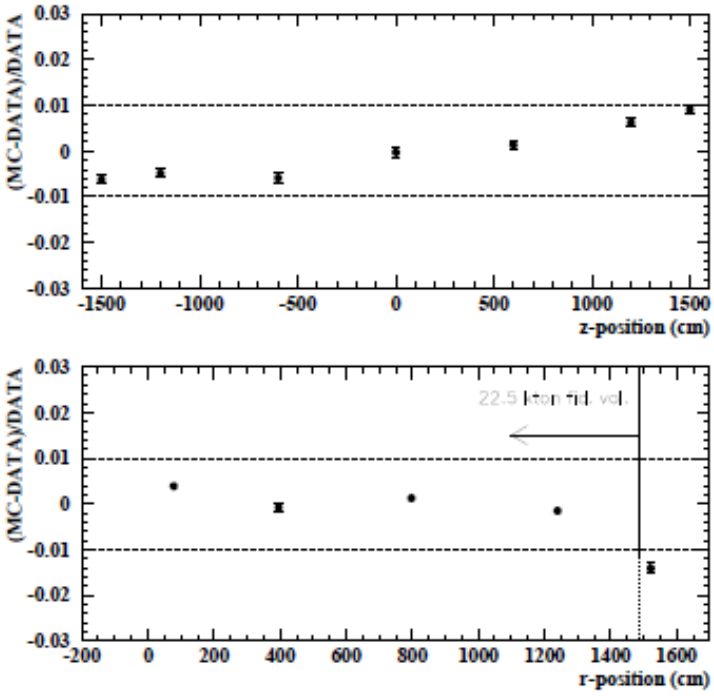

Figure 3.36: Position dependence of the energy scale from DT calibration data from a position-weighted average over all positions in fiducial volume. Horizontal axis of the top figure is Z position of SK tank and that of bottom figure is horizontal distance from tank center.

scale in DTG and LINAC are consistent within 1%. This result demonstrate reliability of the LINAC energy scale calibration.

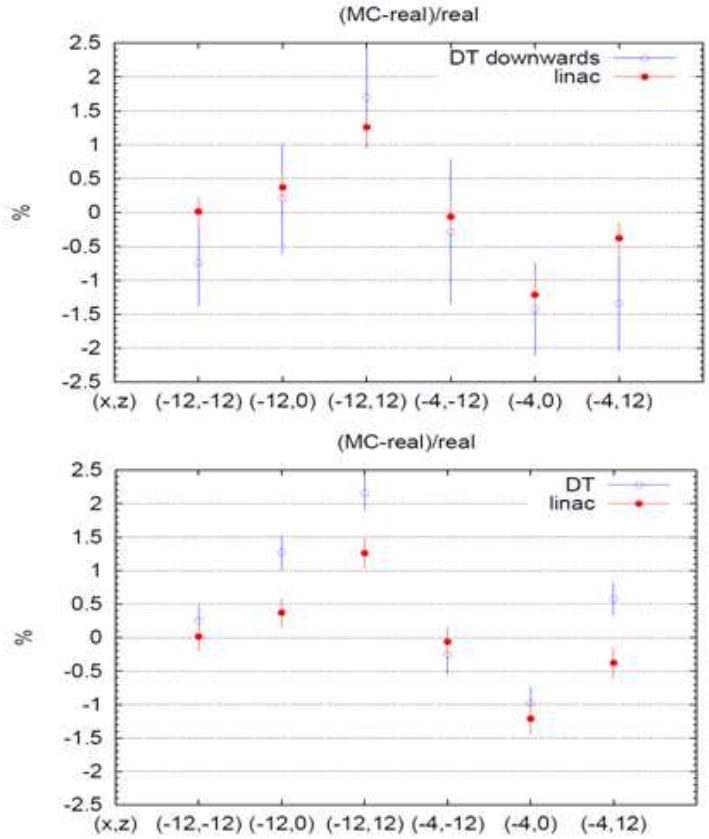

Figure 3.37: Comparison between DTG data and LINAC data. Energy scale in DTG and LINAC are consistent within 1%.

3.7.3 Summary of energy scale calibration

Since the energy scale calibration is quite important for the SRN search analysis, we carefully performed the energy scale calibration. For example, LINAC calibration can determine the conversion factor from the number of hit PMTs to particle energy and also position dependence of energy scale is measured by taking the LINAC data at the several positions. DTG is uniform source in contrast to LINAC so that it can be a good calibration source to measure the directional dependence of energy scale.

The summary of these energy scale calibration is described in this section. Considering the effect of

- Position dependence of energy scale
- Time variation of energy scale
- MC tuning accuracy
- Electron beam determination in LINAC calibration
- Directional dependence of energy scale

we estimate the energy scale uncertainty for SK-I, SK-II and SK-III. They are listed in Table-3.7.3.

Data taking phase	energy scale uncertainty
SK-I	0.64%
SK-II	1.4%
SK-III	0.53%

Table 3.3: Energy scale uncertainty in SK-I, SK-II and SK-III.

Chapter 4

Event reconstruction

The event reconstruction is performed to obtain information such as the vertex, direction and energy from the taken data. In Super-Kamiokande, the vertex of the SRN candidate events are reconstructed using PMT hit timing information. The reconstruction of the event direction is done using the PMT hit pattern. After that, N_{eff}, the effective number of hit PMTs, is calculated and is converted into the corresponding energy using the conversion function obtained from the LINAC calibration. In this chapter, the methods of event reconstruction for SRN candidate events are described.

4.1 Vertex reconstruction

For the reconstruction of the vertex position the hit timing of each ID PMT is used. SRN candidate events are categorized as low energy events whose total charge is less than 2000 photo-electrons (corresponding $\sim$ 250MeV) in SK-I and SK-III, and less than 1000 photo-electrons in SK-II. Our vertex fitter is applied for these low energy events. Figure-4.1 shows an example of typical low energy events. In this section, the method of vertex Reconstruction for SRN candidates is described.

Particles emitting Cherenkov light are moving, but low energy events such as SRN candidates can move only $\sim$ 10 cm in water due to scattering. This is smaller than the vertex resolution of Super-Kamiokande, so we are able to treat the vertex as a point. For the event vertex reconstruction for this SRN analysis we performed a maximum likelihood fit to a timing residual of the Cherenkov signals, as well as a dark noise background, for each vertex hypothesis. The hypothesis which gives a maximum likelihood is chosen as the reconstructed vertex. The likelihood of the vertex fitting is defined as:

$$Likelihood = \sum_{i=1}^{N_{hit}} \log(P(t_i(\vec{x_i}) - tof - t_0)) \tag{4.1}$$

Where $t_i(\vec{x_i})$ is the timing of each hit PMT and tof is the time-of-flight

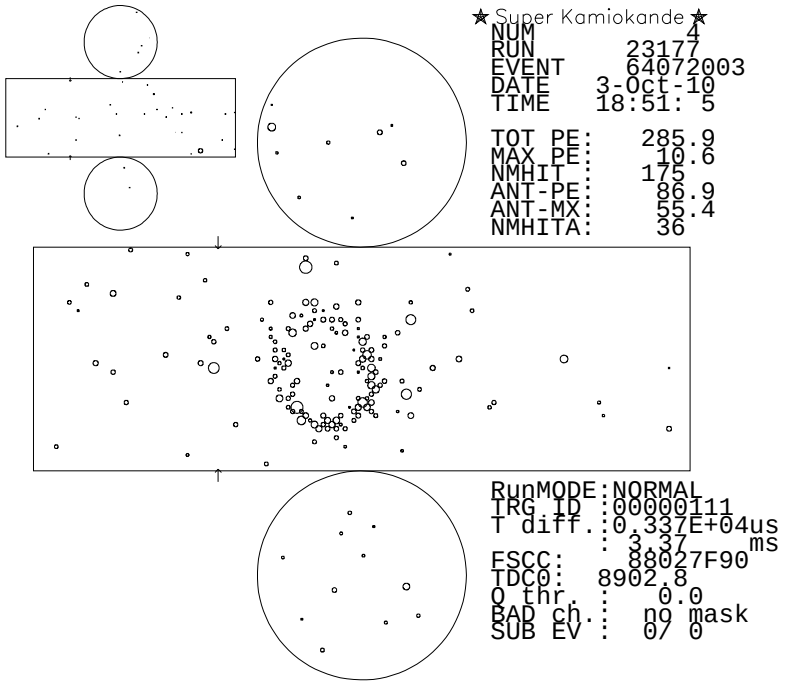

Figure 4.1: An example of a typical low energy event. An example of a typical low energy event as a development view of the SK tank. Each circle shows hit PMTs and its diameter is corresponding to an output charge.

from the vertex position to each hit PMT. t_0 is the timing for which that event occurred, thus $t_i(\vec{x_i}) - tof - t_0$ is ideally zero for all PMTs. P is the probability density function of $t_i(\vec{x_i}) - tof - t_0$ which is obtained from the LINAC calibration data.

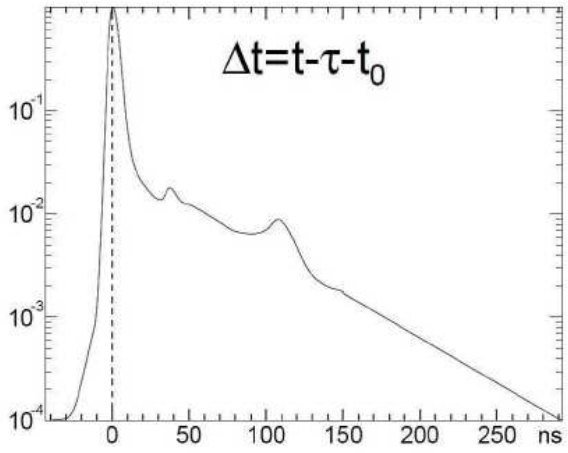

Figure 4.2: Timing distribution of LINAC calibration data after time-of-flight subtraction. The two peaks after the main peak are caused by re-incidence of reflected electrons by the dynodes.

However, sometimes dark noise hits after the time-of-flight subtraction can produce local maxima of the likelihood, at several positions far from the global maximum. Because of the large size of SK, it is tricky and time consuming to search for the global maximum. To reduce mis-reconstruction, as well as improvement of the fitting speed, the likelihood is maximized from a vertex search by the combination of all four PMTs. Each of the four PMT combinations can give a unique vertex so that any event whose number of hit PMTs is four or more can be reconstructed. Then grid vertex search is done for each vertex candidate to avoid selecting a local maximum point. It's iterated, tightening the search range, until it finds a larger and more stable likelihood value, compared to the surrounding grid points. Position resolution using this method for each SK data taking term is obtained from LINAC calibration data and shown in Table-2.2.4.

4.2 Direction reconstruction

Once the vertex position has been determined, the direction of the particle is reconstructed at the next step. Emitted Cherenkov light produces a cone, so the PMT hit pattern should be a ring with an opening angle of 42 degrees. Direction reconstruction uses the likelihood method following the Equation-4.2.

$$likelihood = \sum_{i=1}^{Nhits} \log[f(\phi_i(\mathbf{d}))] \times \frac{\cos\theta_\mathbf{i}}{\mathbf{f_{accept}}(\theta_\mathbf{i})} \tag{4.2}$$

Where $\phi_i(\mathbf{d})$ is the angle between $\mathbf{d}$ and the vector from vertex to the PMT position. $f(\phi)$ is the probability of photon emission as a function of ϕ direction and estimated using MC simulation. $\mathbf{d}$=(d_x, d_y, d_z) is the set of test directions. When we determine the direction, this test direction is changed and the value which maximizes the likelihood of Equation-4.2 is chosen. Figure-4.3 shows this function. The Photon emission distribution shows a peak at 42 degrees and a tail due to scattering. θ_i is the acceptance of a PMT photo cathode and $f_{accept}(\theta_i)$ is its acceptance function. The right side of Figure-4.3 is the distribution of this function.

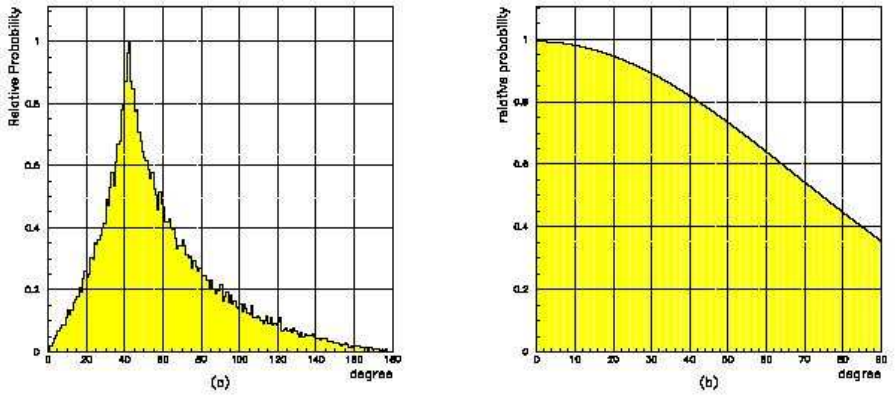

Figure 4.3: The probability density function of photon emission for Cherenkov light from an electron (left figure). PMT acceptance function (right figure).

The accuracy of direction determination is limited by multiple scattering. From LINAC calibration data, the angular resolution of this method is $\sim$ 26 degrees in SK-I.

4.3 Energy reconstruction

The energy of a charged particle is proportional to number of emitted photons. The number of photons can be estimated from number of hit PMTs, (N_{hit}), for low energy events. The reasons why we don't use the number of photo-electrons, but instead N_{hit}, are listed following.

- PMT charge resolution is not good enough at the 1 photo-electron level($\sim$ 50%)
- Most of the hits in low energy events are 1 photo-electron.

- Number of photo-electrons is easily effected by electric noise.

At first, PMTs to be used are selected to maximize the number of hit PMTs within a 50 nsec time window (N_{50}), in order to reduce the effect of dark noise hit. Next various corrections are applied to this N_{50}, obtaining a N_{eff}, which is not dependent on the position in the SK tank as follows:

$$N_{eff} \equiv \sum_{i=1}^{N_{50}} \left[(X_i - \epsilon_{dark} + \epsilon_{tail}) \times \frac{N_{all}}{N_{alive}} \times S(\theta_i, \phi_i) \times exp(\frac{r_i}{\lambda}) / QE(i) \right] \quad (4.3)$$

The meaning of each term is:

- X_i : Correction about multi photo-electron hit

  If the event occurs near the tank wall, though it's still inside of fiducial volume, it can cause a hit whose number of photo-electrons is more than one. We correct for this effect using the following correction:

$$X_i = \begin{cases} \frac{log[(1-x_i)^{-1}]}{x_i} & (x_i \neq 0) \\ 2.5 & (x_i = 0) \end{cases} \quad (4.4)$$

$$x_i = n_i / N_i \quad (4.5)$$

  Where N_i is a number of PMTs surrounding hit PMT and n_i is a number of hit PMT in N_i. The multi photo-electron hit effect is corrected using a ratio of these two numbers, $x_i = n_i/N_i$.

- ϵ_{dark} : Correction for PMT dark hit

  The dark noise hit rate is about 3kHz for each PMT, and there were about 10,000 PMTs mounted in the SK detector during SK-I and SK-III, so ~ 1 hit or less is expected within 50 nsec. This should be subtracted because these hits are not originating from Cherenkov light. The following ϵ_{dark} is used for the correction of this effect.

$$\epsilon_{dark} \equiv \frac{N_{alive} \times R_{noise} \times 50nsec}{N_{50}} \quad (4.6)$$

  In this equation, N_{alive} is number of normal PMTs and R_{noise} is the dark noise rate [hits/nsec] in each run.

- ϵ_{tail} : Effect of the reflection

  Cherenkov light reflected by a PMT or the black sheet has a possibility of falling on a PMT photo cathode and emitting a photo-electron. But these reflected photons are delayed and do not usually come within the 50 nano sec timing window. To recover such delayed hits for the energy calculation, tail hits within 100 nano sec are used as the following correction factor.

$$\epsilon_{tail} \equiv \frac{N_{100} - N_{50}}{N_{50}} - \epsilon_{dark} \tag{4.7}$$

Here N_{100} is the number of hits within the 100 μsec timing window. If ϵ_{tail} is negative, the effect of reflection is not considered.

- N_{all}/N_{alive} : Dead PMT correction

  There are more than 10,000 PMTs in SK, however, $\sim$ 100 PMTs were dead during the SK-I period. Although the fraction of dead PMTs was less than 1%, this fraction varied with time. In order to compensate for the effect of dead PMTs, the ratio of all PMTs and living PMTs is multiplied.

- $exp(\frac{r_i}{\lambda})$: Correction of water transparency

  The attenuation length of pure water in SK is about 100m, meaning the emitted Cherenkov photons are attenuated by $exp(\frac{r_i}{\lambda})$ before reaching the PMT from the vertex position. Here r_i is the distance between a hit PMT and the vertex position of a SRN candidate, λ is the attenuation length of SK pure water. Attenuation length changes during data taking terms and it's measured using decay electrons from stopping muons as described in the previous chapter.

- $S(\theta, \phi)$: Correction of PMT-photon acceptance

  Figure-4.4 shows the PMT-photon acceptance as a function of photon-incident angle. The correction function, $S(\theta, \phi)$, distributes like Figure-4.5. The reason for the ϕ asymmetry is an effect of shadowing of surrounding PMTs.

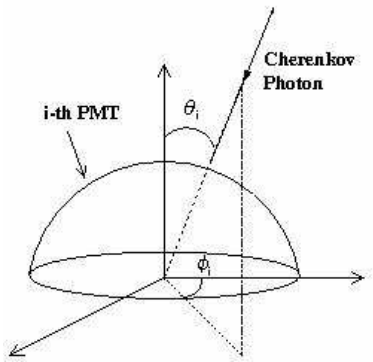

Figure 4.4: Definition of photon incident angle to PMT

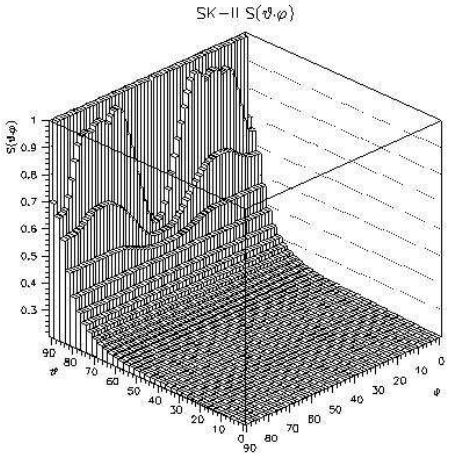

Figure 4.5: Correction function of photon incident angle obtained from MC simulation : $S(\theta, \phi)$

- QE(i) : Correction of quantum efficiency

  As described in Chapter 3, each PMT has a different QE value which is corrected using each measured QE individually.

Reconstructed energy is determined from N_{eff}, with all the corrections above. This conversion factor is obtained from LINAC calibration as described in section 3.7. Energy resolution for 10 MeV electrons in SK-I and SK-III was 14% using this method. In SK-II, it was 20% due to the smaller number of PMTs.

Chapter 5

Data reduction

The data taking term for the first SK phase was from April 1996 to November 2001. Additionally data was collected from October 2002 to October 2005 in a second phase and from July 2006 to September 2008 in the third phase. The livetimes for each period were 1496days, 791days and 548days respectively. These data sets included many kinds of events, for example, cosmic-ray muons, solar neutrinos, gamma-rays from the tank structure and so on. Such events can be background for our SRN analysis. We applied several reductions in order to remove these background events and select our SRN candidate events. In this chapter, we focus on the reductions we applied to the SK data to select the SRN candidate events.

5.1 1st reduction

The 1st reduction which is applied removes cosmic ray muons and bad quality events which should not be SRN candidate events. The cuts applied in the 1st reduction are explained in this section.

Total charge cut

Most of the events originating from cosmic ray muons or atmospheric neutrinos deposit energy usually higher than 1GeV, while the positrons from SRN interactions deposit only up to several tens MeV. To remove very high energy events such as cosmic ray muons, a total charge and total number of hits cuts are applied. The cut criteria is 2,000 photo-electrons and 800 hits in SK-I and SK-III, corresponding to $\sim$ 200MeV. The criteria in SK-II is half of that in SK-I and III due to the half PMT coverage. The total charge distribution in typical runs in SK-III is shown in Figure-3.1.

Time difference cut

The events, whose timing difference from preceding LE/HE trigger event is less than 50 μsec, are removed from data in order to remove decay electron

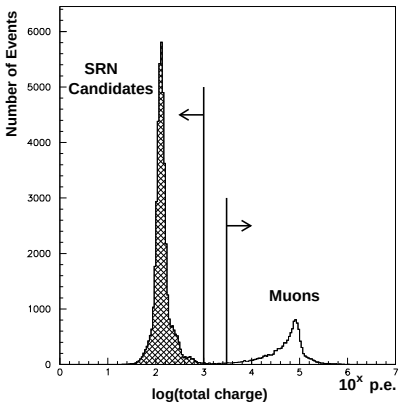

Figure 5.1: Total charge distribution in SK-I. The second peak is mainly caused by muons.

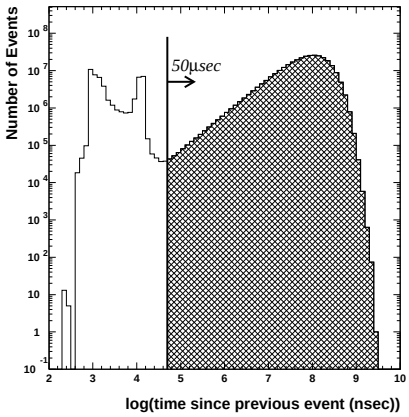

Figure 5.2: Time difference from previous LE/HE event (dt). The events whose dt is shorter than 50μsec are rejected to remove Decay electron and electronics noise events.

of stopping muon. This cut also can remove an electric noise event, so called 'ringing', that occur after an event deposited large amount of light. Figure-5.2 shows a distribution of time difference from preceding eve nt.

Fiducial volume cut

The gamma-rays from the material of the ID wall and the surrounding rock can be a background of SRNs. Since these background events occur near the wall, we can remove these events using a cut for distance from the ID wall. The events whose reconstructed vertex are less than 200cm from the ID wall are removed. By this cut, the fiducial volume of the SRN analysis is 22.5 ktons.

Pedestal event cut

ATM pedestal data is taken every 30 minutes in our DAQ system. During pedestal data taking, the ATM channels cannot record signals from their connecting PMTs. Pedestal data is taken for 1/8th of the SK ID area, all at once, so this data is lacking parts. Therefore, the events taken during the pedestal data taking period are rejected.

Calibration event cut

In order to check the detector stability(PMT Gain, Timing and Water transparency etc.), calibration sources are set in the SK tank and are fired automatically. These events cannot be used for SRN analysis, so they are removed from

data by being tagged with a calibration trigger flag.

Outer Detector event cut

Cosmic rays originate outside of the detector and must deposit energy in the OD, so they can be tagged by an OD trigger. As described in section 2.4.2, the OD trigger is activated when the number of OD PMT hits exceeds 19 within a 200 nsec time window. OD triggered events are removed from our data sample to remove cosmic ray muon backgrounds.

First electric noise event cut

PMT hits from electric noise generally tend to be small charge hits, so events induced by electric noise are cut using a fraction of small charge hit PMTs. If the fraction of PMTs having less than 0.5 photo-electrons(called "noise ratio") is more than 0.4, such events are removed. The noise ratio distribution in typical runs is shown in Figure-5.3.

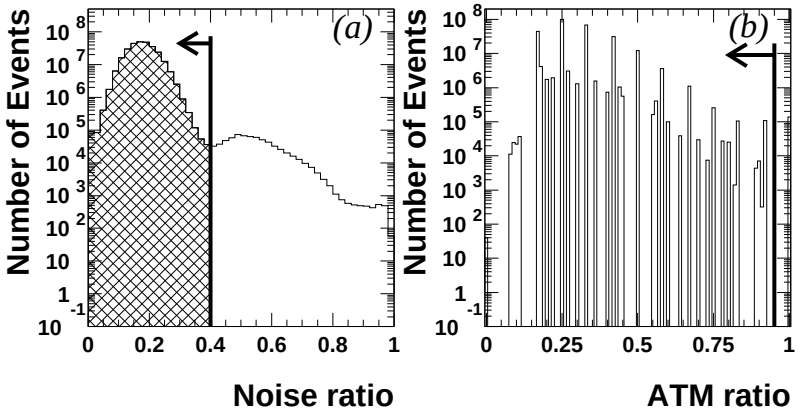

Figure 5.3: Noise ratio distribution (left) and ATM ratio distribution (right).

Second electric noise event cut

If some of the ATM board have some electric noise, most of the channels of this board should have hits. In the case that the fraction of hit channels in one board(ATM ratio) is more than 95%, such events are removed.

5.2 Spallation event cut

Approximately two cosmic ray muons are coming into the SK tank every one second, even under 1000m of rock. These muons can cause spallation in the oxy-

gen nucleus of the water molecule and other radioactive nuclei will be generated as follows.

$$\mu + {}^{16}O \rightarrow \mu + X \tag{5.1}$$

We call these nuclei spallation products and these are one of the most serious backgrounds in this analysis. Possible spallation products and their characteristics are listed in Table-5.1. Some of the spallation products, for example ${}^{11}Li$,${}^{12}N$, can be a background around 20 MeV due to the detector energy resolution.

Isotope	$\tau_{\frac{1}{2}}$(sec)	decay mode	Kinetic Energy (MeV)
${}^{8}_{2}He$	0.119	β^-	9.67 + 0.98(γ)
		β^- n	16%
${}^{8}_{3}Li$	0.838	β^-	$\sim$ 13
${}^{8}_{3}B$	0.77	β^+	13.9
${}^{9}_{3}Li$	0.178	β^-	13.6 (50.5 %)
		β^- n	($\sim$ 50 %)
${}^{9}_{6}C$	0.127	β^+ n	3$\sim$15
${}^{11}_{3}Li$	0.0085	β^-	16$\sim$20 ($\sim$ 50 %)
		β^- n	$\sim$ 16 ($\sim$ 50 %)
${}^{11}_{4}Be$	13.8	β^-	11.51 (54.7 %)
			9.41 + 2.1 (γ) (31.4 %)
${}^{11}_{4}Be$	0.0236	β^-	11.71
${}^{12}_{5}B$	0.0202	β^-	13.37
${}^{12}_{7}N$	0.0110	β^+	16.32
${}^{13}_{5}B$	0.0174	β^-	13.44
${}^{13}_{8}O$	0.0086	β^+	13.2 16.7
${}^{14}_{5}B$	0.0138	β^-	14.55+6.09 (γ)
${}^{15}_{6}C$	2.449	β^-	9.77 (36.8 %)
			4.47+5.30 (γ)
${}^{16}_{6}C$	0.747	β^- n	$\sim$ 4
${}^{16}_{7}N$	7.13	β^-	10.42 (28.0%)
			4.29+6.13 (γ) (66.2%)

Table 5.1: A list of spallation products and their decay modes.

We developed a new spallation cut with a likelihood based on four variables in order to increase the efficiency and lower the energy threshold.

5.2.1 Spallation cut in SK-I and SK-III

A spallation cut for SRN analysis uses a likelihood method based on four variables. The four variables include the time difference between the preceding muons and SRN candidate event (dt), and the transverse distance from muon

track to reconstructed relic candidate position (dl_{trans}). For the cut we also use two other variables by making a histogram like Figure-5.4 for every muon.

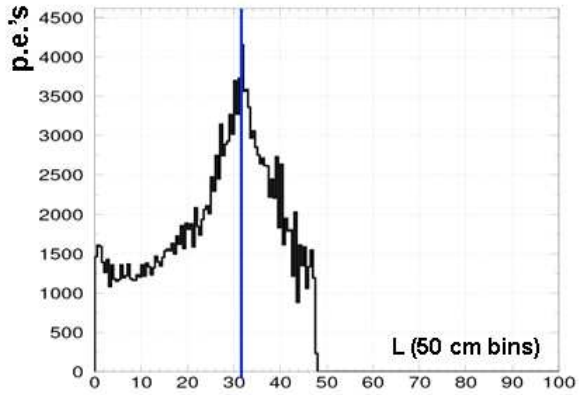

Figure 5.4: Charge distribution along a muon track. Each bin corresponding to 50 cm of muon track length. Number of photo-electrons on the vertical axis is corrected by considering the effect from water transparency and PMT coverage.

The horizontal axis of Figure-5.4 corresponds to the length of the muon track(0 is muon entering point into the inner detector). The vertical axis is the charge produced from each segment along the muon track(extracted from the observed charge in every PMT and their geometrical relations to the muon track). The effect of PMT coverage and water transparency are also considered when making this charge distribution. If we find a strong peak, this indicates where spallation occurs along the muon track. The third variable for our likelihood method is the longitudinal distance from the reconstructed position of the relic candidate to the position where we expect the spallation event along the muon track(dl_{long}). The fourth variable is the total charge which is emitted within +/-5 m of the peak position on the muon track(Q_{peak}). Figure-5.5 shows the relation between the muon track and these parameters as a conceptual view.

Each parameter is calculated for every muon beginning 100 seconds before the SRN candidate. In addition muons are categorized into four muon types as follows.

- Single through going muon ($\sim$ 84%)

  Most muons originating from cosmic rays, and coming from outside the detector, are categorized as a single through going muon. It has only one track and goes through the entire ID.

- Multiple muon ($\sim$ 6%)

  Multiple muon events have two or more muon tracks. The SK event timing window is 1.3 μsec and the muon rate is 2 Hz, so the probability of chance coincidence is very small. However, sometimes multiple muons

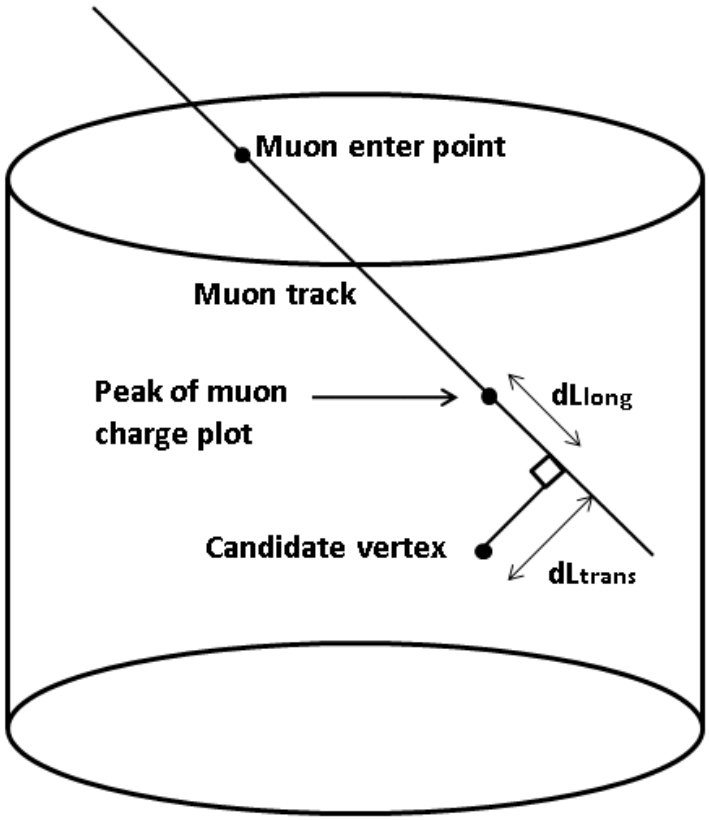

Figure 5.5: An explanation of the variables used in the new spallation cut. The cylinder in this figure represent SK inner detector.

originating from the same cosmic ray come to the detector within the same event timing window.

- Stopping muon ($\sim$ 7%)

  Stopping muons stop in the detector and decay into electrons and neutrinos. There is no exit point, but the vertex of its decay electron can tell us the muon stopping position.

- Corner clipping muon ($\sim$ 3%)

  These events just clip the ID tank corner. Their muon track lengths are less than five meters.

The distributions of the four variables for a single through going muon are shown in Figure-5.6 and Figure-5.7.

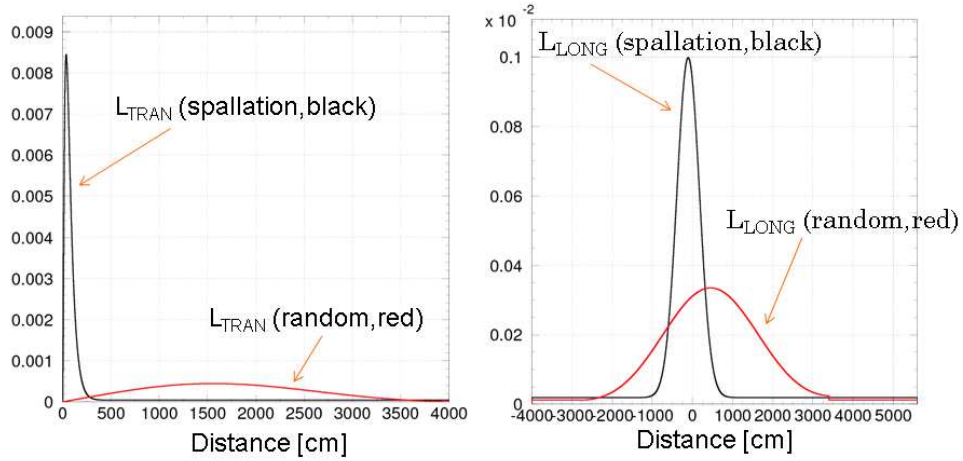

Figure 5.6: dL_{trans}(right) and dL_{long}(left) distribution with single through going muons. Black histogram is for spallation like sample that is made by real data minus the random sample. Red histogram is for the random sample. Clear separation can be seen.

The likelihood distribution is made for each type of muon and a cut point is tuned individually. In the case of multiple muon events, muon reconstruction is more difficult and the cut criteria is more strict to remove all the spallation background. For an example, the spallation likelihood distribution for a single through going muon in SK-I is shown in Figure-5.8.

The inefficiency of the spallation cut was estimated using random sample and, it was 18.5% in the 18 - 24 MeV and 23% in 16-18 MeV.

5.2.2 Spallation cut in SK-II

Energy resolution in SK-II is worse than that of SK-I and SK-III so that more spallation events are expected to contaminate SRN search energy region. We

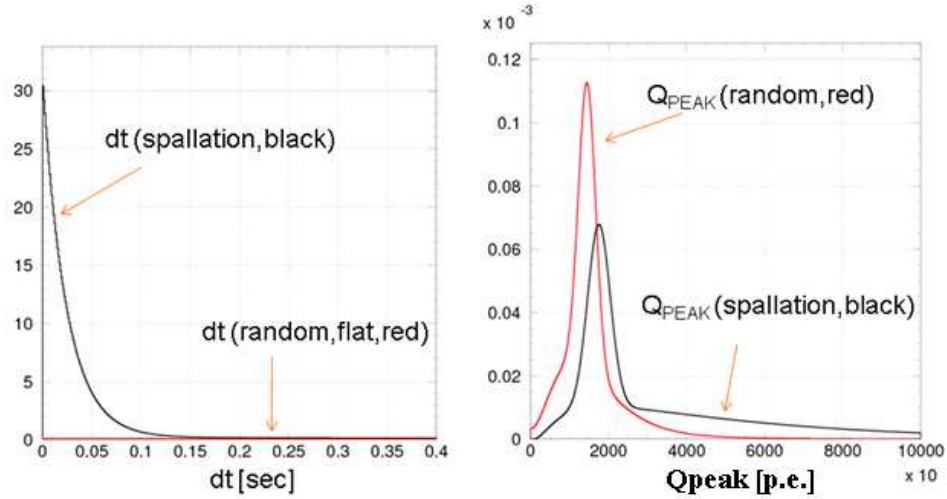

Figure 5.7: dt(right) and Q_{peak}(left) distribution with single through going muons. Black and red histograms are the same sample as Figure-5.6.

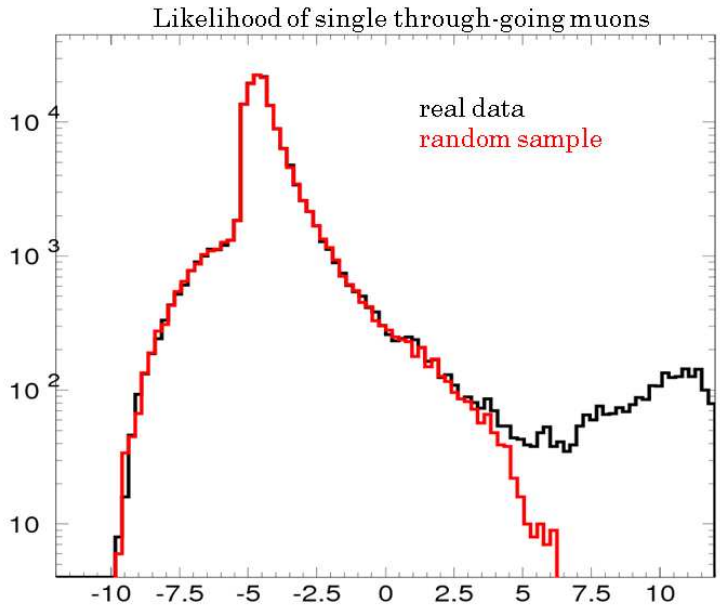

Figure 5.8: Spallation likelihood distribution for SK-I data(black) and the random sample(red) using single through going muons.

adopted the spallation cut developed for solar neutrino analysis in SK-II [39] because it is a tighter than spallation cut described in previous section although its inefficiency is larger. In SK-II analysis, the spallation cut is applied in two steps. First is a cut based on a three variable likelihood method which was developed and optimized for SK's solar ν analysis. Three variables are; time difference from the candidate event to preceding muon (dt), the transverse distance from the reconstructed position of candidate event to preceding muon track (dl_{trans}) and residual charge which is observed total charge minus expected charge from muon track length (Q_{res})[1]. Thus likelihood is calculated as follows.

$$likelihood = \pounds(\Delta T) \times \pounds(\Delta L) \times \pounds(Q_{res}) \tag{5.2}$$

The likelihood distribution for real data and random sample are shown in Figure-5.9. We tuned the cut criteria to save 80% of random sample.

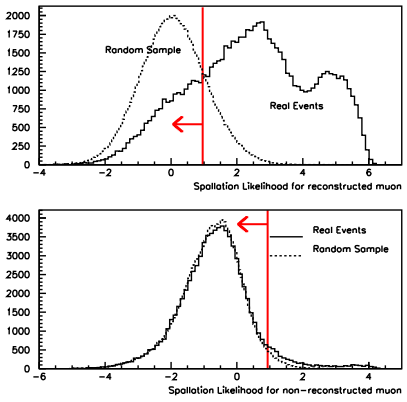

Figure 5.9: Likelihood distribution for real data (Solid line) and random sample (dotted line). Top figure is for the reconstructed muon event and bottom figure is for the failed reconstructed muon events. In failed case, it is impossible to obtain dl_{trans} so that only dt can be used for likelihood calculation.

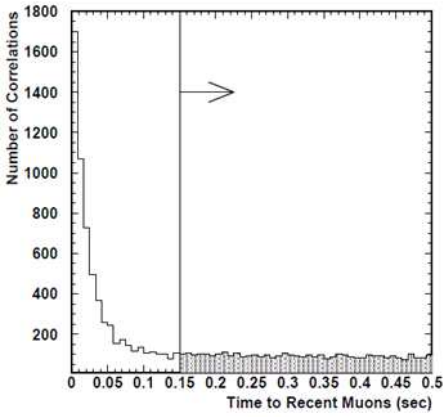

Figure 5.10: Time difference from SRN candidate event to preceding muons (dt). Even after likelihood cut, the is an excess in short dt region. We removed all the events whose dt is shorter than 0.15 sec.

Since this cut is not tight enough, we need to apply additional cut. A second cut was applied using a time difference from last muon (dt_{last}). We know higher energy spallation product has basically shorter half-life (see Table-5.1). Figure-5.10 show dt_{last} distribution in SK-I and this cut rejects events whose time difference from the last muon is shorter than 0.15 sec.

[1]Expected charge from muon is 1000 photo-electron / meter

By applying these two cuts, all the spallation events can be removed above 20 MeV but several spallation like events exist in SK-II data even after this tighter spallation cut. The combined inefficiency of these cuts is 36% below 34MeV.

5.3 Double timing peak cut

Event timing window in SK is 1.3 μsec. Since the muon livetime is 2.2 μsec, some of the decay electrons and their parent muons can be in the same event. This can happen if a low energy muon, but still higher than Cherenkov threshold, stops in the detector and decays quickly, within same event timing window. In such cases, the ID hit PMT timing distribution has two peaks, as shown in Figure-5.11.

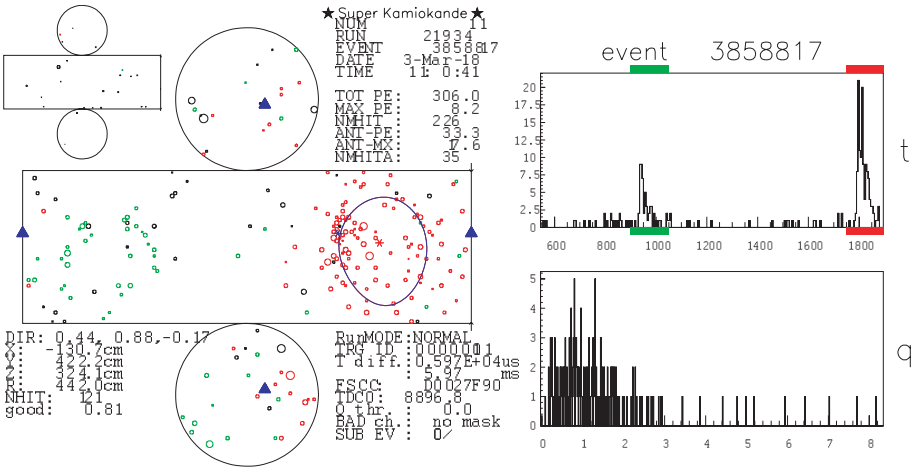

Figure 5.11: An example of timing, two peak events. Left figure is a development view of the SK tank and the right top figure is the PMT hit timing distribution. The first peak of the timing distribution is low energy muons and the second peak is the decay electrons.

We removed the events whose timing histogram has multi peaks. To search for timing peaks, we open a 15 nsec timing window, after time-of-flight subtraction, and count the number of hit ID PMTs within that 15 nsec window. If the number of hits in the first and second peak are both more than 5, such an event is removed from our data sample. The inefficiency of this cut is estimated using a SRN MC simulation sample, and is less than 0.5%.

5.4 Cherenkov angle cut

The opening angle of the Cherenkov light(θ), is determined by the equation of $\cos\theta = \frac{1}{n\beta}$. In the case of water, the refractive index is 1.33, so that Cherenkov

light is emitted with an opening angle θ of 42 degrees, if β=1. Since the electron mass is 0.511 MeV, electrons above the SK trigger threshold($\sim$ 5 MeV) always have β=1, that is to say an opening angle θ which is 42 degrees.

On the other hand, in the case of heavier particles, such as muons, cannot be relativistic enough to approximate $\beta = 1$ and so the Cherenkov opening angle becomes less than 42 degrees. The expected Cherenkov opening angle for muons as a function of energy is shown in Figure-5.12.

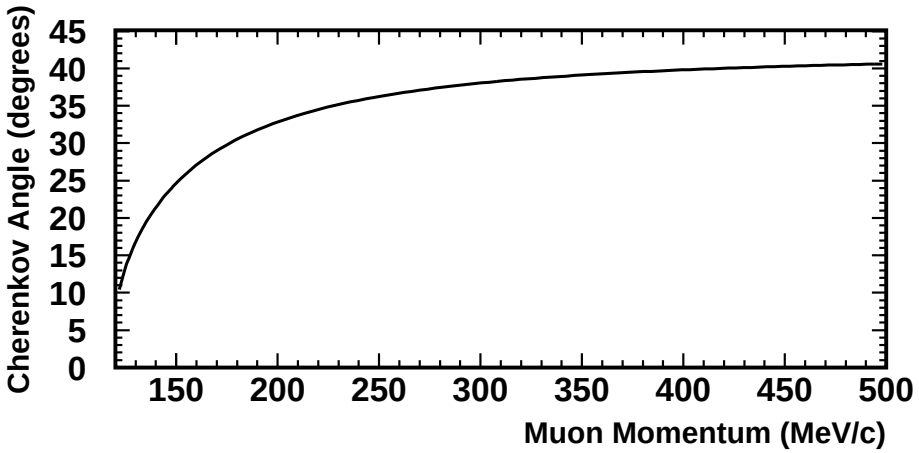

Figure 5.12: Cherenkov opening angle of muons is plotted as a function of the muon momentum. Muons contaminating the SRN search have muon momentum $<$ 300 MeV which correspond to Cherenkov angle $<$ 38 degrees.

Figures-5.13 and 5.14 show an example of an electron-like event and a muon-like event, respectively. The solid line is the expected ring assuming 42 degrees by the reconstructed vertex position and direction. The muon-like ring clearly shows a smaller ring than the expected ring of 42 degrees, as for the electron-like event. We have separated muon-like background using the difference of opening angle θ.

Also neutral interactions of atmospheric neutrinos on oxygen nuclei occasionally occur and the excited nuclei's decays emit several gamma rays. These gamma rays have uniform direction and so this event generates an isotropic hit pattern. This event clearly gives a larger opening angle than 42 degrees, so we can separate this from electron-like events. The example of such a gamma ray event is shown in Figure-5.15. There is no clear Cherenkov ring pattern unlike for the electron-like and muon-like events.

Calculation method of the Cherenkov angle follows the steps below.

1. Search the hit timing peak, which includes the maximum hit PMTs(N_{15}) within a 15 nsec timing window after TOF subtraction.

2. Choose any combination of three hit PMTs in N_{15} and get the unit vector from the vertex position of the SRN candidate event to each PMT(see

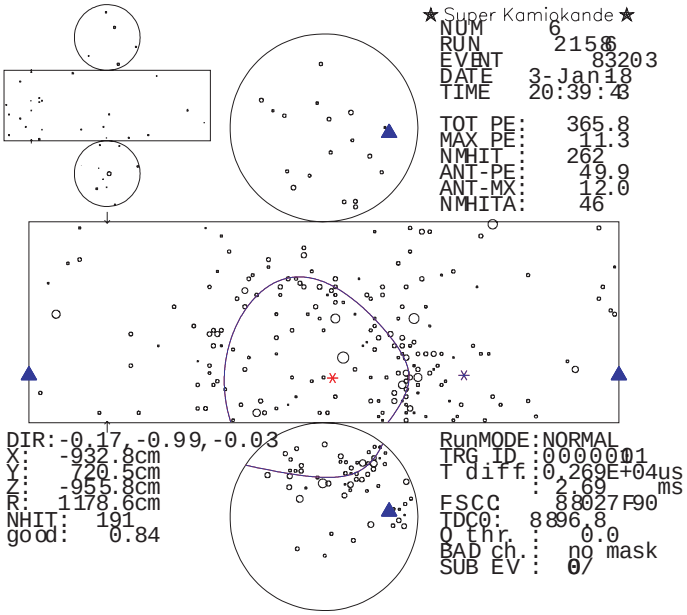

Figure 5.13: The event display of typical electron like event. Lines represent the expected Cherenkov opening angle, assuming 42 degrees.

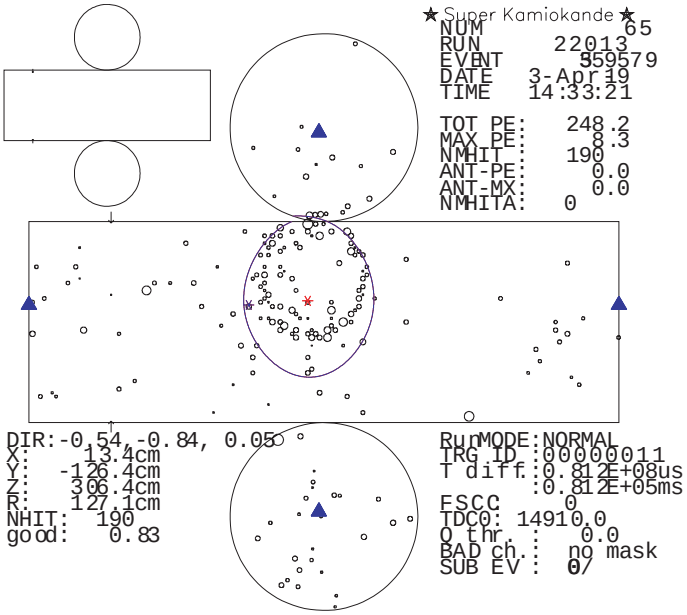

Figure 5.14: The event display of typical low energy muon like event. The Cherenkov ring is smaller than 42 degrees.

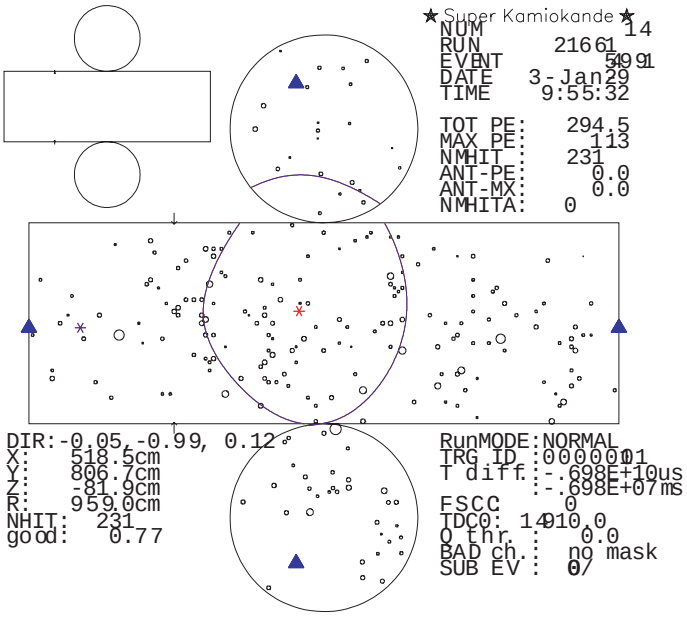

Figure 5.15: The event display of typical gamma like event. Hit PMTs are uniformly distributed and no clear Cherenkov ring can be seen.

Figure-5.16).

3. The vertex position and unit vectors obtained above can form a unique circular cone. The opening angle of this cone is calculated. Each combination of three hit PMTs gives the opening angle from the vertex position.

4. Repeat step 2 and 3 for all the combination of three hit PMTs(repeat ${}_{N_{15}}C_3$ times). The results of this opening angle calculation for electron-like, muon-like and gamma-like events are shown in Figure-5.17.

5. Find the peak of the opening angle distribution from this histogram with 6 degree windows.

6. Remove the events whose obtained Cherenkov angle is smaller than 38°(μ-like) or larger than 50°(γ-like).

Figure-5.18 shows the Cherenkov angle distribution of real data for SK-I. The three peaks caused by muon, electron and gamma-ray events are clearly separated. We cut the events whose Cherenkov angle less than 38 degrees and those whose angle is greater than 50 degrees, in order to select only electron like events. The inefficiency of this cut is $\sim$ 90%, estimated from the SRN MC simulation events.

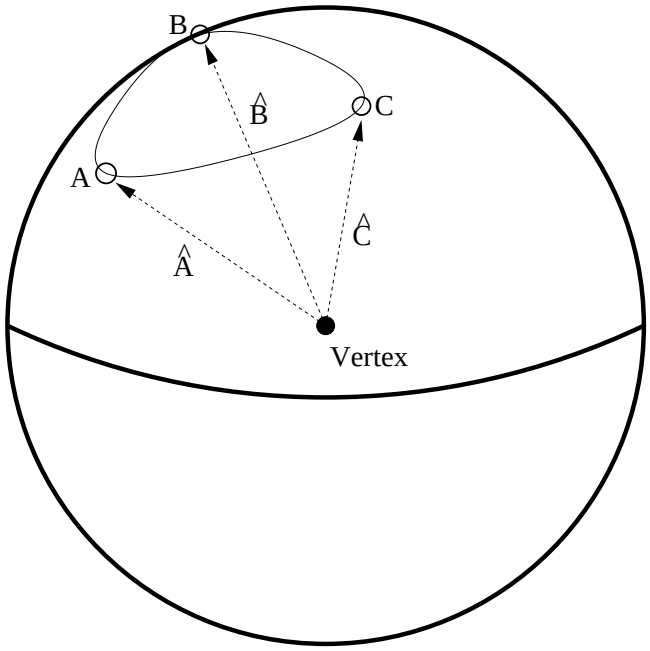

Figure 5.16: Three unit vectors are obtained from each three hit PMTs. The vertex and those three vectors give a unique solution of Cherenkov opening angle.

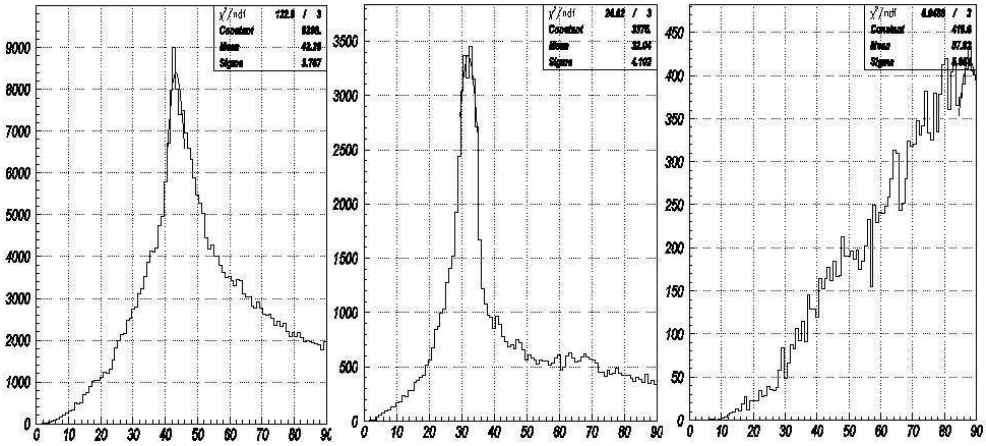

Figure 5.17: The opening angle distribution for e-like(left), μ-like(middle) and γ-like(right).

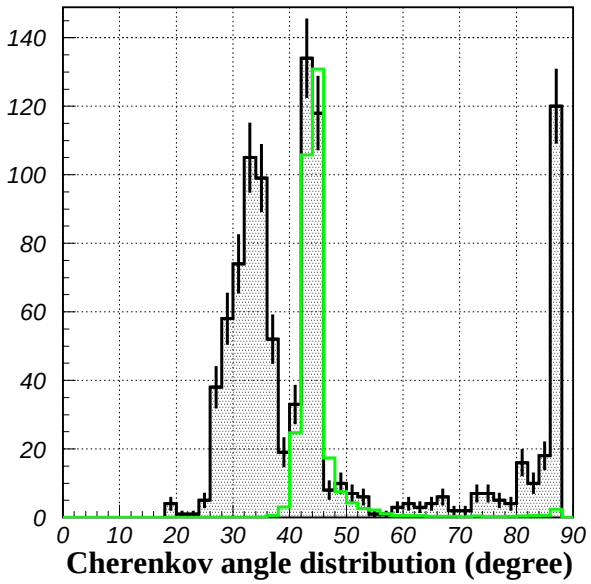

Figure 5.18: An average of the Cherenkov opening angle distribution. The shaded black histogram with error bars is SK-I data and the green histogram is the SRN MC simulation events. Clearly three peaks are shown in the real data histogram. Only the e-like peak around 42 degrees is selected.

5.5 Pion like event cut

Sometimes atmospheric neutrinos create pions in the detector. If a created pion has a high enough energy to emit Cherenkov light, it can be recognized as a SRN candidate. We cut these pions using a difference of the Cherenkov ring pattern between a pion and an electron.

Generally a pion created from an atmospheric neutrino interaction emits Cherenkov light and is soon captured by a nucleus in a water molecule. In this case, the Cherenkov ring tends to be very clear, as shown in Figure-5.19. Most of the hit PMTs are near the 42 degree line as expected from the reconstructed vertex and direction. While an electron undergoes multiple scattering in water, and thus the ring pattern looks more broad as shown in Figure-5.19.

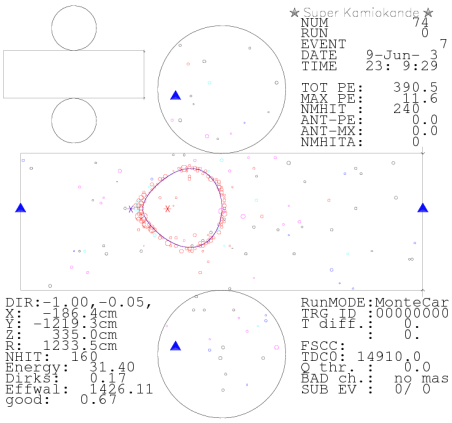

Figure 5.19: Event display of simulated pion event. Ring edge is very clear and most of the hit PMTs are around the 42 degree line.

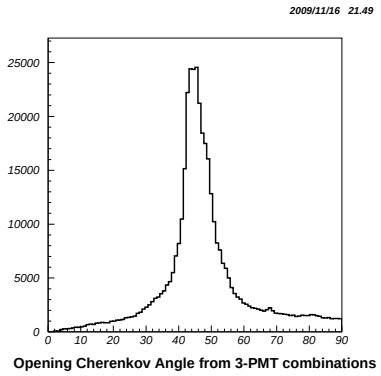

Figure 5.20: Cherenkov opening angle distribution of the pion event shown in Figure-5.19. The distribution is very sharp.

In order to evaluate the pion likelihood, we used the distribution of the Cherenkov opening angle which is explained in the Cherenkov angle cut. A distribution width of the pion event is expected to be narrower than that of the electron event. The opening angle distribution of the pion-like event and electron-like event(the event of Figure-5.19 and Figure-5.21) are shown in Figures-5.20 and 5.22, respectively. The pion-like event indicates a much narrower distribution width.

Evaluating a pion-likelihood, we took the ratio of the number of entries between +/-3 degrees and +/-10 degrees from the peak bin.

$$pilike = \frac{number\ of\ entry\ in\ \pm 3 degrees\ from\ peak}{number\ of\ entry\ in\ \pm 10\ degrees\ from\ peak} \tag{5.3}$$

The distribution of the pilike variable for the pion and electron are shown

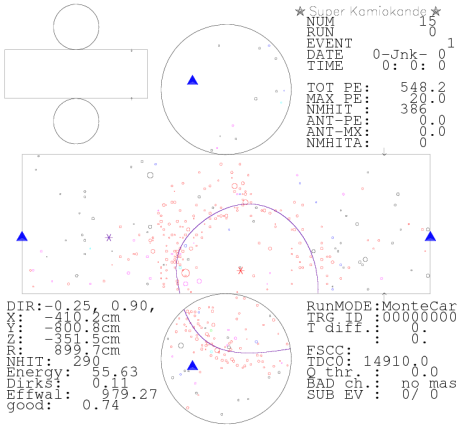

Figure 5.21: Event display of simulated electron event. Due to multiple scattering, the ring pattern becomes broader.

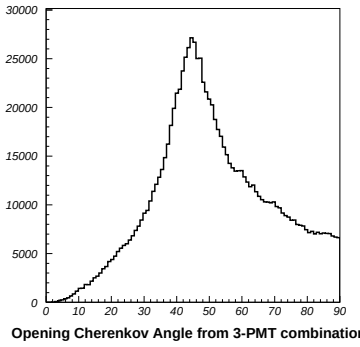

Figure 5.22: Cherenkov opening angle distribution of the electron event shown in Figure-5.21. A wider distribution than the pion event can be seen.

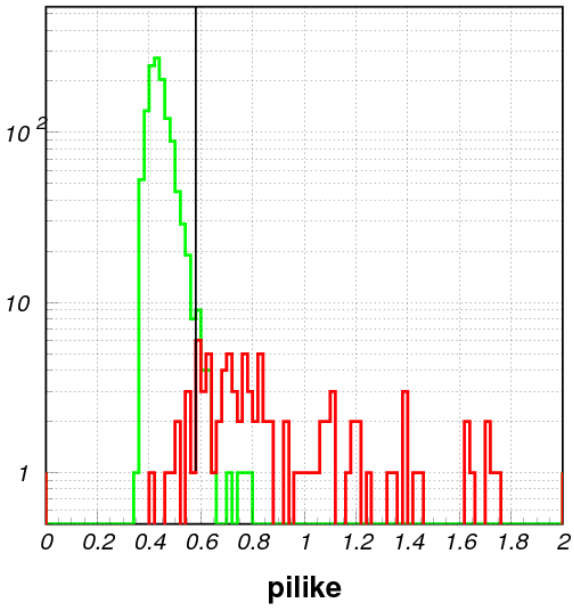

Figure 5.23: The distribution of the pilike value for pion and electron MC simulations. The green one is for electron MC and the red one is for pion MC. They are separated and the cut criteria is determined as pilike < 0.58.

in Figure-5.23. The cut point was determined to be 0.58 and the inefficiency of this cut was $\sim 1\%$.

5.6 Solar direction cut

Figure-1.2 shows the solar neutrino spectrum as predicted by the Standard Solar Model(SSM). These neutrinos, mainly from ^8B, exist up to $\sim$ 20 MeV and can be a background of our SRN search, even though it's a small flux. Since solar neutrinos are only electron neutrinos, the following electron scattering interaction is dominant. Therefore recoil electrons should keep the original direction of the neutrinos from the sun.

$$\nu + e^- \rightarrow \nu + e^- \tag{5.4}$$

We use the angle between solar direction and the reconstructed event direction(θ_{sun}) to separate solar neutrino background events and SRN candidate events. Figure-5.27 shows a θ_{sun} distribution for solar neutrino MC simulation events[2].

In the old SRN analysis, only θ_{sun} was used for the solar neutrino cut. In order to improve the cut efficiency, we developed a new method using a goodness of the direction.

Electrons in the SRN search energy region experience multiple scattering during Cherenkov light emission. Due to the multiple scattering, the ring pattern becomes broader and so the angular resolution of the scattered electron becomes worse. So the θ_{sun} distribution of scattered events is also expected to be broader. We measured multiple scattering using a hough transformation(see Figure-5.24 for the conceptual overview).

We can draw a circle around each hit PMT with the radius expected from the 42 degree opening angle. Such a circle is ideally passed through the true direction, as shown in Figure-5.24(left). Two circles give two solutions, true and fake, as shown in Figure-5.24(right). However wrong solutions are excluded because they don't fit together well with all the other solutions.

Next, a unit vector is provided from each solution and these unit vectors are connected like in Figure-5.25(top). The connected vector length becomes shorter if this event is scattered a lot. This length is compared with the length of the case in which all the vectors are on the straight path. The ratio of these two lengths is defined as a goodness of direction. This goodness distribution and the relation between the average of θ_{sun} and the direction goodness, for solar neutrino MC events, are shown in Figure-5.26. Events with worse goodness clearly give worse direction reconstruction.

We tuned the cut criteria using the following significance function.

$$sig = \frac{\epsilon}{\sqrt{\kappa S + \epsilon\alpha}} \tag{5.5}$$

Where ϵ is the efficiency of the cut for the SRN signal and background events other than solar neutrinos and κ is the effectiveness of the cut for the

[2]Bahcall 1998 spectrum is used

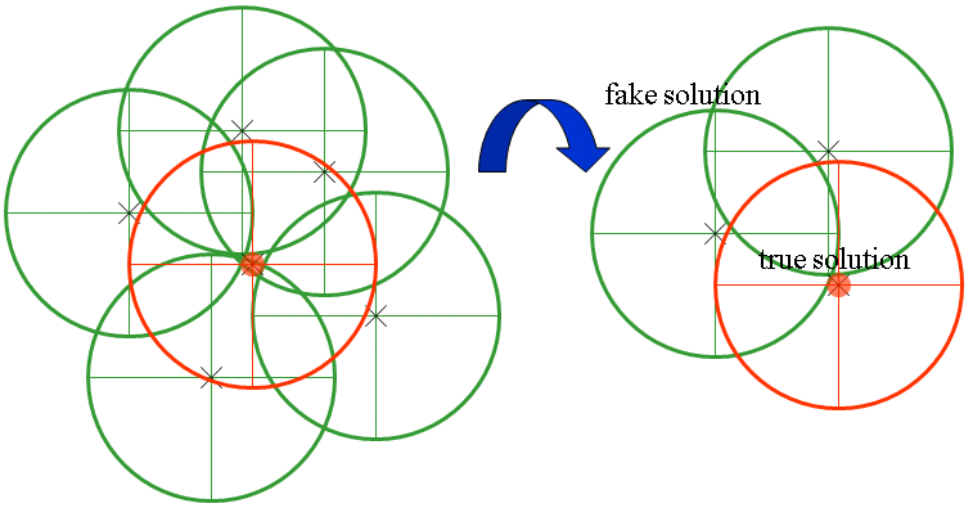

Figure 5.24: The basic idea of a hough transformation. The true direction is the cross point of each circle, which is centered at the hit PMTs, although two circle gives two solutions.

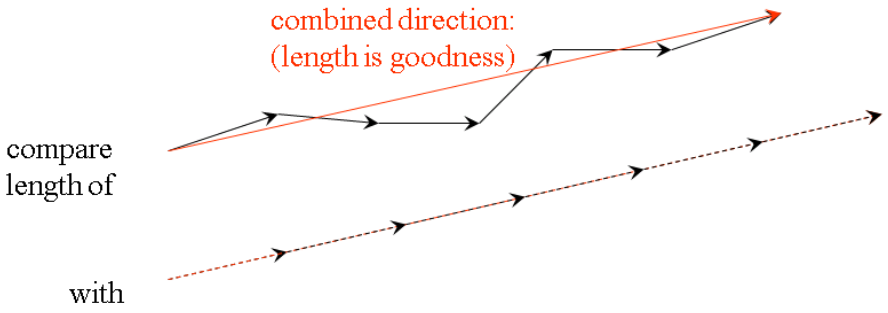

Figure 5.25: The Unit vector is obtained from each solution of two circles in Figure-5.24 and are connected. The length of this connected vector is compared with the length in the case that all unit vectors are lined straight. The ratio of these two lengths is defined as a goodness of direction.

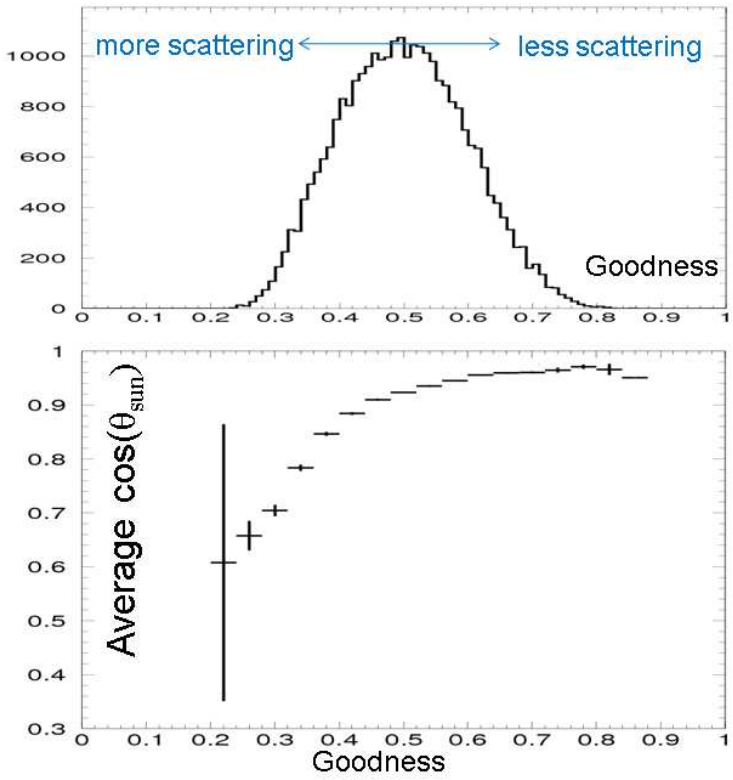

Figure 5.26: The goodness distribution of the solar neutrino MC(top) and average $\cos\theta_{sun}$ as a function of goodness(bottom). Events with worse goodness(that means more scattering) have worse angular resolution.

solar neutrino background events. S is the solar neutrino background event, estimated from the solar neutrino MC simulation. α is a background from invisible decay electron background events. To estimate this background we obtained a spectrum shape from decay electrons of stopping muons which is normalized by the number of SRN candidate events.

Figure-5.27(left) plots the θ_{sun} distribution of the solar MC events, for events with different goodness values. The right figure shows the significance as a function of θ_{sun}, for each events of a certain goodness(energy is 17-18MeV region).

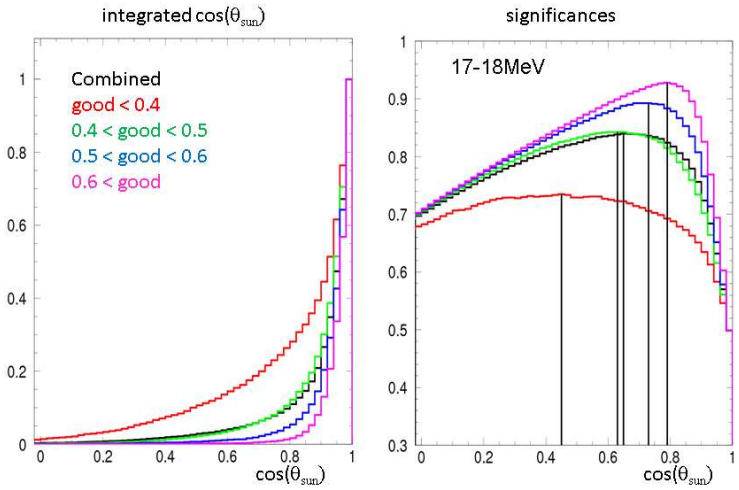

Figure 5.27: The $\cos\theta_{sun}$ distribution for the solar neutrino MC events are plotted for different goodness events(left). The significances are also plotted as a function of $\cos\theta_{sun}$(right). The Cut point was determined to maximize the significance.

The cut criteria is determined for every 1 MeV, at the peak of the significance. The cut criteria is listed in Table-5.2.

Figure-5.28 shows the $\cos\theta_{sun}$ distribution before and after the solar neutrino cut. A clear excess exists in the solar direction distribution before the solar cut. After the cut, this excess disappears, and the distribution becomes flat, similar to the distribution of the simulated SRN events(should be random direction distribution). By this reduction 24 events were rejected and the remaining solar neutrino background events were estimated to be less than 0.35 event / 1496days.

The number of PMTs in the SK-II detector were half of that of SK-I and SK-III. Therefore the energy resolution was worse and also the goodness calculation is more difficult to do. Thus we applied a more strict cut, without a goodness method for SK-II data, in order to remove all the solar neutrino background. In SK-II, the events whose energy is less than 25 MeV and $\cos\theta_{sun}$ less than 0.75, are removed. This cut criteria is strict enough and the expected number

Energy	Goodness	Cut point
16-17MeV	< 0.4	0.05
	0.4 - 0.5	0.39
	0.5 - 0.6	0.59
	> 0.6	0.73
17-18MeV	< 0.4	0.35
	0.4 - 0.5	0.61
	0.5 - 0.6	0.73
	> 0.6	0.79
18-19MeV	< 0.4	0.45
	0.4 - 0.5	0.77
	0.5 - 0.6	0.81
	> 0.6	0.91
19-20MeV	< 0.4	0.93
	0.4 - 0.5	0.93
	0.5 - 0.6	0.93
	> 0.6	0.93

Table 5.2: The list of solar direction cut criteria in SK-I and SK-III . Cut criteria is determined for each 1MeV up to 20 MeV. For the tuning, we used a solar neutrino MC simulation.

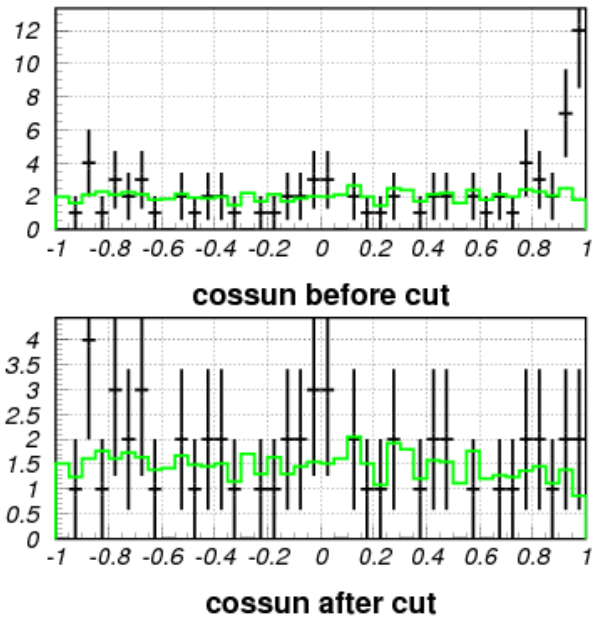

Figure 5.28: The $\cos\theta_{sun}$ distribution before the cut(top) and after the cut(bottom) in SK-I. In both figures the black markers show the distribution of real data and the green line shows the distribution of simulated SRN events.

of solar neutrino backgrounds after this cut is less than 0.2 event / 791 days, although the inefficiency of the cut is worse than that of SK-I and SK-III.

5.7 Effwall cut

The event rate near the ID wall is higher than that of inside fiducial volume due to gamma rays from the PMTs and ID structure. Also decay electrons from low energy muons come from out of the detector and can remain in our sample. Such decay electrons have a vertex near the wall.

In order to remove such backgrounds, we apply the cut using an expected travel distance from the ID wall(effwall). The schematic view of the effwall definition is shown in Figure-5.29.

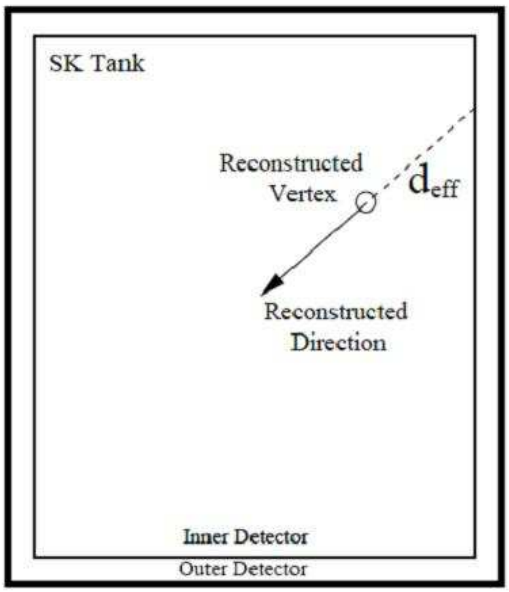

Figure 5.29: The definition of effwall. The schematic view of the definition of the effective wall distance(effwall). Effwall is defined as the distance from the reconstructed vertex of the SRN candidate event to the ID wall reversely along the reconstructed direction.

Figure-5.30 is the effwall versus the energy distribution of relic candidate events. We determined the cut criteria to remove the excess of the effwall distribution of the data. In SK-I we adopted an energy dependent cut criteria as shown in Figure-5.30. Meanwhile in SK-II, since the vertex resolution was poorer, we applied a more strict cut(effwall $>$ 450 cm in all energy region). The right figure in Figure-5.30 shows the SK-III case and an effwall $>$ 450 cm cut is needed for the energy $<$ 22 MeV region as well as effwall $>$ 300 cm above 22 MeV.

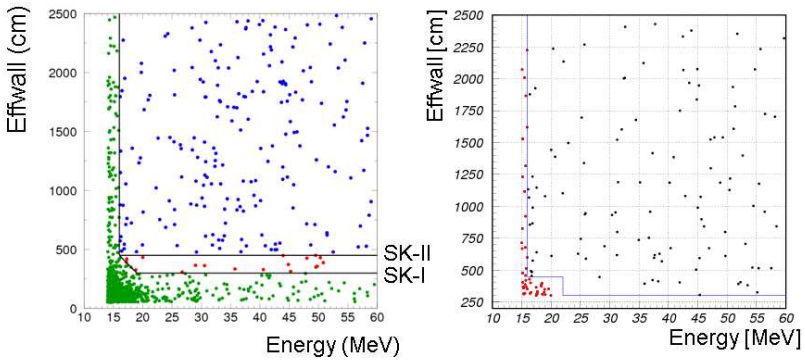

Figure 5.30: The effwall versus energy distribution for the relic candidate events in SK-I(right) and SK-III(left). The lines represent the cut criteria in each phase and the red dot is removed by this cut. In the SK-III figure, there are no events below effwall < 300 cm because we removed such events at a very Early stage of reduction in order to reduce the process time of the spallation cut.

After this cut, the effwall distribution of the data becomes consistent with that of the MC simulated SRN events(see Figure-5.31).

5.8 OD correlated event cut

The OD triggered events are removed from the data sample at the 1st stage of reduction. However the OD PMT coverage is much less than the ID and sometimes low energy cosmic ray muons can enter the detector without any OD trigger and can generate decay electrons. Those decay electrons can be a background for our analysis. However even in these cases, the OD PMTs still have been hit, although the number of hit PMTs is small. For an example of this event, see Figure-5.32.

We removed the events which have OD PMT hits having timing correlation with ID PMT hit timings and position correlations with the reconstructed vertex. To select correlated PMTs efficiently, we also used the distance from the vertex position to each PMT position(dL).

The number of OD PMT hits is obtained using PMT hit timing information and dL as follows.

- Search for a peak in the ID PMT hit timing histogram after TOF subtraction and within a 50 nsec sliding timing window.
- Count the number of PMTs in the OD timing histogram within +/- 150 nsec from the ID peak and dL < 500 cm. This number is defined as N1.
- Search for a peak in the OD PMT hit timing histogram within a 100 nsec sliding timing window.

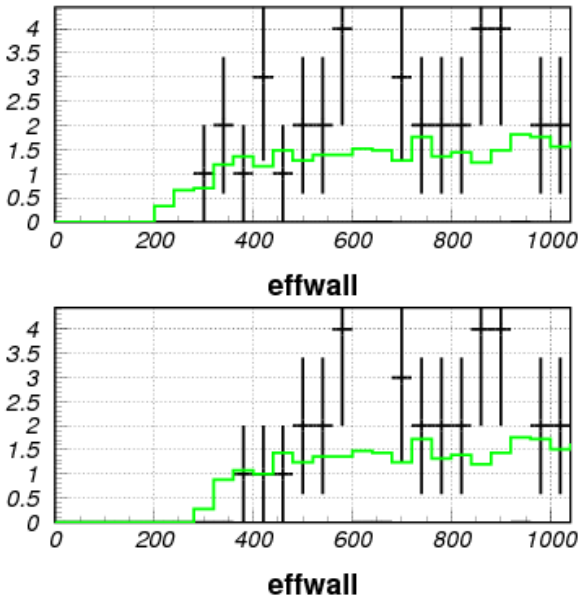

Figure 5.31: Effwall distribution in SK-I(after 2m fiducial volume cut). The marker histogram is the data and the green histogram is the MC simulated SRN events, which should be randomly distributed.

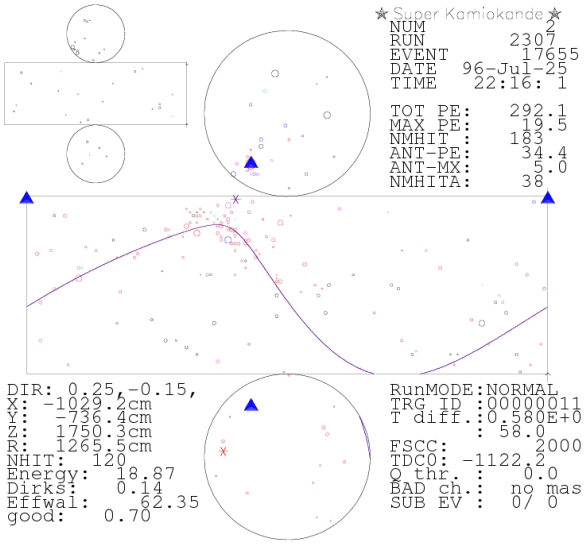

Figure 5.32: An example of a typical OD correlated event. The left top figure is the OD development view. There is a cluster hits on the top of OD.

- Count the number of PMTs within this 100 nsec timing window and dL $<$ 500 cm (defined as N2).

For a conceptual view of the peak search see Figure-5.33. If N1 $>$ 1 hit or N2 $>$ 2 hits, the event is removed as an OD correlated event. This cut criteria is tuned using the control sample of two years of SK-I real data. The N1 and N2 distributions of SK-I data are shown in Figure-5.34.

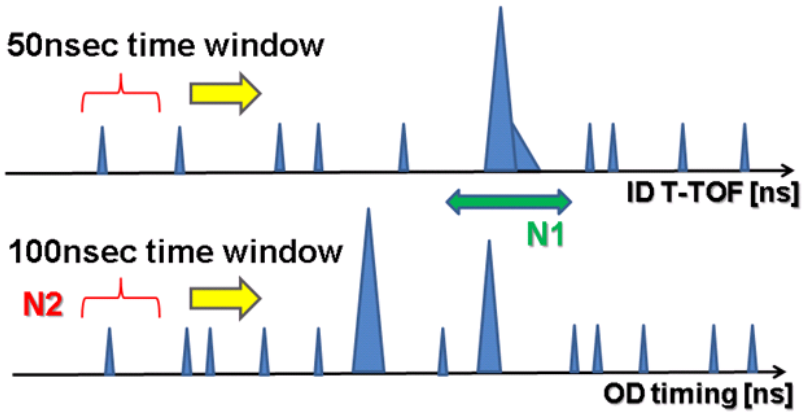

Figure 5.33: OD peak search method. Top figure shows ID hit timing after TOF subtraction. Bottom figure shows OD PMT hit timing. The ID peak search is done using a 50 nsec timing window. +/- 150 nsec from this ID peak is the first OD timing window for the OD hit PMT counting (N1). The Second OD peak is searched using 100 nsec timing window in the OD PMT hit timing distribution. The counted number of PMTs in the 2nd window is defined as N2.

The inefficiency of this cut is estimated using a random OD PMT hit sample. The cosmic-ray-muons randomly come to the detector with a rate of about 2 Hz. Using hit PMTs in these events(before muon peak), we made a random OD timing distribution of random events, and estimated the inefficiency of the cuts. Figure-5.35 shows the N1 and N2 distributions of the random events, the inefficiency is less than 1%.

5.9 Multi ring event cut

If an atmospheric neutrino creates a pion and muon simultaneously, and the energy of both resultant particles is higher than the Cherenkov threshold, two Cherenkov rings can occur with the same timing, causing double timing peaks, events which cuts cannot remove. Figure-5.36 shows a typical multi ring event with one timing peak.

To count the number of rings in each event we used “the ring counting method”, based on the Hough transformation [55] which was developed for atmospheric neutrino analysis. Details of this method are described in [54].

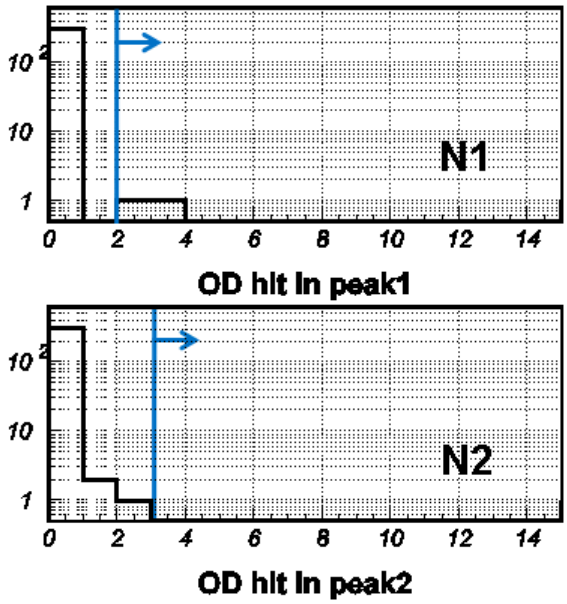

Figure 5.34: N1 and N2 distributions for SK-I data. The blue line shows the OD correlated event cut criteria. The events of N1 $>$ 1 and N2 $>$ 2 are rejected.

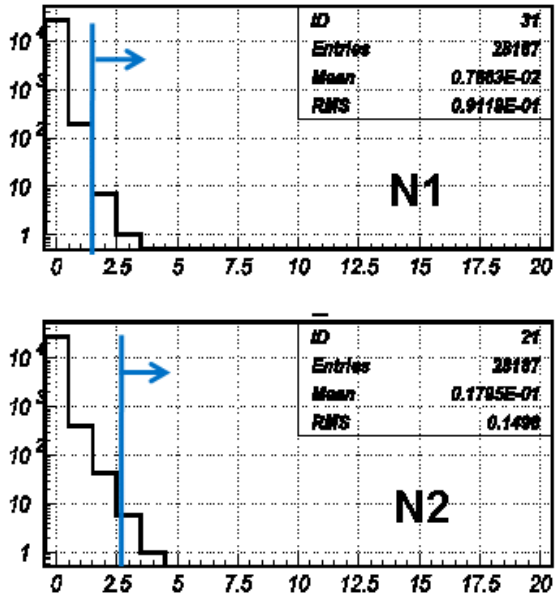

Figure 5.35: N1 and N2 distributions for the random event sample made by muon events. The inefficiency of this cut is estimated from this sample and is $< 1\%$.

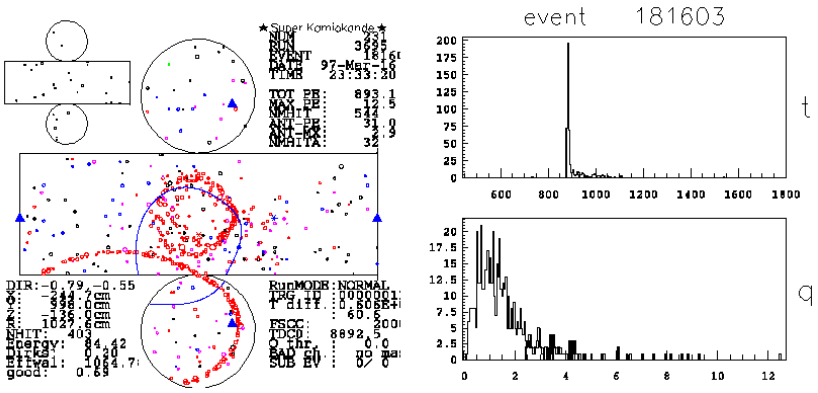

Figure 5.36: Example of a multi ring event. The left figure is the event display, two rings can clearly be seen. The right top figure is the PMT hit timing distribution of this event after time-of-flight subtraction. There is only one peak.

This ring counting method gives us the number of rings and the direction of each ring. However, for low energy electrons the ring patterns become broad due to multiple scattering causing such rings to be recognized as multi rings. In such cases, the reconstructed two ring direction is very close to the same. To save these fake two ring events, the angle between the first and second rings is required to be larger than 60 degrees. The distribution of this angle is shown in Figure-5.37.

If the reconstructed number of rings is more than two, and the angle between two of the ring's directions is more than 60 degrees, the event is removed from our data sample.

5.10 Sub-event cut

Sometimes an atmospheric neutrino interacts with an oxygen nuclei and activates it. In such cases, there will be a gamma ray event several micro seconds before the decay electron event. Tagging this pre activity allows us to remove this invisible mu-e decay background.

Also if a SRN candidate is a low energy muon, the decay electron event must exist just after the candidate event. So we also tag the post activity to remove such background events. See Figure-5.38 for an example of this event.

Additionally this cut removes the decay electron events whose parent muon only registers an SLE trigger. If other muons come to the detector within the timing window of some low energy event, which triggers only an SLE trigger, the decay electron cannot be rejected by the 50 micro second cut in the 1st reduction because this cut uses the timing difference from the previous LE/HE trigger event. Typical events of this background are shown in Figure-5.39.

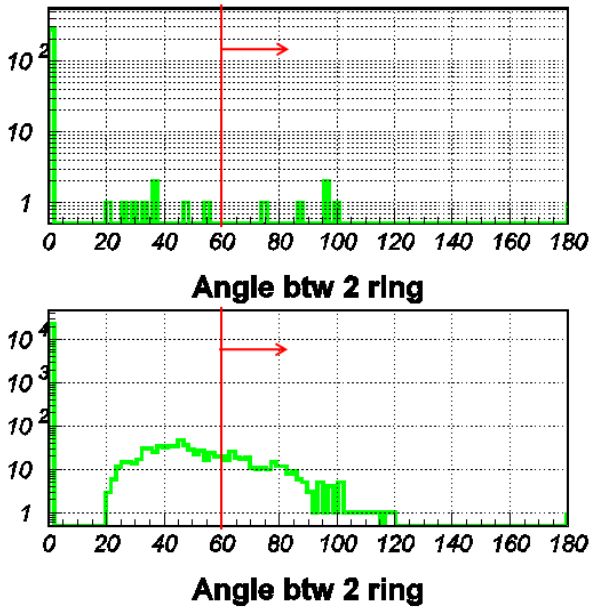

Figure 5.37: The distribution of the angle between the first and second rings. The upper figure is for SK-I real data and the lower figure is for a SRN MC simulation. If this value is larger than 60 degrees, the event is removed.

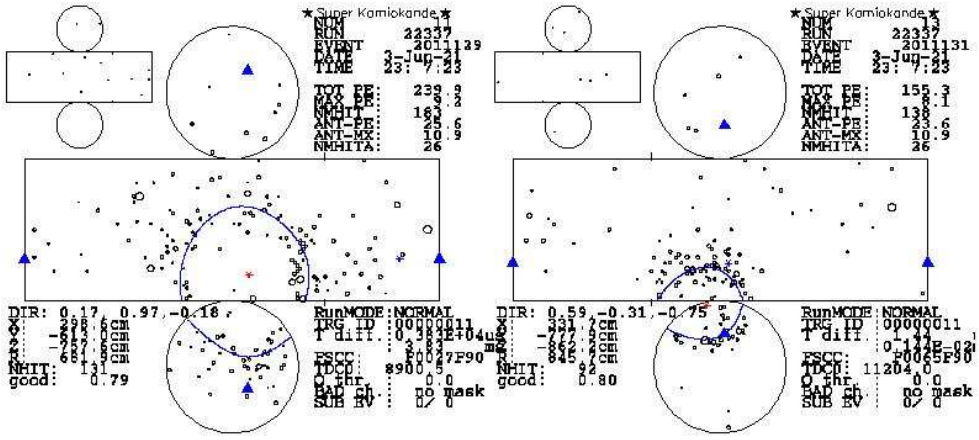

Figure 5.38: An example of an event which has a sub-event after itself. The left figure shows a SRN candidate event. The right figure is its sub-event, which occur after 1.44 μsec from the SRN candidate event.

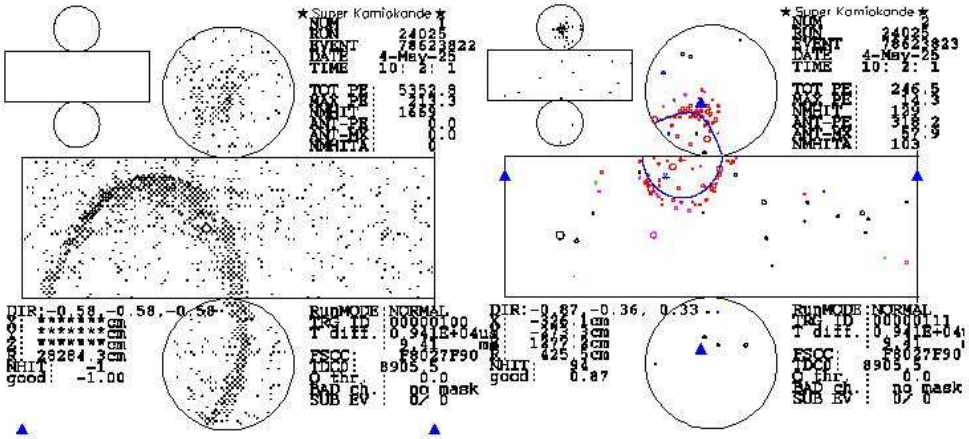

Figure 5.39: An example of a SLE triggered muon case. The left figure shows a muon which triggers only the SLE. Its decay electron is shown in right figure.

We apply a sub-event cut mainly to remove these three types of background events described above. The cut criteria is determined as follows.

1. Remove events which have pre/post activity within +/- 50μsec from a SRN candidate if the vertex of the SRN candidate event and sub-event are closer than 500cm.

2. Remove events which have SLE events within 50 μsec before the candidate event and the total charge of sub-event is larger than 1000 photo-electron.

Figure-5.40 is the vertex difference between SRN candidate events and sub-events within 50 μsec.

5.11 Summary of data reduction

In this section we summarize the data reduction process for SK-I, SK-II and SK-III. We applied various cuts to remove background events which are not true SRN signal events. The number of events at each reduction step in SK-I, SK-II and SK-III are listed in Table-5.11, 5.11 and 5.11 respectively. These numbers are counted within the fiducial volume(2m from ID wall) which an energy region between 16-90 MeV in SK-I and SK-III, and 18-82 MeV in SK-II. The energy spectrum of the data in each reduction steps is also shown in Figure-5.41, 5.42, and 5.43.

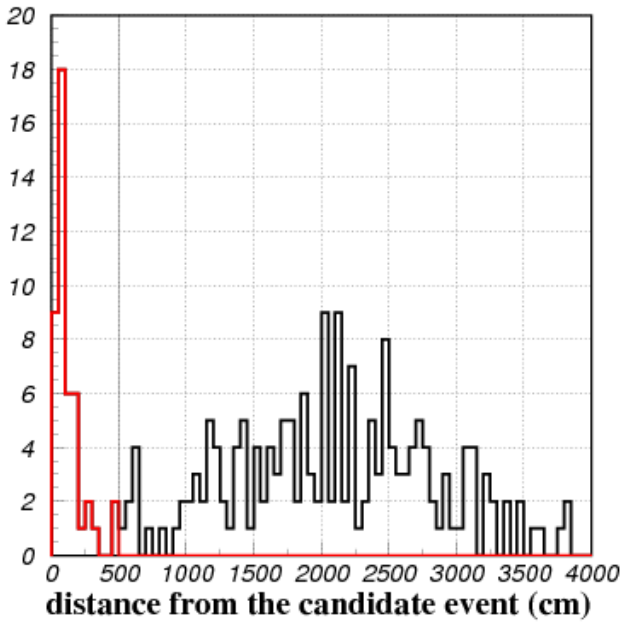

Figure 5.40: The distribution of the distance between SRN candidates and subevents. The red histogram is within the 500 cm cut criteria.

The applied reduction process was the same for SK-I and SK-III but not for SK-II. Although we improved the data reduction method to increase the efficiency for the SRN signal, it does not work for SK-II due to poor detector performance. Because the number of PMTs in SK-II was only half that of SK-I and SK-III, vertex, energy and direction resolution was worse and more backgrounds contaminated the data sample in SK-II. Therefore we applied inefficient, but strict cuts for the SK-II data. Even after these strict cuts, the SK-II data has an excess in the low energy region. This remaining background is due to spallation products and will be described in the next chapter.

The number of events after all reductions is 236 events(SK-I), 115 events(SK-II) and 102 events(SK-III). These correspond to event rates of 0.16 ± 0.01 events / day(SK-I), 0.15 ± 0.01 events / day(SK-II) and 0.18 ± 0.02 events / day(SK-III). These are consistent, within statistical error.

Reduction step	Number of event	cut efficiency
1st reduction	3970	99%
Double peak cut	3580	99%
Spallation cut	1032	85% @20MeV
Cherenkov angle cut	341	94%
effwal cut	336	97.5%
Solar cut	314	95%
OD correlated cut	312	99%
Pion like event cut	290	99%
2ring cut	283	99%
Sub-event cut cut	236	99%

Table 5.3: Number of events after each reduction step in SK-I. (16-90MeV)

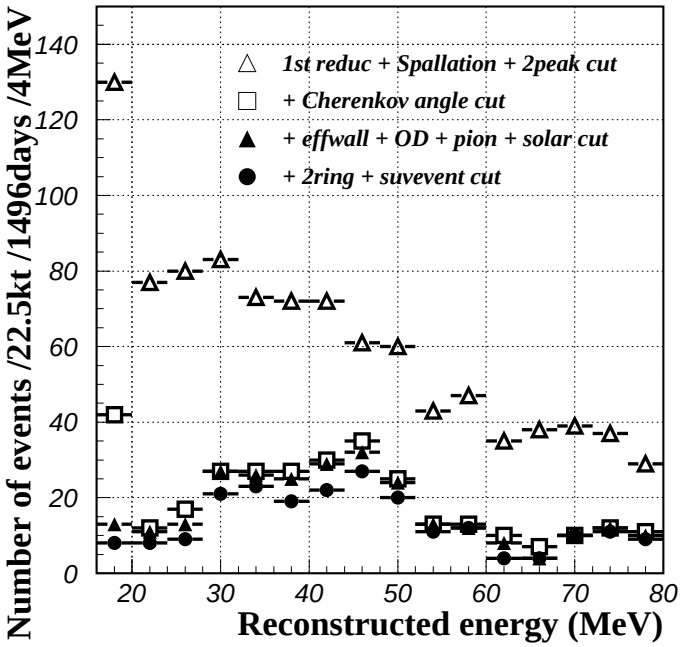

Figure 5.41: Energy spectrum for SK-I data in each reduction step. (16-80MeV)

Reduction step	Number of event	cut efficiency
1st + spallation cut	569	80% below 34 MeV
Cherenkov angle cut	241	83%
Solar direction cut	228	90%
Timing spallation cut	213	64% including normal spacut
Sub-event cut	123	99%
Effwall cut	115	93%

Table 5.4: Number of events after each reduction step in SK-II. (18-82MeV)

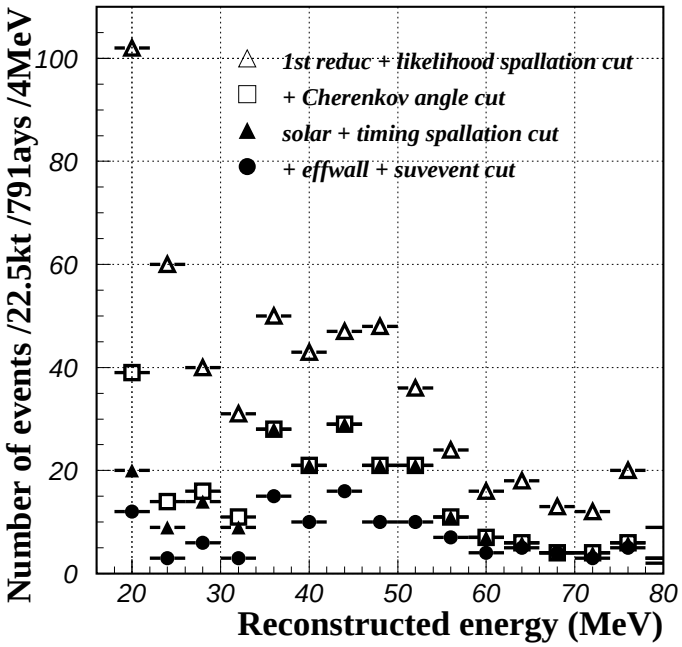

Figure 5.42: Energy spectrum for SK-II data in each reduction step. (18-82MeV)

Reduction step	Number of event	cut efficiency
1st reduction	1840	99%
Double peak cut	1592	99%
Spallation cut	393	80% @20MeV
Solar cut	348	95%
Cherenkov angle cut	153	93%
effwal cut	146	93%
OD correlated cut	145	99%
2ring cut	127	99%
Sub-event cut	102	99%

Table 5.5: Number of events after each reduction step in SK-III. (16-90MeV)

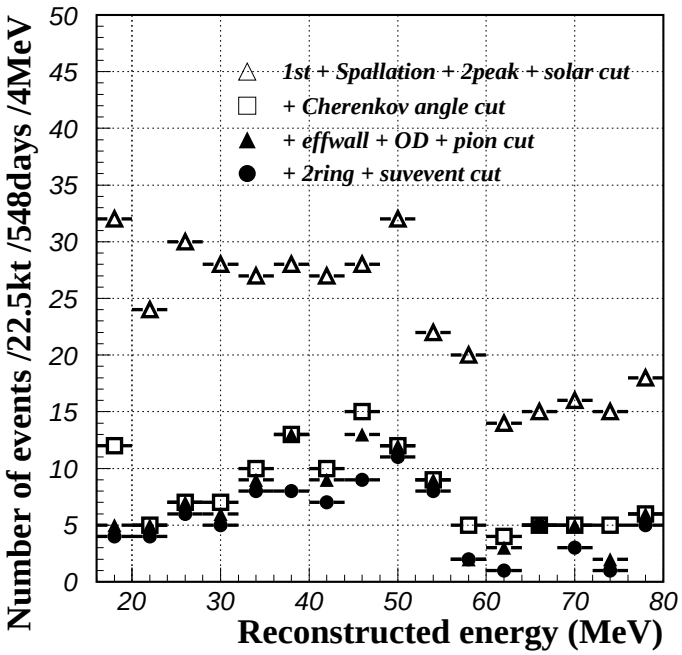

Figure 5.43: Energy spectrum for SK-III data in each reduction step. (16-80MeV)

Chapter 6

Event simulation

In order to obtain the shape of the energy spectrum of SRN events and evaluate the efficiency of the reduction process, we simulated inverse beta decay, caused by SRN's anti-electrons, using the Monte Carlo method. Similarly, background events, mainly coming from atmospheric neutrinos, were also simulated using the Monte Carlo simulation. Both simulated SRN and background events were passed through the detector simulation followed, by the same analysis chain as the real data.

6.1 Detector simulation

We simulated the propagation of the particles produced in the detector by the SRN and the atmospheric neutrino events. This simulation is described later. Our detector simulation program consists of the following three steps.

- Particle tracking through the water
- Propagation of emitted Cherenkov photons through water
- Detection of Cherenkov photons by PMTs and electronics

Particle tracking

GEANT 3.21 [59] was used for the particle tracking. It was developed at CERN and is able to simulate the electro-magnetic processes in the energy range from 10keV to 10TeV.

Figure-6.1 shows tracks of 10MeV electrons in water, as simulated by GEANT. The interactions we considered in our simulation were not only Cherenkov radiation but also Multiple scattering, Ionization, δ-ray production, bremsstrahlung and e^+ annihilation for electrons. For γ-ray, e^+ e^- pair creation, Compton scattering and the photo-electron effect were considered.

The direction of photon emission is calculated using equation 2.1. The refractive index is dependent on the photon wavelength as shown in Figure-6.2(left).

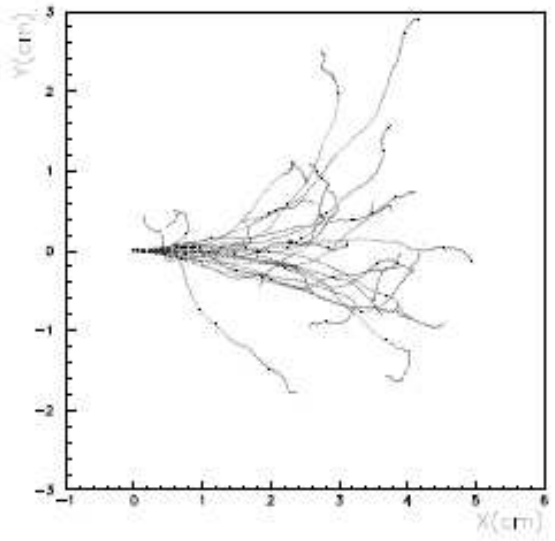

Figure 6.1: The tracks of 20 electron events with 10 MeV/c as simulated by GEANT. The generated vertex is (0,0,0) and the direction is (1,0,0).

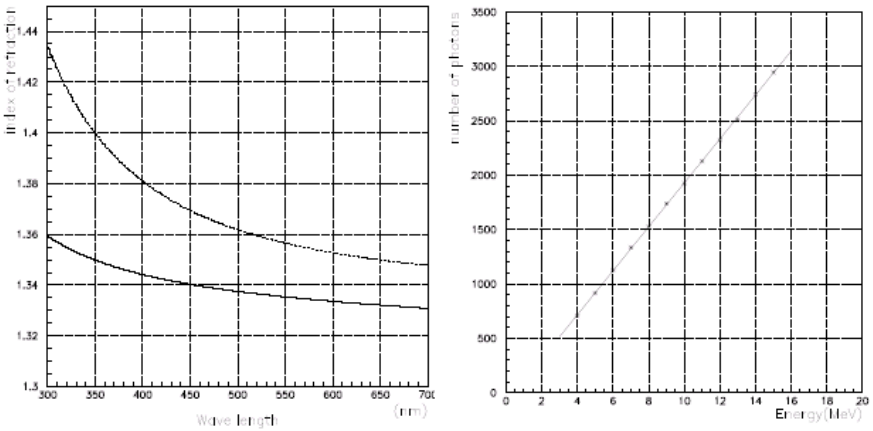

Figure 6.2: The solid line of the left figure shows the refractive index as a function of wavelength. The dashed line shows "effective index". The right figure shows the number of generated Cherenkov photons as a function of generated electron energy in the MC simulation. The solid line shows a linear fit to the points.

The wavelength of the emitted photon is calculated from equation 2.3. Figure-6.2 (right) shows the total number of Cherenkov photons emitted from an electron in water as a function of electron kinetic energy. The number of Cherenkov photons is approximately proportional to the electron energy.

Cherenkov photon tracking

The speed of light in water is dependent on the wavelength of the photons. The group velocity, v_g, is defined as

$$v_g = \frac{c}{n(\lambda) - \lambda \frac{dn(\lambda)}{d\lambda}} \tag{6.1}$$

Where c is the speed of light in vacuum, λ is the wavelength of the photon and $n(\lambda)$ is the so called effective refractive index, which depends on wavelength(see figure 6.2(left)).

The emitted photons propagate with this group velocity and are scattered and absorbed by water molecules. We considered Rayleigh scattering, Mie scattering and absorption. Since the wavelengths of the Cherenkov photons are shorter than the radius of the water molecules, Rayleigh scattering is dominant, with a $1/\lambda^4$ dependence in the shorter wavelength region. However, we also considered Mie scattering. While the effect of absorption becomes larger for longer wavelengths, its wavelength dependence is studied in [63] separately. The wavelength dependences of the water parameter coefficients are tuned by the LINAC calibration and plotted in Figure-6.3.

In addition, the water quality has changed as a function of time as shown in Figure-3.22. This change of water attenuation length is mainly coming from the absorption parameter, so we take into account the change of the absorption coefficient.

The reflection of the PMT glass and black sheet depend on photon incident angle and are also included in our simulation.

Photon detection by PMT and electronics

Once a photon comes to a PMT surface, the responses of the PMT and the electronics are simulated. First, the quantum efficiencies of the PMTs(see Figure-2.3) are considered and whether a photon-electron can be emitted or not is determined. Next, the output charge is simulated, the charge distribution of a single photo-electron is shown in Figure-2.8. The PMT hit timing is determined considering the timing resolution of the PMTs by a Gaussian random variable with a 1σ width, as shown in Figure-2.9. The dark noise is simulated by randomly distributing hits throughout the detector according to the measured of the dark noise rate.

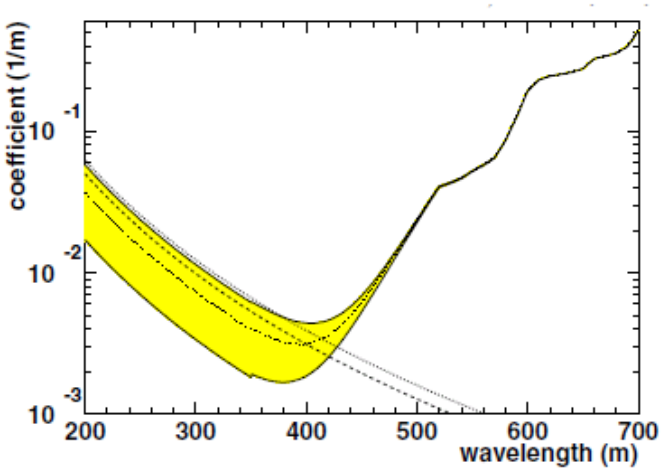

Figure 6.3: Wavelength dependence of the water parameter coefficients in SK-I. Absorption(solid line), Rayleigh scattering(dashed line) and Mie scattering(dotted line) are shown. The absorption coefficient is also a function of water transparency. The filled region shows the range of the parameters as water transparency is changed.

6.2 SRN event simulation

To perform the SRN event extraction, we need to know the energy spectrum shape of SRN events. For this purpose, SRN events are simulated by Monte Carlo simulation using nine different theoretical SRN models which predict spectrum shape and absolute flux. There is a strong model dependence in the flux prediction, but a weak dependence in the spectrum shape. The predicted SRN flux of anti-electron neutrinos by [27] and cross section of this interaction are shown in Figure-6.4(Top).

As discussed in chapter 1, most of the events we can detect in Super-Kamiokande are anti-electron neutrinos which undergo inverse beta decay.

$$\bar{\nu_e} + p \rightarrow e^+ + n \tag{6.2}$$

The inverse beta decay cross section we used is the result of the latest calculation by A.Strumia and F.Vissani [15]. Figure-6.4(Bottom) shows the expected event rate in Super-Kamiokande for 1496 days.

The positron total energy is approximated by:

$$E_e = E_\nu - \Delta \tag{6.3}$$

Where Δ is the mass difference between the neutron and the proton(1.3 MeV). This approximation is correct, as long as the neutrino energy is smaller($<1/10$) than the neutron mass. Because most of the input quantities, including the form

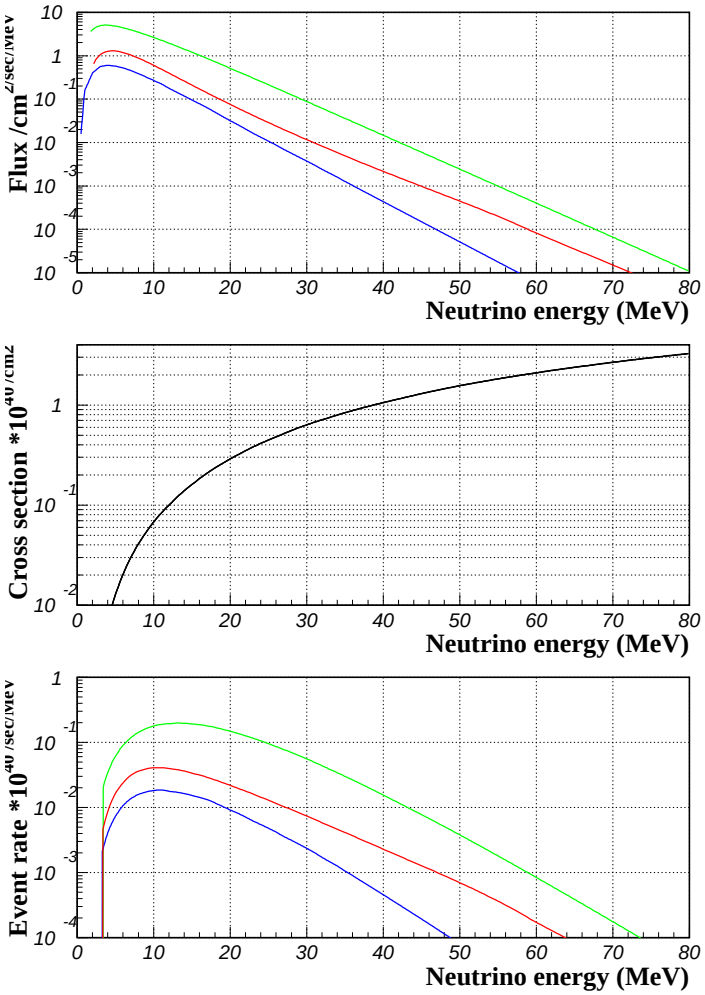

Figure 6.4: Anti-electron neutrino flux from SRN theoretical models(Top). Cross section as calculated by A.Strumia and F.Vissani [15](Middle). Event rate of SRN events in Super-Kamiokande(Bottom). Red is the LMA model[27], green is the constant SN rate model[20] and blue is the cosmic gas infall model[22].

factors, have been measured precisely, the cross section in this calculation has only 0.4% uncertainty in the low energy region.

Since supernovae have happened all over the universe, SRN events do not have a specific direction. So direction of the simulated SRN events are randomly distributed. Similarly, the vertex position of the SRN events are also given randomly inside the 32 kton full volume of the Super-Kamiokande inner detector.

Although an energy range of 16-80MeV is used for this SRN analysis, we generated positrons with energy above 5MeV. This is because the energy resolution of the detector can cause some of the SRN events with low energy to be reconstructed above our threshold. Events below 5MeV cannot contaminate above 16MeV, even considering energy resolution. Time information is given to the simulated events for considering the time variation of the water transparency. The generated number of events are; 96965 events, 69783 events and 68495 events in SK-I, SK-II and SK-III respectively.

Response of the detector was simulated using the method described in the previous section. Then output of the detector simulation was treated like real data by applying the same reconstruction and reduction tools. The spectrum shape was obtained as above, but using the assumption that a SRN was detected every 10 minutes. So normalization is needed for each model based on the expected number of events as follows.

$$N_{exp} = (\tau \times N_P) \times \int_{5MeV}^{\infty} \sigma(E_\nu)\phi(E_\nu)dE_\nu \tag{6.4}$$

Where τ is the livetime of each data taking term, 1496 days in SK-I, 791 days in SK-II and 548 days in SK-III. N_P is the number of protons in the Super-Kamiokande inner detector($= 2.17 \times 10^{33}$ protons / 32kton), which are the target for the inverse beta decay interaction. σ is the cross section of inverse beta decay $[cm^2]$ and ϕ is the predicted SRN flux $[/cm^2/sec]$.

Performing this calculation, we obtained $N_{exp} = 49.4$ events /1496days /32kt $(E_\nu > 5MeV)$ for the LMA model. The normalized energy spectrum expected in Super-Kamiokande for the LMA model, the Constant SN model and the Cosmic gas infall model are shown in Figure-6.5.

Eventually the number of expected events above 16MeV after all reductions is $N_{exp} = 10.4$ events /1496days /22.5kt (E_e >16MeV) for the LMA model. The numbers of expected events for other models are listed in Table-6.1.

6.3 Atmospheric neutrino event simulation

As described later, atmospheric neutrino events are one of the irreducible backgrounds for SRN searches in Super-Kamiokande. To understand these background we used atmospheric MC simulation events which are generated by the Super-Kamiokande group(see [64] for the detail discussion).

There are several detailed calculations of the atmospheric neutrino flux at the Super-Kamiokande site, however, we adopted the flux calculation by M.Honda

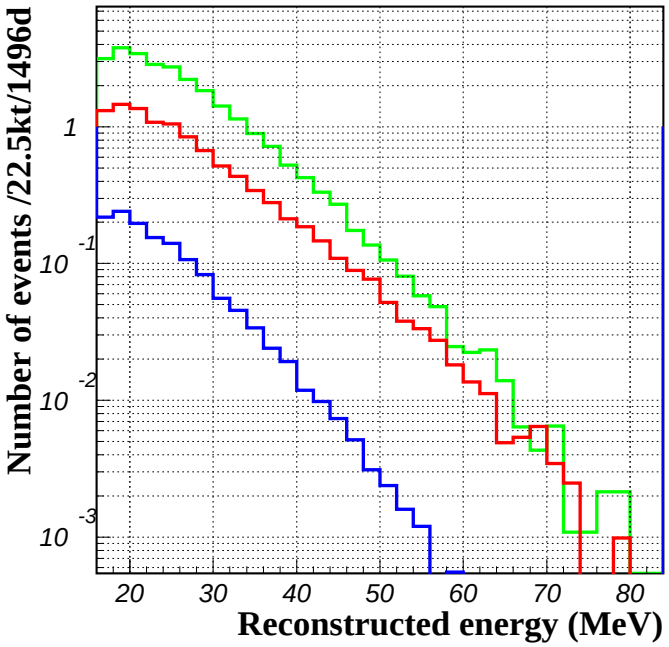

Figure 6.5: Reconstructed energy spectrum of simulated SRN events after all reductions. Red is the LMA model, green is the constant SN rate model and blue is the cosmic gas infall model.

SRN model	SK-I	SK-II	SK-III
LMA neutrino oscillation	9.9 events	3.4 events	3.5 events
Constant SN rate	26.6 events	9.1 events	9.4 events
Cosmic gas infall	1.4 events	0.5 events	0.5 events
Cosmic Chemical evolution	3.5 events	1.2 events	1.2 events
Heavy metal abundance	9.6 events	3.2 events	3.4 events
Population synthesis	3.0 events	1.0 events	1.1 events
Cosmic SF history	11.4 events	3.9 events	4.0 events
SFR constraint	3.9 events	1.3 events	1.4 events
Failed supernovae	4.3 events	1.5 events	1.6 events

Table 6.1: Expected number of SRN events for each SRN model after all reductions. The energy region is 16-80MeV in SK-I and SK-III, and 18-82MeV in SK-II. The fiducial volume is 22.5 ktons for all phases and the livetimes are 1496 days, 791 days and 548 days in SK-I, SK-II and SK-III.

et al.(Honda flux [60]) for our simulation. Figure-6.6 shows the predicted atmospheric neutrino flux. The solid line is the Honda flux we used and the other two lines are the neutrino fluxes from G.Battistoni et al.(Fluka flux [61]) and G.Barr et al.(Bartol flux [62]).

There are two large uncertainties for the atmospheric neutrino flux. The First is the uncertainty of the primary cosmic ray flux and is about 30% in the low energy region. The Second is the uncertainty of the cross section of hadronic interactions, which produce atmospheric neutrinos. This effect is about 20% and is discussed in [70].

The effect of solar activity and the geomagnetic field is about 10%, and is taken into account in the calculation. The geomagnetic field works as a shield so that cosmic rays which have relatively lower momentum cannot continue down to earth's surface. This effect is especially important for low energy region and the difference between solar maximum and solar minimum about 10% for neutrino flux.

The systematic uncertainty for the atmospheric neutrino flux described above effects the absolute flux, but does not effect the spectrum shape much. So only the spectrum shape was obtained from this MC simulation.

Atmospheric neutrinos interact with nucleons and electrons in the water, in the Super-Kamiokande detector. The neutrino interactions are simulated by NEUT [65], in our Monte Carlo simulation. NEUT was developed to study atmospheric neutrinos as a background for the nucleon decay analysis first done in the Kamiokande experiment, and was inherited to the Super-Kamiokande experiment with various modifications. In the NEUT code, the following charged current(CC) and neutral current(NC) interactions are considered.

CC/NC (quasi-)elastic scattering $\nu + N \rightarrow l + N'$

CC/NC single meson production $\nu + N \rightarrow l + N' + meson$

CC/NC deep inelastic interaction	$\nu + N \rightarrow\ l + N' + hadrons$
CC/NC coherent pion production	$\nu +\ ^{16}\mathrm{O} \rightarrow\ l +\ ^{16}\mathrm{O} + \pi$

Where N and N' are nucleons(proton or neutron) and l is a lepton.

Since the cross-section of neutrino-electron elastic scattering is about 10^3 times smaller than that of the neutrino-nucleon interactions at a neutrino energy of $\sim$1 GeV, it is neglected in our simulation.

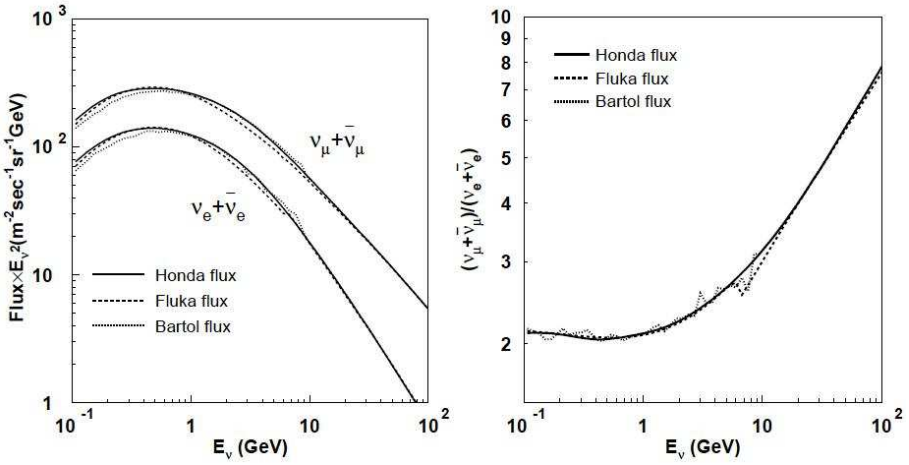

Figure 6.6: Predicted atmospheric neutrino flux(left) and the $\nu_\mu + \bar{\nu_\mu}$ and ν_e $\bar{\nu_e}$ ratio(right). The solid line shows the Honda flux which was used in our simulation. The dashed line is the calculation by G.Battistoni et al. [61] and the dotted line is G.Barr et al. [62].

Chapter 7

Remaining background

Even after applying all reduction steps, more events than expected remain as SRN candidates in the data. Figure-7.1 shows the energy spectrum of the final data sample in SK-I and SK-II. It is important to understand these irreducible backgrounds for our analysis. In this chapter, we discuss these remaining background events.

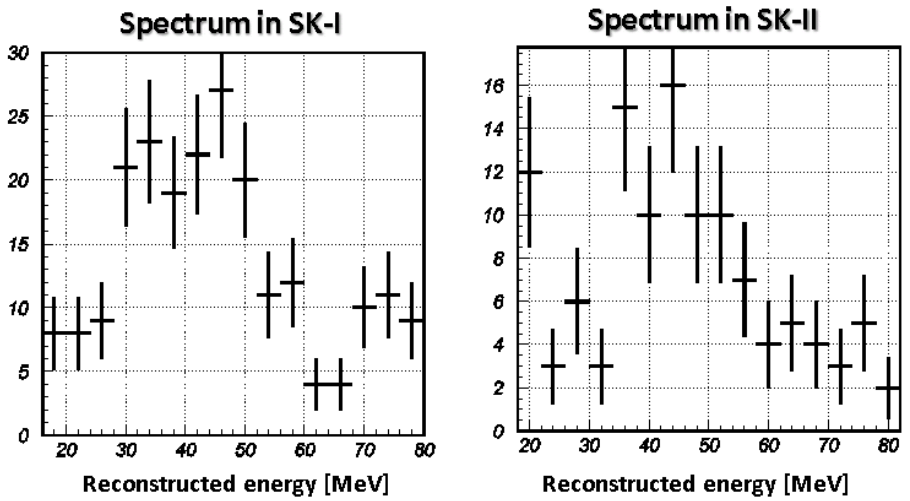

Figure 7.1: The reconstructed energy spectrum of final data sample after all of the reduction. The left figure is SK-I and the right figure is SK-II. The SK-III spectrum is similar to SK-I.

Possible backgrounds in the the analysis energy region 16-80MeV are:

- Cosmic ray muons
- Solar neutrinos
- ν_e components of atmospheric neutrinos

- Decay electrons from muons (cosmic ray muon or atmospheric ν_μ origin)
- Spallation products

Cosmic ray muons which are not rejected by the OD trigger event cut during the 1st reduction are rejected by the sub-event cut, making the cosmic ray muon background negligibly small. Solar neutrino events are rejected by the solar neutrino event cut based on the events's directional correlation with the solar direction. As described in Chapter 5, the remaining solar neutrino background is expected to be less than 0.3 events in SK-I. Spallation backgrounds are basically all removed in SK-I and SK-III, however due to the poor energy resolution in SK-II, some of spallation products remain in the final data sample. The number of remaining spallation backgrounds are estimated in this chapter.

The irreducible backgrounds in this energy region both come from atmospheric neutrinos. The origin of atmospheric neutrinos is the decay of secondary cosmic rays(e.g. pion), which are produced by the interactions of primary cosmic rays(e.g. proton) with atmospheric nuclei such as nitrogen and oxygen. For example, a $\pi^\pm$ decays through the following steps.

$$\begin{aligned} \pi^+ \rightarrow \quad & \mu^+ \quad + \nu_\mu \\ & \searrow \quad e^+ + \nu_e + \overline{\nu}_\mu \qquad (7.1) \\ \pi^- \rightarrow \quad & \mu^- \quad + \overline{\nu}_\mu \\ & \searrow \quad e^- + \overline{\nu}_e + \nu_\mu \qquad (7.2) \end{aligned}$$

That is to say, one $\pi^\pm$ can produces two ν_μ and one ν_e by this process.

Atmospheric $\nu_\mu, \bar{\nu_\mu}$ induce a muon via charged current (CC) interaction and it decays into an electron (decay-e). This is one of the irreducible backgrounds and most dominant background for SRN search in this energy region. Electrons originating from atmospheric $\nu_e, \bar{\nu_e}$ are also an irreducible background source.

In this chapter, we will discuss these backgrounds and estimate their energy spectra.

7.1 Decay electron from invisible muon

As described above, one of the irreducible backgrounds comes from decay electrons produced by invisible muons from atmospheric neutrino interactions. We evaluated the decay electron spectrum by collecting a decay electron sample using real cosmic ray stopping muons. Since these events are also decay electrons, they follow the Michel spectrum, which is expressed by the following equation:

$$\frac{dN}{dE_e} = \frac{G_F^2}{12\pi^3} m_\mu^2 E_e^2 \left(3 - \frac{4E_e}{m_\mu}\right) \quad \left(E_e < \frac{m_\mu}{2}\right) \qquad (7.3)$$

The positron from the μ^+ decay follows this function, however, in the case of μ^-, the energy spectrum is distorted because almost all of the muons are

trapped by oxygen atoms in K-shell orbits. The decay electron is influenced both by the orbital motion of the parent muon and by the electric potential of the oxygen nucleus. Figure-7.2 shows the calculated energy spectra of the decay electrons and positrons.

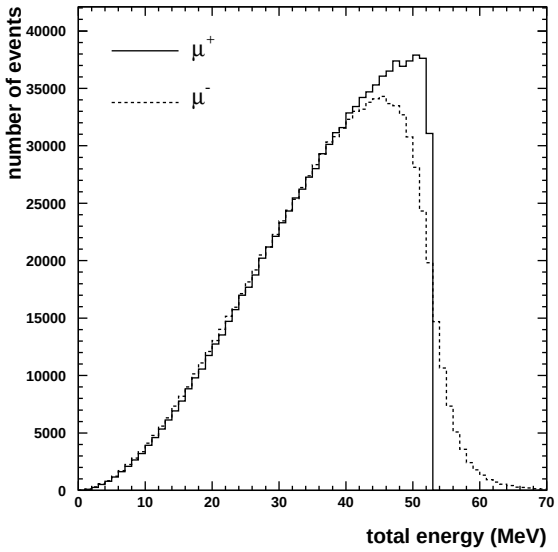

Figure 7.2: The calculated energy spectra for decay electron events in water. The solid line represents the positron spectrum and the dashed line represents the electron spectrum.

The μ^+/μ^- ratios from atmospheric neutrinos and cosmic rays are different. The primary particles of cosmic rays are mainly free protons which have positive charge. Therefore the fraction of μ^+ is larger than that of μ^- in the cosmic ray stopping muon case. While in the atmospheric neutrino's case, the ν_μ interaction is larger than $\bar{\nu_\mu}$, due to the almost twice as large cross section[69]. Figure-7.3 shows the calculated cross section of the charged current quasi-elastic interaction for ν_μ and $\bar{\nu_\mu}$. μ^- from the ν_μ interaction is greater than μ^+ in the atmospheric origin case.

Although the μ^+/μ^- ratio for the atmospheric neutrino origin and the cosmic ray origin are different its effect is not significant when determining the flux limit. Because the electric potential of the oxygen nucleus is $\sim$ 0.2 MeV, the difference in mean value of the energy spectrum for μ^+ and μ^- decays is small. The difference in energy spectrum shape mainly come from Lorentz boost of μ^-.

Considering the difference of the μ^+/μ^+ ratio, the decay electron energy spectra for both cases are obtained by MC simulation and they are plotted in Figure-7.4.

The red line shows the energy spectrum using the μ^+/μ^- ratio of atmo-

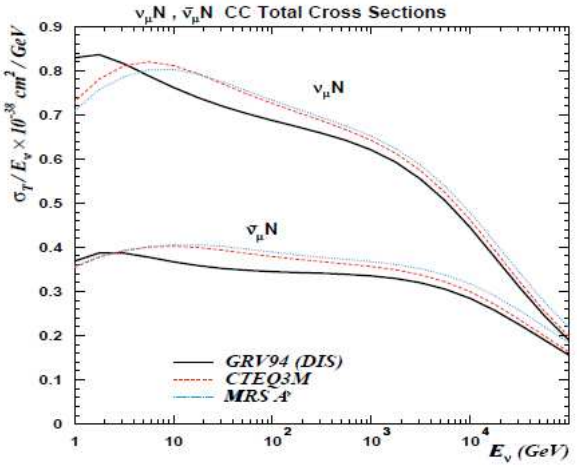

Figure 7.3: The calculated charged current interaction cross section for $\nu_\mu(\bar{\nu_\mu})$ on a nucleon.

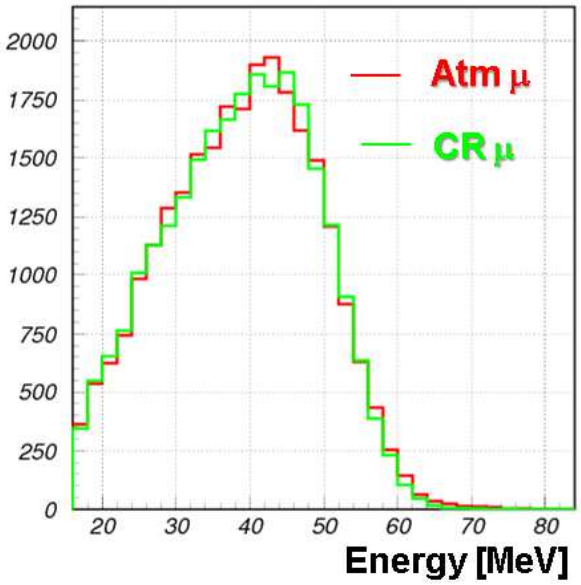

Figure 7.4: Red line shows the energy spectrum using μ^+/μ^- ratio of atmospheric neutrino case ($\mu^+/\mu^- = 0.3/0.7$) and green is that of the stopping muon case($\mu^+/\mu^- = 0.7/0.3$)

spheric neutrino case ($\mu^+/\mu^- = 0.3/0.7$) and green is that of the stopping muon case($\mu^+/\mu^- = 0.7/0.3$). The difference of mean value is less than 0.5% and they are consitent in the low energy signal region. So the decay electron spectrum obtained from the stopping muon sample can be used as a background spectrum.

We collected the decay electron sample from stopping muons with the following selection criteria:

- Time difference from stopping muon is between 3-8 μsec
- Distance from muon stopping point to vertex is closer than 500cm.

The energy spectrum after this reduction is shown in Figure-7.5 comparing with decay electron MC. The consistency was checked by calculating χ^2 using statistical error of data and MC. Calculated χ^2 is 20.1 / 13 d.o.f (∼10% probability).

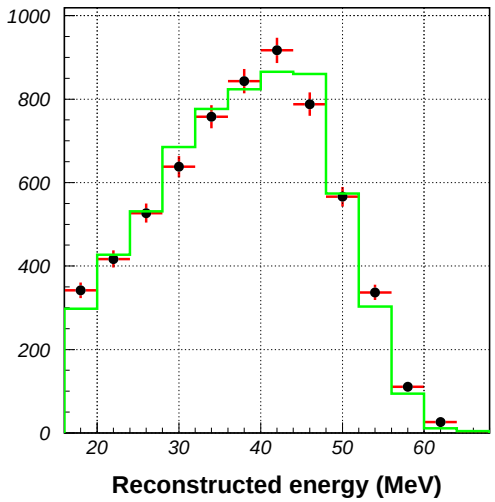

Figure 7.5: The energy spectrum for the decay electron sample obtained from stopping muon real data and decay electron MC. Calculated χ^2 is 20.1 / 13 d.o.f (∼10% probability).

Since this sample is real data, systematic error due to energy scale calibration is negligible. It does not include any gamma rays produced by NC interactions of atmospheric neutrinos. These low energy gamma rays have large uncertainty so they are considered as a systematic error and are described in section 8.3.

7.2 Atmospheric $\nu_e, \bar{\nu}_e$

Atmospheric electron-neutrinos and anti-electron-neutrinos are an irreducible background in this energy region. Atmospheric anti-electron-neutrinos interact with a proton in the water via inverse beta decay as do SRN anti-electron neutrinos. However atmospheric electron-neutrinos interact with a neutron in the ^{16}O nucleus via the following interaction:

$$\nu_e + n \rightarrow e^- + p, \quad \bar{\nu_e} + p \rightarrow e^+ + n \tag{7.4}$$

Neither can be separated from the SRN events and are dominant background sources.

Using the Honda flux and NEUT, described in section 6.3, 50 years of atmospheric neutrino MC were generated and passed through the detector simulation described in section 6.1.

The reconstructed energy spectrum of the atmospheric neutrino MC, after reductions is shown in Figure-7.6(right) for $\nu_e, \bar{\nu_e}$. The original neutrino energy for those events are also shown in Figure-7.6(left).

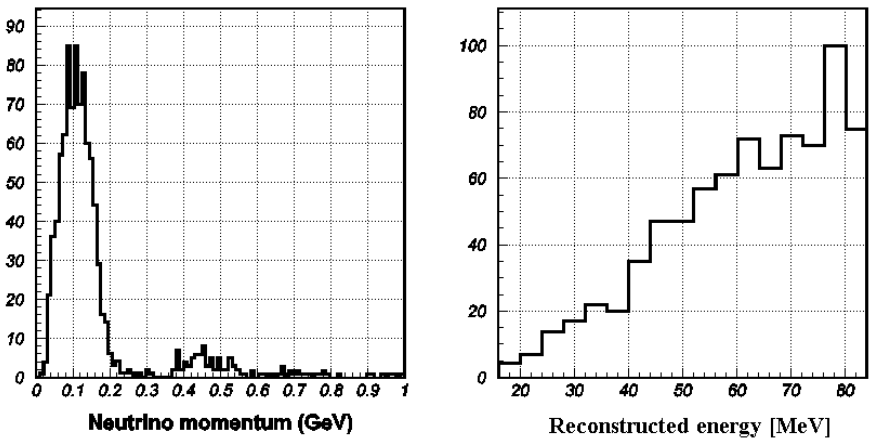

Figure 7.6: Charged current interactions are selected. The original neutrino energy for the events is shown in left figure. The reconstructed energy spectrum of atmospheric ν_e and $\bar{\nu_e}$ events after the reductions(right).

7.3 Spallation background

The backgrounds in SK-I and SK-III are understood to be due to an atmospheric neutrino origin as described in the previous section. But there is still a remaining unknown background in the low energy bin in the SK-II data as shown in Figure-7.1. There is a possibility that this excess is due to spallation backgrounds which

are reconstructed above the 18 MeV energy threshold due to the worse SK-II energy resolution, even though we adopted a tighter spallation cut in SK-II as used for the solar neutrino analysis, as described in section 5.2.2. We estimated how many spallation background events are still remaining in our final data sample after all reductions.

The spallation cut was applied in two steps for SK-II as follows.

- The cut based on the likelihood method using three variables
- The cut using time difference from the last muon ($\Delta T_{last} > 0.15$sec)

The first step of this spallation cut uses the spallation likelihood expressed by the following equation.

$$likelihood = \pounds(\Delta T) \times \pounds(\Delta L) \times \pounds(Q_{res}) \tag{7.5}$$

As described in section 5.2.1, the three variables are; ΔT which is the time difference between the preceding muon and the SRN candidate event, ΔL which is the transverse distance from the muon track to the reconstructed relic candidate position, and Q_{res} which is the residual charge that is defined as the observed total charge minus the expected charge from the muon track length.

If the likelihood value is greater than 3.9, the event is rejected by this cut. Figure-7.7 shows the energy spectrum before and after the likelihood spallation cut. 616 events(corresponding to 85%) are rejected by this cut in the 18-22MeV region. This means a lot of spallation events are included before the cut, in this bin, but are now rejected. Most of the rejected 616 events are "spallation like" events.

Using these "spallation-like" events, the time difference from preceding muons(dt) distribution is made and is shown in Figure-7.8. The red line shows the distribution for "spallation-like" events and the green line shows "random" events, which has random timing and vertex information. For the "random" event sample, we selected very low energy events near the ID wall, and generated their vertex randomly instead of the reconstructed vertex. Most of these events are gamma ray events originating at the PMTs or tank structures so that they have no correlation with the muon. The black line shows the distribution of "spallation-like-random", which is called the "true spallation".

The obtained ΔT distribution for the "true spallation" has events above 0.15 seconds. These events pass the second spallation cut using ΔT, and remain in the final sample if the likelihood spallation cut cannot reject them. We estimated how many "true spallation" events were remaining after both spallation cuts.

To do this, we need to know the likelihood distribution for "true spallation" events. We estimated this likelihood distribution by generating a spallation MC based on the ΔT, ΔL and Q_{res} distribution of "true spallation".

We started from making the ΔL and Q_{res} distribution using a "Spallation-like" sample with all the preceding muons occurring within 100 seconds. The

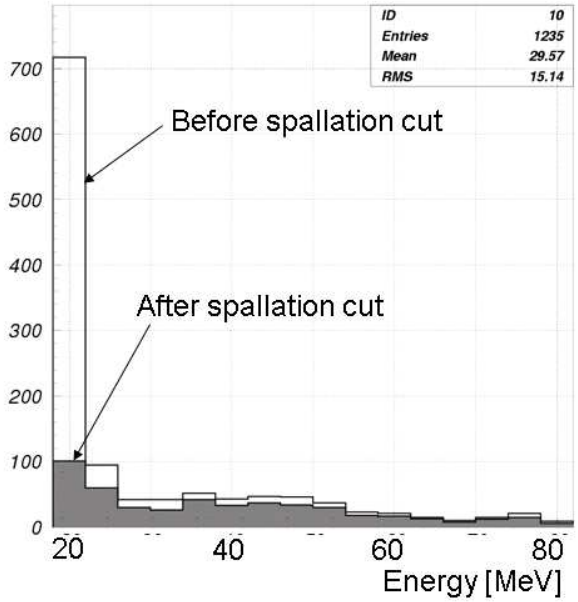

Figure 7.7: The energy spectrum of the SK-II data, before and after spallation cut.

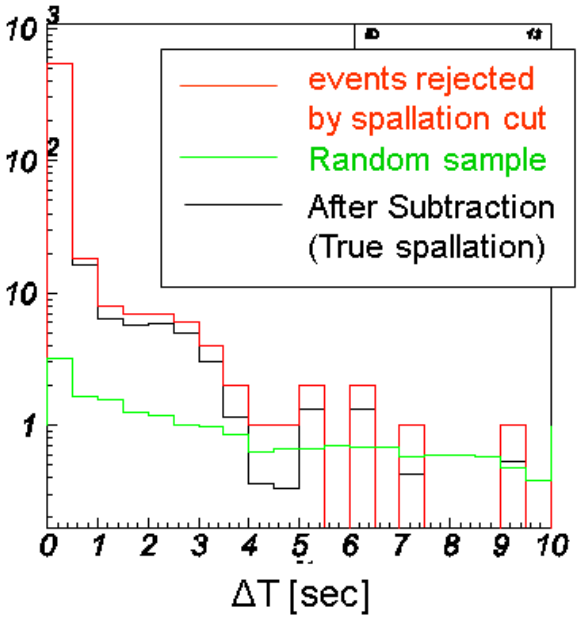

Figure 7.8: The distribution of time difference from the last muon (dt_{last}).

distribution is made in two categories, one is "on-time"($0.1sec > \Delta T > 0.0sec$) and the other is "off-time"($100.0sec > \Delta T > 90.0sec$). Figure-7.9 shows the ΔL and Q_{res} distribution, the green line is "on-time", the red line is "off-time", and the black line is the "true spallation" which was made by the "on-time - off-time" after normalization by time as follows.

$$\Delta L(truespallation) = \Delta L(on-time) - \Delta L(off-time) \times \frac{0.1[sec]}{10.0[sec]} \quad (7.6)$$

$$Q_{res}(truespallation) = Q_{res}(on-time) - Q_{res}(off-time) \times \frac{0.1[sec]}{10.0[sec]} \quad (7.7)$$

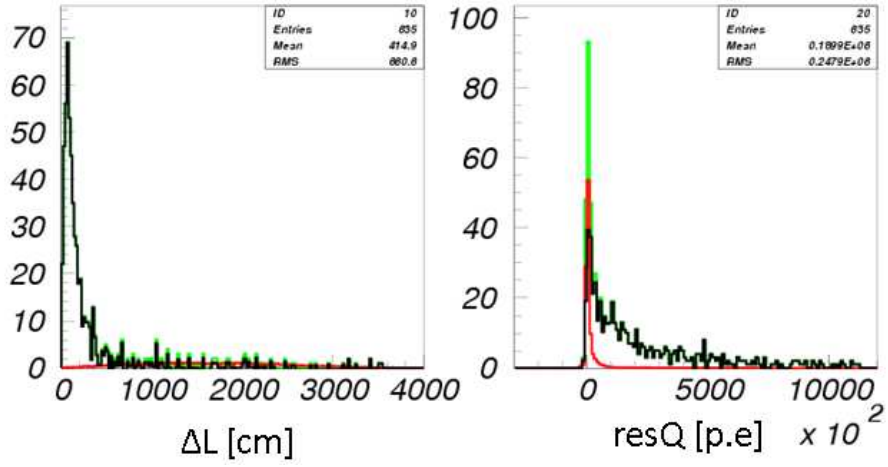

Figure 7.9: ΔL, Q_{res} distribution. Green is "on-time", red is "off-time" and black is "true spallation" defined by "on-time - off-time".

By the method described above, we obtained all of the distributions needed for the simulation of the spallation likelihood distribution. The random variables of ΔT, ΔL and Q_{res} were generated following the distribution of "true spallation". This calculation was done for every 0.6 second bin of the ΔT distribution. The center value of each bin is used as ΔT for the spallation likelihood calculation. The results of the likelihood simulation, in the case of $\Delta T = 0.375$ seconds and 0.9 seconds, are shown in Figure-7.10. The cut point in both is $likelihood < 3.9$, so that 9.7% and 10.2% of the simulated events can pass the likelohood spallation cut, respectively. The results in other ΔT bins are listed in Table-7.3. Integrating the number of events passing through the spallation cut, for $\Delta T > 0.15$ second, gives a total of 9.2 events which can remain in the data sample after the spallation cut in the 18-22MeV region.

Because this number of events is just after the spallation cut, we multiplied the efficiency($\approx$67%) of the other cuts to evaluate the number of spallation

background events in the final data sample. This analysis was also done using 622 days of SK-II data, although the SK-II data was collected for 791 days overall. Considering the cut efficiency and livetime normalization, the expected number of spallation background events in the final data sample in each energy bin was calculated and is listed in Table-7.3. In the 18-22MeV region, 7.8 spallation events are expected to exist in our final data sample for SK-II.

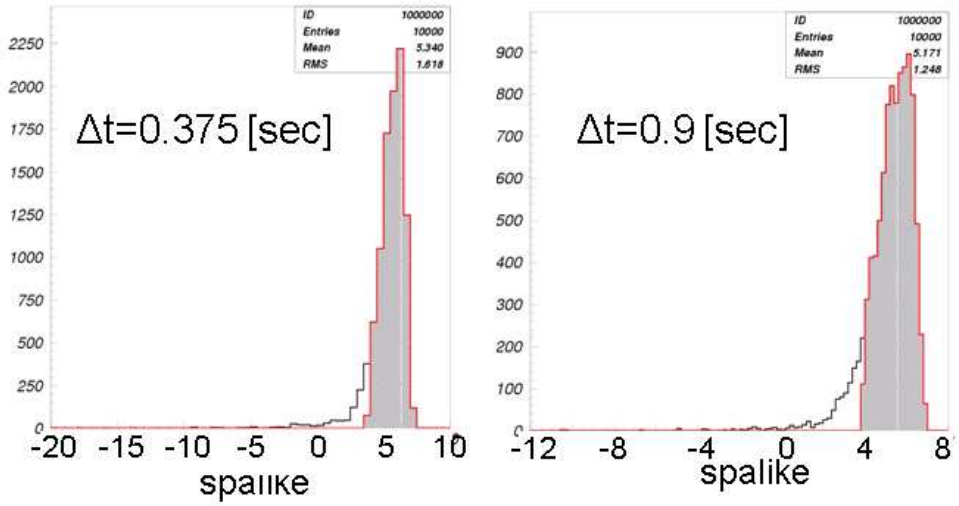

Figure 7.10: The simulated likelihood distribution for "true spallation" events. The left figure is the case of $\Delta T = 0.37$ seconds and the right figure is $\Delta T = 0.9$ seconds. The shaded region is rejected by the spallation cut.

Remaining spallation in SK-I and SK-III

Most of the spallation backgrounds must be rejected by the spallation cut in SK-I and SK-III. Looking at the dt and dL_{trans} distributions, there is no strong evidence for any remaining spallation events. If spallation is long lived and the fit is poor, it can be missed. Even considering that case, remaining spallation events are less than one or two both in SK-I and SK-II. In our analysis, the remaining backgrounds are assumed as signals. So even if there are remaining spallation events, the obtained flux upper limit should be a conservative result.

ΔT	# of "true spallation"	pass rate [%]	remaining events
0.0 - 0.15	517.3	0.0	0.0
0.15 - 0.6	26.1	9.7	2.5
0.6 - 1.2	12.3	10.2	1.3
1.2 - 1.8	8.09	11.9	1.0
1.8 - 2.4	6.65	12.7	0.8
2.4 - 3.0	5.76	13.4	0.8
⋮	⋮	⋮	⋮
Total	593.5	1.6%	9.2

Table 7.1: Expected number of remaining events in the final data sample for each time bin. The energy range is between 18MeV and 22MeV. The events in 0.0 - 0.15 second bin are rejected by the second spallation cut using the timing difference from the muon.

Energy [MeV]	Number of remaining events
18-22	7.8
22-26	0.5
26-30	0.2
> 30	≈ 0

Table 7.2: Number of expected events in the final data sample for each energy bin. These values are estimated by integrating the number of remaining events in each timing bin and multiplying the efficiency of the other cuts. The expected livetime is 791 days of all SK-II period.

Chapter 8

Systematic error estimation

Since the data statistics are not large, the effect of most systematic errors is not significant. But in order to extract SRN signal more correctly, we considered three non-negligible source of uncertainty in this analysis. The first is the uncertainty on the signal efficiency estimation originating from the difference between data and MC. The second is the energy scale uncertainty. This is important because the SRN spectrum is "soft" meaning that the number of expected events can be strongly affected by the energy scale. Finally the third is the background shape error on the decay electron spectrum. Since this spectrum is made from a pure decay electron sample, we need to consider events originating from atmospheric neutrino interactions (e.g. gamma rays from NC interaction).

8.1 The uncertainty for signal efficiency

The uncertainty on the SRN signal efficiency is evaluated as described below.

The cross section of inverse beta decay is important because it affects the detection efficiency directly. As described in [15], most input quantities have been measured precisely. The cross section uncertainty is approximated by 1% $\times(E_\nu/40MeV)^2$. The SRN spectrum decreases with increasing energy and most part of the SRN flux is bellow 40 MeV so the systematic error originating from cross section uncertainty is less than 1%.

The uncertainty from each reduction step are estimated by applying the same reduction to LINAC data and LINAC MC and comparing the difference of their efficiency. The uncertainty of solar neutrino event cut are negligible, because θ_{sun} distribution must be flat for SRN signal even if the angular resolution is different for data and MC. The spallation cut uncertainty is estimated by calculating the efficiency in the several different period. Other cuts, for example OD correlated event cut, double T peak cut, sub-event cut and so on, have small inefficiencies for SRN signal ($\sim$1% or less). Therefore, we took the quadratic sum of these errors as a single error source on the inefficiency. The estimated uncertainties for each reduction step are listed in Table-8.1.

reduction	SK-I	SK-II	SK-III
Cherenkov angle cut	±0.4%	±3.0%	±0.3%
Effwall cut	±0.5%	±1.0%	±0.3%
Spallation cut	±3.0%	±0.4%	±1.0%
Pion-like event cut	±0.2%	-	±0.5%
Other cuts	±2.0%	±1.3%	±1.7%

Table 8.1: The systematic uncertainty from each reduction step in this analysis.

The uncertainties on the fiducial volume and detector livetime calculation are quoted from the solar neutrino analysis in Super-Kamiokande[38, 39, 40], because the data set and vertex reconstruction program are same as that of solar neutrino analysis although applied cut is different.

In total, the uncertainty on the SRN signal efficiencies are ±3.9% in SK-I, ±4.6% in SK-II and ±2.5% in SK-III. The uncertainty described above are summarized in Table-8.1.

	SK-I	SK-II	SK-III
Cross section of inverse β decay	±1.0%	±1.0%	±1.0%
Reduction efficiency	±3.6%	±4.3%	±2.1%
Fiducial volume	±1.3%	±1.1%	±1.0%
Livetime calculation	±0.1%	±0.1%	±0.1%
Total	±3.9%	±4.6%	±2.5%

Table 8.2: The summary table of systematic uncertainty in our analysis.

8.2 Energy scale uncertainty

The energy scale uncertainty is obtained from energy scale calibration as described in section 3.7. The systematic uncertainty for energy scale is calculated considering the effect of position dependence of energy scale, time variation of energy scale, MC tuning accuracy, electron beam determination in LINAC calibration and directional dependence of energy scale. As shown in table 3.3, obtained uncertainty is 0.64% in SK-I, 1.4% in SK-II and 0.53% in SK-III respectively. To be conservative, we applied a larger uncertainty, 1% in SK-I and SK-III and 1.5% in SK-II.

8.3 Background shape error

As described in section 7.1, the decay electron spectrum is obtained from decay electron real data from cosmic ray stopping muon data. This sample does not

include other atmospheric neutrino interactions. These low energy neutral current interactions have large uncertainties so we considered them as a systematic error on the background shape.

In order to investigate the influence of atmospheric neutrino interactions, atmospheric neutrino MC events were classified into four groups, based on the original neutrino flavor. Each group is further classified into six groups based on the interaction mode. The energy spectrum obtained for each group is shown in Figure-8.1, 8.2(ν_e, $\bar{\nu_e}$), Figure-8.3, 8.4(ν_μ, $\bar{\nu_\mu}$). The interaction mode is defined in Table-8.3(for ν_e and $\bar{\nu_e}$) and 8.4(for ν_μ and $\bar{\nu_\mu}$).

id	electron neutrino interaction	id	anti-electron neutrino interaction
10	$\nu_e + n \to e^- + p$	20	$\bar{\nu_e} + p \to e^+ + n$
11	$\nu_e + p \to e^- + p + \pi^+$ $\nu_e + n \to e^- + p + \pi^0$ $\nu_e + n \to e^- + n + \pi^+$ $\nu_e + {}^{16}O \to e^- + {}^{16}O + \pi^+$	21	$\bar{\nu_e} + p \to e^+ + n + \pi^0$ $\bar{\nu_e} + p \to e^+ + p + \pi^-$ $\bar{\nu_e} + n \to e^+ + n + \pi^-$ $\bar{\nu_e} + {}^{16}O \to e^+ + {}^{16}O + \pi^-$
12	$\nu_e + p(n) \to e^- + p(n) + multi\ \pi$ $\nu_e + n \to e^- + p + \eta^0$ $\nu_e + n \to e^- + \Lambda + K^+$ $\nu_e + p(n) \to e^- + p(n) + mesons$	22	$\bar{\nu_e} + p(n) \to e^+ + p(n) + multi\ \pi$ $\bar{\nu_e} + p \to e^+ + n + \eta^0$ $\bar{\nu_e} + n \to e^+ + \Lambda + K^-$ $\bar{\nu_e} + p(n) \to e^+ + p(n) + mesons$
13	$\nu_e + n \to \nu_e + n + \pi^0$ $\nu_e + p \to \nu_e + p + \pi^0$ $\nu_e + n \to \nu_e + p + \pi^-$ $\nu_e + p \to \nu_e + n + \pi^+$ $\nu_e + {}^{16}O \to \nu_e + {}^{16}O + \pi^0$	23	$\bar{\nu_e} + n \to \bar{\nu_e} + n + \pi^0$ $\bar{\nu_e} + p \to \bar{\nu_e} + p + \pi^0$ $\bar{\nu_e} + n \to \bar{\nu_e} + p + \pi^-$ $\bar{\nu_e} + p \to \bar{\nu_e} + n + \pi^+$ $\bar{\nu_e} + {}^{16}O \to \bar{\nu_e} + {}^{16}O + \pi^0$
14	$\nu_e + n(p) \to \nu_e + n(p) + multi\ \pi$ $\nu_e + n \to \nu_e + n + \eta^0$ $\nu_e + p \to \nu_e + p + \eta^0$ $\nu_e + n \to \nu_e + \Lambda + K^0$ $\nu_e + p \to \nu_e + \Lambda + K^+$ $\nu_e + n(p) \to \nu_e + n(p) + mesons$	24	$\nu_e + n(p) \to \nu_e + n(p) + multi\ \pi$ $\bar{\nu_e} + n \to \bar{\nu_e} + n + \eta^0$ $\bar{\nu_e} + p \to \bar{\nu_e} + p + \eta^0$ $\bar{\nu_e} + n \to \bar{\nu_e} + \Lambda + K^0$ $\bar{\nu_e} + p \to \bar{\nu_e} + \Lambda + K^+$ $\bar{\nu_e} + n(p) \to \bar{\nu_e} + n(p) + mesons$
15	$\nu_e + p \to \nu_e + p$ $\nu_e + n \to \nu_e + n$	25	$\bar{\nu_e} + p \to \bar{\nu_e} + p$ $\bar{\nu_e} + n \to \bar{\nu_e} + n$

Table 8.3: The definition of the id number in each interaction mode for electron and anti-electron neutrinos.

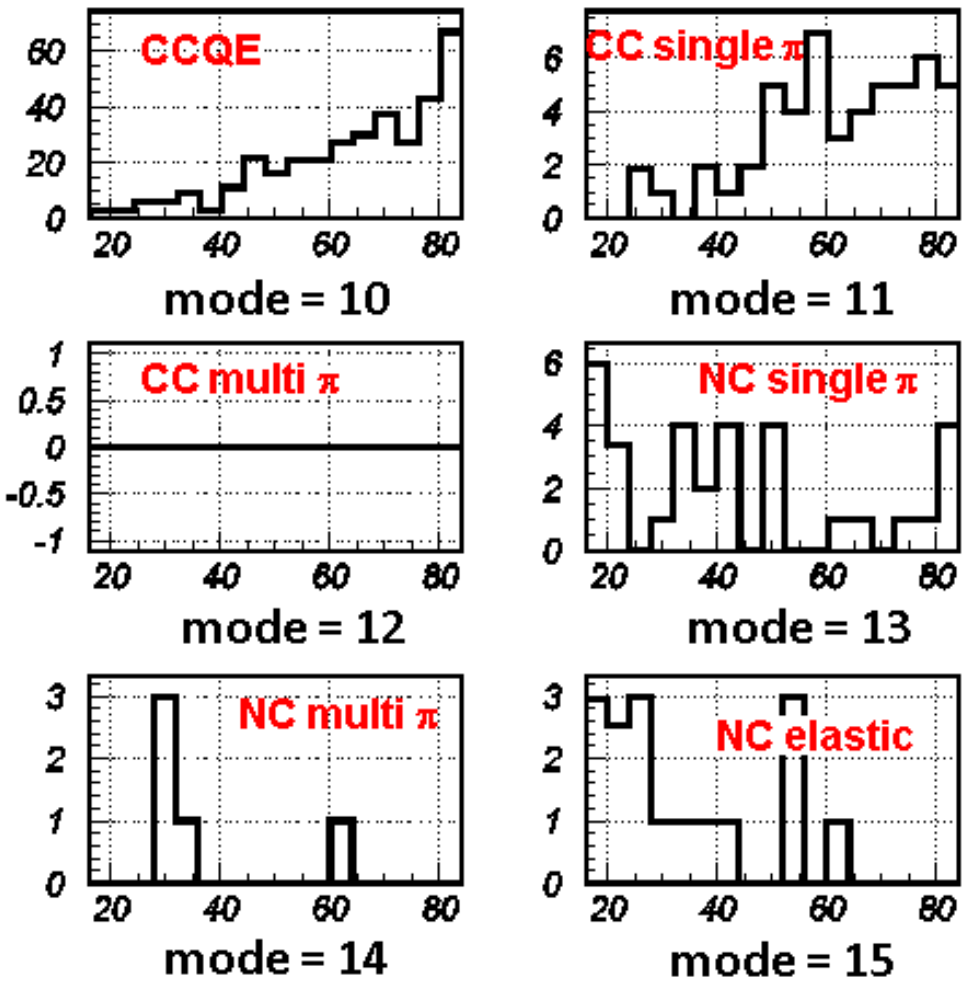

Figure 8.1: The energy spectrum of atmospheric electron neutrinos for each interaction mode using 50years of MC. The horizontal axis is the reconstructed energy. The definition of the id number of interaction modes are described in Table-8.3.

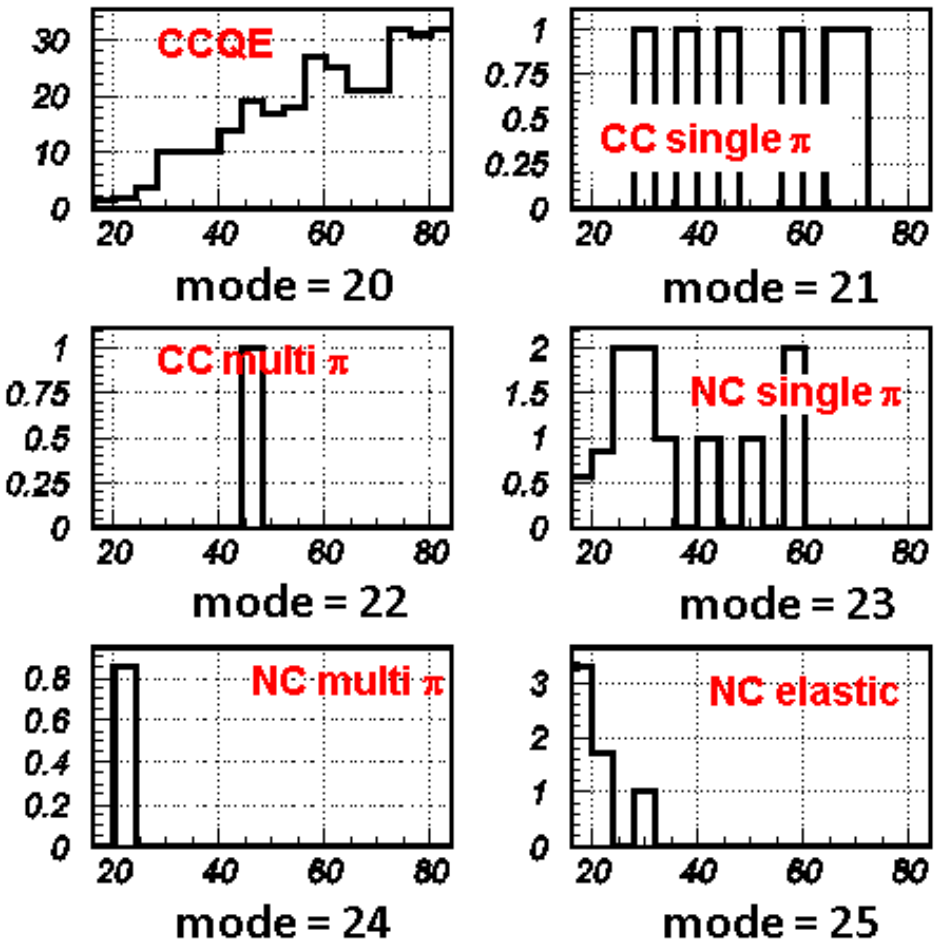

Figure 8.2: The energy spectrum of atmospheric anti-electron neutrinos for each interaction mode using 50years of MC. The horizontal axis is the reconstructed energy. The definition of the id number of interaction modes are described in Table-8.3.

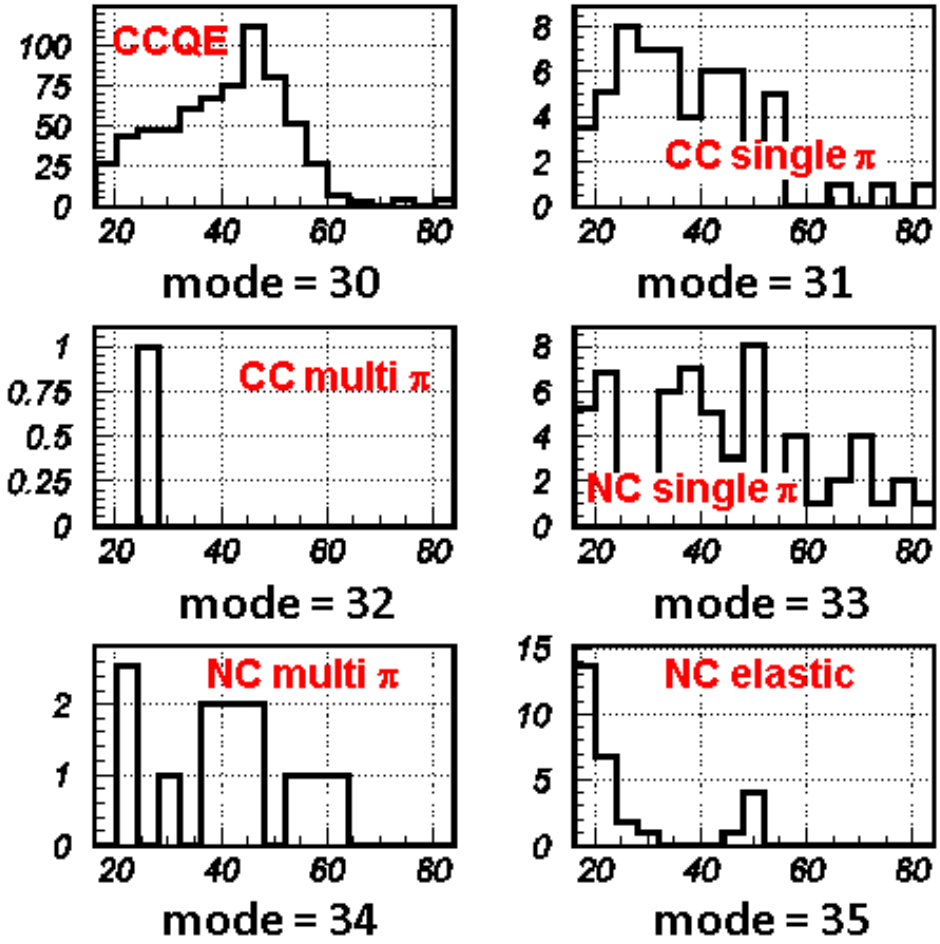

Figure 8.3: The energy spectrum of atmospheric muon neutrinos for each interaction mode using 50years of MC. The horizontal axis is the reconstructed energy. The definition of the id number of interaction modes are described in Table-8.4.

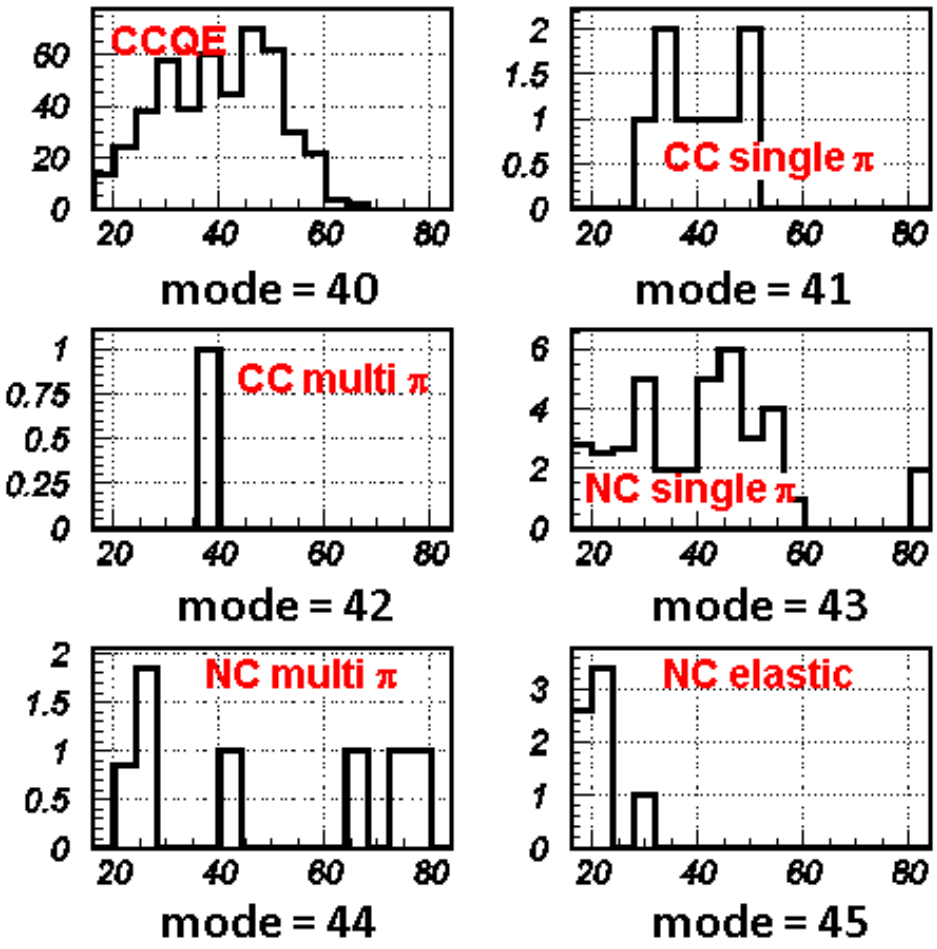

Figure 8.4: The energy spectrum of atmospheric anti-muon neutrinos for each interaction mode using 50years of MC. The horizontal axis is the reconstructed energy. The definition of the id number of interaction modes are described in Table-8.4.

id	muon neutrino interaction	id	anti-muon neutrino interaction
30	$\nu_\mu + n \to \mu^- + p$	40	$\bar{\nu_\mu} + p \to \mu^+ + n$
31	$\nu_\mu + p \to \mu^- + p + \pi^+$ $\nu_\mu + n \to \mu^- + p + \pi^0$ $\nu_\mu + n \to \mu^- + n + \pi^+$ $\nu_\mu +^{16} O \to \mu^- +^{16} O + \pi^+$	41	$\bar{\nu_\mu} + p \to \mu^+ + n + \pi^0$ $\bar{\nu_\mu} + p \to \mu^+ + p + \pi^-$ $\bar{\nu_\mu} + n \to \mu^+ + n + \pi^-$ $\bar{\nu_\mu} +^{16} O \to \mu^+ +^{16} O + \pi^-$
32	$\nu_\mu + p(n) \to \mu^- + p(n) + multi\ \pi$ $\nu_\mu + n \to \mu^- + p + \eta^0$ $\nu_\mu + n \to \mu^- + \Lambda + K^+$ $\nu_\mu + p(n) \to \mu^- + p(n) + mesons$	42	$\bar{\nu_\mu} + p(n) \to \mu^+ + p(n) + multi\ \pi$ $\bar{\nu_\mu} + p \to \mu^+ + n + \eta^0$ $\bar{\nu_\mu} + n \to \mu^+ + \Lambda + K^-$ $\bar{\nu_\mu} + p(n) \to \mu^+ + p(n) + mesons$
33	$\nu_\mu + n \to \nu_\mu + n + \pi^0$ $\nu_\mu + p \to \nu_\mu + p + \pi^0$ $\nu_\mu + n \to \nu_\mu + p + \pi^-$ $\nu_\mu + p \to \nu_\mu + n + \pi^+$ $\nu_\mu +^{16} O \to \nu_\mu +^{16} O + \pi^0$	43	$\bar{\nu_\mu} + n \to \bar{\nu_\mu} + n + \pi^0$ $\bar{\nu_\mu} + p \to \bar{\nu_\mu} + p + \pi^0$ $\bar{\nu_\mu} + n \to \bar{\nu_\mu} + p + \pi^-$ $\bar{\nu_\mu} + p \to \bar{\nu_\mu} + n + \pi^+$ $\bar{\nu_\mu} +^{16} O \to \bar{\nu_\mu} +^{16} O + \pi^0$
34	$\nu_\mu + n(p) \to \nu_\mu + n(p) + multi\ \pi$ $\nu_\mu + n \to \nu_\mu + n + \eta^0$ $\nu_\mu + p \to \nu_\mu + p + \eta^0$ $\nu_\mu + n \to \nu_\mu + \Lambda + K^0$ $\nu_\mu + p \to \nu_\mu + \Lambda + K^+$ $\nu_\mu + n(p) \to \nu_\mu + n(p) + mesons$	44	$\nu_\mu + n(p) \to \nu_\mu + n(p) + multi\ \pi$ $\bar{\nu_\mu} + n \to \bar{\nu_\mu} + n + \eta^0$ $\bar{\nu_\mu} + p \to \bar{\nu_\mu} + p + \eta^0$ $\bar{\nu_\mu} + n \to \bar{\nu_\mu} + \Lambda + K^0$ $\bar{\nu_\mu} + p \to \bar{\nu_\mu} + \Lambda + K^+$ $\bar{\nu_\mu} + n(p) \to \bar{\nu_\mu} + n(p) + mesons$
35	$\nu_\mu + p \to \nu_\mu + p$ $\nu_\mu + n \to \nu_\mu + n$	45	$\bar{\nu_\mu} + p \to \bar{\nu_\mu} + p$ $\bar{\nu_\mu} + n \to \bar{\nu_\mu} + n$

Table 8.4: The definition of id number in each interaction mode for muon and anti-muon neutrinos.

Charged current interactions (CC) create leptons that can be source of background. In the case of ν_μ and $\bar{\nu_\mu}$, decay electron from invisible muon is main background source. Pion is produced in the CC pion production interaction as well as lepton, but some fraction of pion cannot go out of oxygen nuclei due to a pion absorption. Neutral current interactions (NC) emit gamma rays and they can be a background in the SRN search (nuclear γ).

Additionally, deexcitation gamma rays from the interactions of final state nucleons in surrounding medium are another source of background(secondary-interaction γ). If charged particle is not produced at prompt interaction, those γ can be detected as prompt signal. Though CC interaction also can emit gamma rays, such event should have two timing peaks or sub-event (i.e. gamma ray and decay electron). So most CC events, including gamma rays originating from neutrino interaction, are already removed by the data reduction.

To evaluate the effects of atmospheric neutrino interactions other than decay electrons from invisible muons, we compared decay electron MC and atmospheric neutrino MC including all interaction in Figure-8.5.

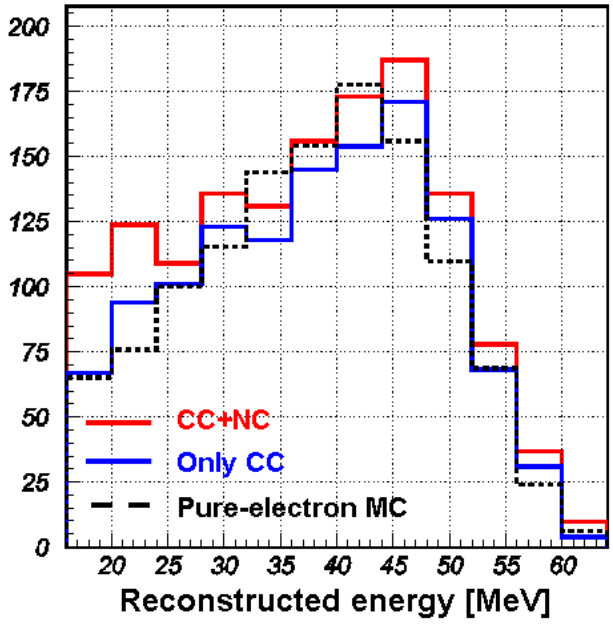

Figure 8.5: Energy spectra are compared between atmospheric neutrino MC and decay electron MC. The red histogram is the atmospheric neutrino MC including all interactions and the blue histogram includes only CC interaction events. Decay electron MC spectrum is normalized by number of entries in the blue histogram.

The decay electron MC (black) is generated as an electron (positron) whose energy follows the Michel spectrum. The red histogram is atmospheric neutrino

MC including all interactions and the blue includes only CC interactions. The difference between red and blue is due to gamma rays mainly caused by nuclear γ. The small difference between blue and black comes from secondary γ although most CC secondary γ events are rejected by data reduction. The decay electron MC spectrum is normalized by the number of entries in the blue histogram. The systematic error of background shape is estimated from the difference between all interaction modes of atmospheric MC (red) and decay electron MC (black). This difference is assumed to be 1σ level systematic uncertainty.

Chapter 9

Results

After all reductions, the final data sample was obtained, and still remaining backgrounds were understood as atmospheric neutrino origin as stated in the previous chapter. Because the individual SRN events cannot be identified, a statistical method was used to extract the SRN signal. In this chapter, a fitting method using the energy spectra and its results are described.

9.1 Spectrum fitting

Although nine SRN models predict slightly different spectral shape, those shapes all basically decrease exponentially with increasing energy, as shown in Figure-6.4. In contrast, the spectral shape of the expected background, i.e. invisible μ-e decay, atmospheric ν_e, $\bar{\nu_e}$, rise with energy increase. See Figure-7.5 and 7.6. Since their spectra are different from the SRN spectrum, spectrum fitting can be used to discriminate those components.

9.1.1 The spectrum fitting by Gaussian method

The expected signal and background spectra obtained in the previous chapter were normalized by the livetime and used to fit the final data spectrum. The energy spectra of our final data samples for SK-I and SK-II are shown in Figure-7.1. The lower threshold of this analysis is 16 MeV (SK-I, SK-III) and 18 MeV (SK-II), which is limited by the spallation backgrounds. Although the decay electron spectrum is up to $\sim$65 MeV, even considering detector resolution, the upper threshold of this analysis was extended to 80 MeV, in order to evaluate the contribution from the atmospheric ν_e, $\bar{\nu_e}$.

For the fitting, the data was divided into sixteen bins, with 4 MeV width, and the following χ^2 function was used.

$$\chi^2 = \sum_{i=1}^{16} \frac{(N_{Data}(i) - N_{Spec}(i))}{\sigma^2} \tag{9.1}$$

$$N_{Spec}(i) = \alpha \times N_{SRN}(i) + \beta \times N_{atm\nu_e}(i) + \gamma \times N_{atm\nu_\mu}(i) + N_{Spal}(i) \tag{9.2}$$

Where:

- N_{Data} : The spectrum of the final data sample
- N_{SRN} : The spectrum of the SRN MC
- $N_{atm\nu_e}$: The spectrum of the atmospheric ν_e, $\bar{\nu_e}$ MC
- $N_{atm\nu_\mu}$: The spectrum of the decay electron from stopping muon real data
- N_{spal} : The expected number of remaining spallation events (only for SK-II)

α, β and γ are the normalizing factors for SRN, atmospheric ν_e, $\bar{\nu_e}$ and invisible μ-e decay respectively.

σ is the statistical error of the Gaussian standard deviation and systematic error, added quadrature, represented as follows.

$$\sigma^2 = \sigma^2_{data} + \sigma^2_{MC} + \sigma^2_{sys} \tag{9.3}$$

Since the MC statistics are much larger than the data statistics, σ^2_{MC} is negligible in all energy regions. The systematic error, described in section 7.3, is always <5% and is also much smaller than the data statistical error. Minimizing the χ^2 function(Equation-9.1), the α, β and γ parameters were determined. To avoid the best fit SRN flux being in the unphysical region, the α parameter was required to be non-negative.

By the spectrum fitting method described above, we obtained the α parameter, which indicates the expected number of SRN events in our data sample. We obtained the best α value and its 1 σ error, which were 0.2 ± 0.9 in SK-I, $< 1.5(1\sigma)$ in SK-II and 0.8 ± 1.8 in SK-III[1]. All of them are consistent with zero, within a 1σ error. This means there is no clear evidence of SRN events in SK-I, SK-II and SK-III. The minimum χ^2 value is 11.9, for 13 degree of freedom, in SK-I which corresponds to 54% probability. For SK-II and SK-III, the χ^2 values are 10.6 and 8.8, both for 13 degree of freedom, and correspond to 64% and 79% probabilities. These χ^2 values demonstrate the validity of our background hypothesis.

As we discuss later, the Gaussian method was used in the old SK-I analysis [16], which gave the current flux upper limit of < 1.2 /cm^2/sec(>18 MeV).

9.1.2 Spectrum fitting by Poissonian method

In the previous section, the fitting method by the Gaussian method was described. But even in the SK-I data, which has the largest statistics in the three phases, the number of entries in each bin is not large enough to approximate the statistical errors by a Gaussian standard deviation. In the case of SK-II

[1]since the best fit α is in the unphysical region in SK-II, only the upper 1σ side is shown

and SK-III, statistics are even poorer than SK-I. So we developed a new flux extraction method, based on the Poissonian distribution.

The χ^2 is defined in equation 9.6, and can be transformed as follows.

$$\chi^2 = \Sigma \frac{(N_{obs} - N_{spec})^2}{\sigma^2} = -2\Sigma \log \frac{G(N_{obs}, N_{spec})}{G(N_{obs}, N_{obs})} \tag{9.4}$$
$$G(N_{obs}, N_{spec}) = \frac{exp(-(N_{obs} - N_{spec})^2/2\sigma^2)}{\sqrt{2\pi}\sigma}$$

$$N_{Spec}(i) = \alpha \times N_{SRN}(i) + \beta \times N_{atm\nu_e}(i) + \gamma \times N_{atm\nu_\mu}(i) + N_{Spal}(i) \tag{9.5}$$

Where $G(N_{obs}, N_{spec})$ is a Gaussian distribution and N_{spec} is signal + BG spectrum expected from α, β and γ. Then by replacing the Gaussian distribution by a Poisson distribution, we obtained the χ^2 of the Poissonian method:

$$\begin{aligned} \chi^2 &= -2 \log \frac{P(N_{obs}, N_{spec})}{P(N_{obs}, N_{obs})} \\ &= -2\Sigma \log \left(\frac{N_{spec}}{N_{obs}} \right)^{N_{obs}} exp\left(N_{obs} - N_{spec}\right) \\ &= -2\Sigma \log \left(N_{obs} - N_{spec} + N_{obs} \log \left(\frac{N_{spec}}{N_{obs}} \right) \right) \end{aligned} \tag{9.6}$$

where

$$P(N_{obs}, N_{spec}) = \frac{(N_{spec})^{N_{obs}} exp(-N_{spec})}{N_{obs}!} \tag{9.7}$$

In the Poissonian fitting method, this χ^2 was used instead of the Gaussian χ^2, defined by Equation-9.1. Since this χ^2 definition does not include σ, systematic errors were considered as follows.

$$\chi^2 = \int \chi^2(\eta, \xi, \delta) \frac{exp(-\eta^2/2\sigma_\eta^2)}{\sqrt{2\pi}\sigma_\eta} \frac{exp(-\xi^2/2\sigma_\xi^2)}{\sqrt{2\pi}\sigma_\xi} \frac{exp(-\delta^2/2)}{\sqrt{2\pi}} d\eta d\xi d\delta \tag{9.8}$$

where η is the energy scale error and its uncertainty (σ_η) was obtained from the LINAC and DTG calibration (section 3.7). ξ is the systematic error of the expected number of SRN events(e.g. due to reduction efficiency, fiducial volume, livetime etc). The estimated error was summarized in Table-8.1. By changing η and ξ manually, SRN spectrum is regenerated (see Equation-9.9) and χ^2 is calculated for each η and ξ. η and ξ is changed from -3σ to +3σ and χ^2 is summed up with the weight of Gaussian distribution.

$$(1 + \xi) \times N_{SRN}(E \times (1 + \eta)) \tag{9.9}$$

δ is the background shape uncertainty for decay electron spectrum. Real background shape include not only decay electron but also some gamma rays

originating from atmospheric neutrino interaction. This error changes the decay electron spectrum as follows:

$$N_{atm\nu_\mu}(i) + \delta \times \Delta N_{atm\nu_\mu}(i) \tag{9.10}$$

We estimated this error ($\Delta N_{atm\nu_\mu}(i)$) using atmospheric MC as described in section 8.3.

δ is changed only for positive side from 0 to $+3\sigma$, because additional nuclear and secondary γ rays distort the spectrum only to positive direction.

Fitting result

The fitting was performed using the Poissonian χ^2, defined by Equation-9.6, for all of the SRN models and the best fit parameters were obtained by minimizing the χ^2 value.

The Poissonian distribution is asymmetric and the error bar is larger for the upper direction. So the best fit parameters are likely to be larger values than those for the Gaussian case. Between the 30 and 60 MeV region, where the decay electron background is dominant, the number of entries is more than ten, so the error bar can be approximated by the Gaussian distribution. So the γ parameter, which is the normalizing factor of the decay electron spectrum, does not changed. Since the signal energy region, below 30 MeV, also has small statistics, this increases the limit of α. Thus the limit on the number of events, and the flux, should be worse in the Poissonian method.

The best fit parameters are listed in Table-9.1. The best fit spectra are shown in Figure-9.1(SK-I), 9.2(SK-II) and 9.3(SK-III), respectively. The data points with error bars represent the data spectrum, the red line is the spectrum of atmospheric ν_e, $\bar{\nu_e}$ MC, the green line is the spectrum of decay electrons from stopping muon real data. The black line shows the sum of the red and green spectra.

parameter	best fit value SK-I	best fit value SK-II	best fit value SK-III
α	0.12 $\pm$ 0.8	0.0	0.66 $\pm$1.8
β	1.26	0.94	1.51
γ	1.39	0.47	1.16
χ^2	14.1 / 13 d.o.f	8.5 / 13 d.o.f	9.1 / 13 d.o.f

Table 9.1: The best fit parameters from the χ^2 spectrum fitting in SK-I, SK-II and SK-III, by the Poissonian method, are listed. The LMA model was used for getting this result. α, β and γ are the normalizing factors for SRN, atmospheric ν_e, $\bar{\nu_e}$ and invisible μ-e decay, respectively.

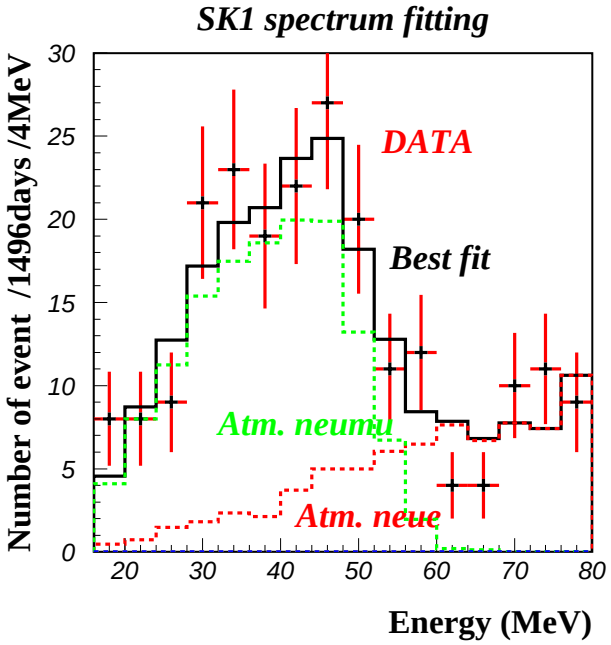

Figure 9.1: The result of the χ^2 fitting for the distribution of the SK-I final data sample, by Poissonian method, are shown. The LMA model was used for getting this result. The data points are SK-I data and the red and green dashed histograms represent the fitted backgrounds from atmospheric ν_e (and $\bar{\nu_e}$) and invisible μ-e decay. The black solid line shows the sum of both backgrounds.

9.2 flux upper limit extraction

In the previous section, we discussed the spectrum fitting results. From these results we could not find a significant SRN signal in any of the three data taking phases, so we extracted the flux upper limit from the fitting result, as described below.

1. Get the χ^2 distribution as a function of α, by changing α, with minimizing χ^2 with two free parameters(β and γ). The χ^2 values thus obtained at each α are defined as χ^2_α. the χ^2_α distribution in SK-I for the LMA model is shown in Figure-9.4(top).

2. The probability is calculated for each χ^2_α, defined by Equation-9.11. Figure-9.4(middle) shows the probability distribution as a function of χ^2_α.

$$Probability = K \cdot \exp\left(-\frac{\chi^2_\alpha}{2}\right) \tag{9.11}$$

Where K is the normalizing factor, determined to make the integrated value equal to 1 as follows.

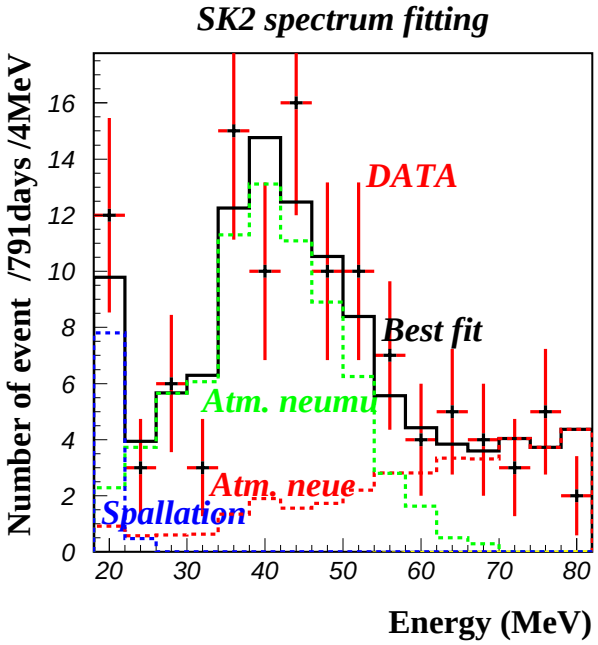

Figure 9.2: The result of the χ^2 fitting for the distribution of the SK-II final data sample, by Poissonian, method are shown. The LMA model was used for getting this result. The data points are SK-II data and the red and green dashed histograms represent the fitted backgrounds from atmospheric ν_e (and $\bar{\nu_e}$) and invisible μ-e decay. The black solid line shows the sum of both backgrounds.

$$\int_{\alpha=0}^{\infty} K \cdot \exp\left(-\frac{\chi^2_\alpha}{2}\right) d\alpha = 1 \tag{9.12}$$

3. The probability is integrated up to $\alpha = 40$. The α value whose sum of the probability exceeds 0.9 corresponds to the 90% confidence level α upper limit and is defined as α_{90}. The sum of the probability as a function of α is shown in Figure-9.4(bottom) and the dotted line shows the 90% confidence level limit.

4. Multiplying the expected number of events shown in Table-6.1 by the obtained α_{90}, the 90% confidence level limit of the SRN events(N_{limit}) is obtained. Similarly, multiplying the expected flux value by α_{90} gives us the 90% confidence level flux upper limit(F_{limit}).

$$N_{limit}(> 16MeV) = N(16 - \infty MeV) \times \alpha_{90} \tag{9.13}$$

$$F_{limit}(> 16MeV) = F(16 - \infty MeV) \times \alpha_{90} \tag{9.14}$$

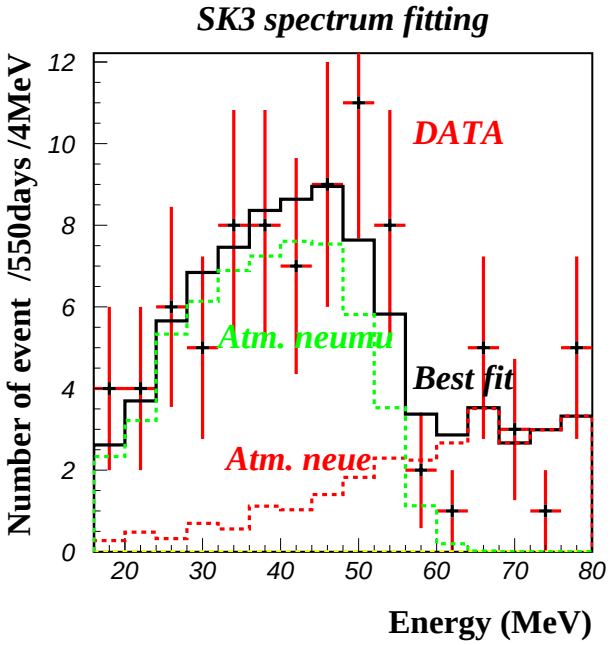

Figure 9.3: The result of the χ^2 fitting for the distribution of the SK-III final data sample, by Poissonian method, are shown. The LMA model was used for getting this result. The data points are SK-III real data and the red and green dashed histograms represent the fitted backgrounds from atmospheric ν_e (and $\bar{\nu_e}$) and invisible μ-e decay. The black solid line shows the sum of both backgrounds.

However, N(F) is the predicted number of events(flux) for each model and is integrated for the region in parenthesis. Table-9.2 shows the number of events and the flux upper limits at the 90% confidence level for nine SRN theoretical models, for the analysis energy region (16MeV electron energy corresdonds to 17.3MeV neutrino energy). The flux upper limits were obtained for SK-I, SK-II and SK-III and for each SRN model. For LMA model, 90% confidence level flux upper limits were $< 2.6/\mathrm{cm}^2/\mathrm{sec}$ (SK-I), $< 5.0/\mathrm{cm}^2/\mathrm{sec}$ (SK-II) and $< 5.9/\mathrm{cm}^2/\mathrm{sec}$ (SK-III), respectively. The flux upper limits are summarized in Table-9.3.

Combined flux upper limit

The flux upper limit was obtained for SK-I, SK-II and SK-III individually. In this section, a combined analysis using these three phase results is described. The χ^2 distributions for all three phases are summed up to obtain the combined χ^2 ($=\chi^2_{comb}$) distribution as follows.

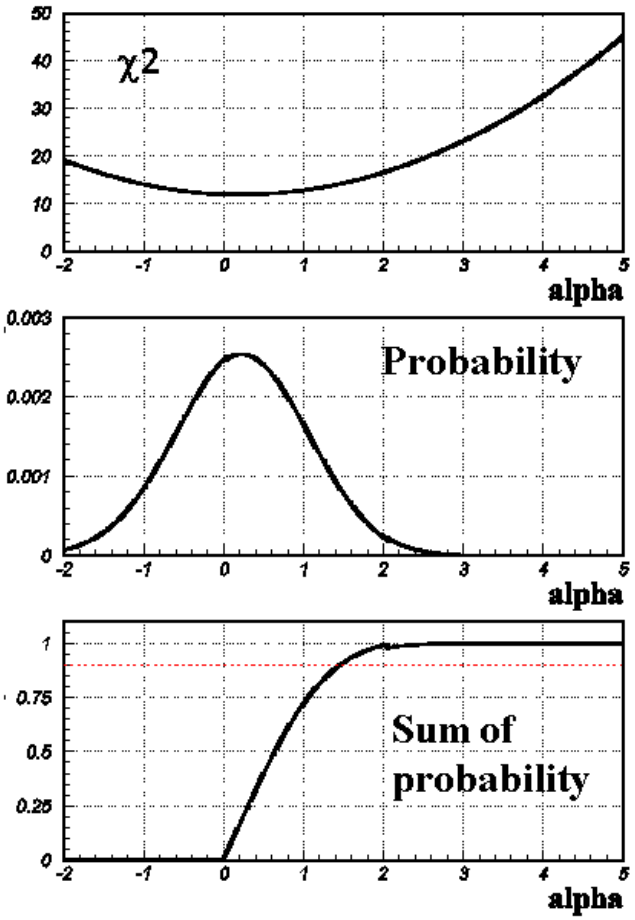

Figure 9.4: The chi-squared, probability and sum of the probability distributions are plotted as a function of alpha. The red dotted line shows the 90% confidence lebel.

$$\chi^2_{comb} = \chi^2_{SK-I} + \chi^2_{SK-II} + \chi^2_{SK-III} \tag{9.15}$$

The χ^2_{comb}(and χ^2 in each phase) distribution, as a function of α is shown in Figure-9.5. α_{90} was obtained from the χ^2_{comb} distribution and is converted to the 90% confidence level flux upper limit. The 90% flux upper limits, corresponding to E_ν >17.3 MeV, obtained by this combined method are listed in Table-9.4.

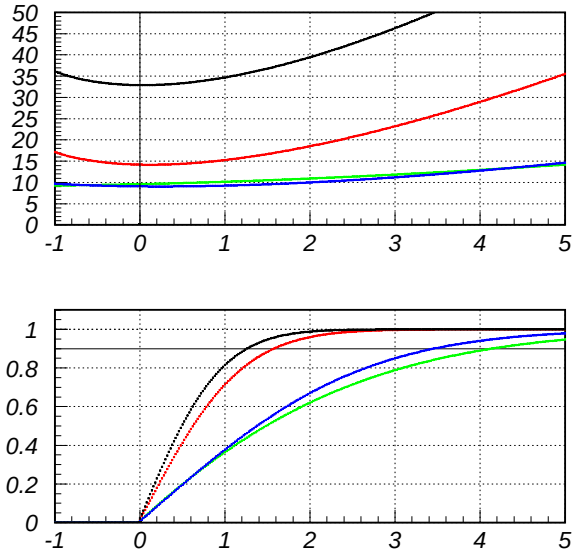

Figure 9.5: The chi-squared(top) and sum of the probability(bottom) distributions, for the LMA model, are plotted as a function of alpha. Red is SK-I, green is SK-II, and blue is SK-III respectively. The black line shows the combined χ^2 distribution.

Theoretical model	SK-I (16-80 MeV)	SK-II (18-82 MeV)	SK-III (16-80 MeV)
LMA neutrino oscillation	< 15.6	< 14.2	< 12.1
Constant SN rate	< 15.2	< 13.3	< 12.0
Cosmic gas infall	< 13.0	< 11.2	< 10.1
Cosmic Chemical evolution	< 14.4	< 12.8	< 11.3
Heavy metal abundance	< 13.4	< 12.8	< 10.8
Population synthesis	< 14.7	< 13.1	< 11.6
Cosmic SF history	< 16.1	< 14.2	< 12.7
SFR constraint	< 17.4	< 14.0	< 12.3
Failed supernova	< 12.7	< 11.1	< 10.0

Table 9.2: The limit on the number of events for each model, by Poissonian method, are listed for all three data taking phase. The fiducial volume was 22.5 kton for all three phases. The livetimes are 1496 days in SK-I, 791 days in SK-II and 548 days in SK-III.

Theoretical model	SK-I $E_\nu >$17.3MeV	SK-II $E_\nu >$ 19.3MeV	SK-III $E_\nu >$ 17.3MeV
LMA neutrino oscillation	< 2.6	< 5.0	< 5.9
Constant SN rate	< 2.7	< 4.9	< 5.9
Cosmic gas infall	< 2.5	< 4.2	< 5.5
Cosmic Chemical evolution	< 2.6	< 4.8	< 5.9
Heavy metal abundance	< 2.5	< 4.8	< 5.7
Population synthesis	< 2.6	< 4.8	< 5.9
Cosmic SF history	< 2.7	< 4.9	< 6.0
SFR constraint	< 2.6	< 4.9	< 5.9
Failed supernova	< 2.8	< 5.3	< 6.1

Table 9.3: The upper limit on the anti-electron neutrino flux for each model, by Poissonian method, are listed. All three data taking phases are listed. The flux units are [/cm^2/sec].

Theoretical model	Flux limit (E_ν >17.3 MeV)
LMA neutrino oscillation	$< 2.1\ \bar{\nu_e}\ /cm^2\ /sec$
Constant SN rate	$< 2.1\ \bar{\nu_e}$/cm^2/sec
Cosmic gas infall	$< 2.0\ \bar{\nu_e}\ /cm^2\ /sec$
Heavy metal abundance	$< 2.0\ \bar{\nu_e}\ /cm^2\ /sec$
Cosmic Chemical evolution	$< 2.1\ \bar{\nu_e}\ /cm^2\ /sec$
Population synthesis	$< 2.1\ \bar{\nu_e}\ /cm^2\ /sec$
Cosmic SF history	$< 2.1\ \bar{\nu_e}\ /cm^2\ /sec$
SFR constraint	$< 2.1\ \bar{\nu_e}\ /cm^2\ /sec$
Failed supernova	$< 2.2\ \bar{\nu_e}\ /cm^2\ /sec$

Table 9.4: The combined 90% C.L. upper limit on the SRN flux, for each model, by poissonian method. The second column is the flux limit for E_ν >17.3MeV.

Chapter 10

Discussion

The SRN flux upper limit of < 2.0 - 2.2 /cm^2/sec ($E_\nu > 17.3 MeV$) was obtained in the previous chapter. This obtained upper limit is compared with the SRN theoretical models and other experimental results in this chapter.

10.1 Comparison with theoretical models

In this thesis, nine theoretical models were used to evaluate the SRN spectrum shape. The flux upper limit was obtained for each model, all within the range of $\sim$ 2.0 - 2.2 /cm^2/sec. They are compared with the predicted flux from each model and are discussed in this section.

The "LMA oscillation model" includes neutrino oscillation effects inside stars and was calculated by Ando et al[26, 27]. Due to the oscillation effects, the $\bar{\nu_e}$ spectrum becomes relatively harder and the predicted flux is higher among the models we used in this analysis. The predicted flux for the neutrino region with energy above 17.3 MeV(corresponding to 16 MeV of electron energy) is $\sim$ 1.7 /cm^2/sec. The 90% flux upper limit obtained from the combined analysis was < 2.1 /cm^2/sec($E_\nu > 17.3$ MeV). Our flux limit is higher than the prediction by $\sim$ 20%. Figure-10.2(top) shows the predicted flux and the obtained flux limit for this model. The black line shows the SRN spectrum. The upper region of the red line is excluded by our 90% confidence level flux limit. Since we used the spectrum fitting method, the flux limit curve is parallel with the model spectrum. The main search region in our analysis is effectively up to $\sim$ 30 MeV. This is because the invisible muon background dominates above 30 MeV, although spectrum fitting has been done up to 80 MeV.

The "Constant SN rate model" [21] predicts the largest flux by assuming a constant rate of core collapse supernovae, since the beginning of the universe till now. The predicted flux in this model is $\sim$ 4.6 /cm^2/sec for neutrino energy above 19.3 MeV. The obtained flux limit was 2.1 /cm^2/sec and is already strict enough to exclude this model prediction. Figure-10.2(middle) is the comparison between the model prediction and our limit. The "Constant SN rate model" was

excluded in our analysis, in the energy region of $E_\nu > 17.3$MeV(corresponding to 16 MeV electron energy).

The "Cosmic gas infall model" [22] is predicts the smallest neutrino flux among the nine models used in this analysis. The spectrum shape of this model most sharply decreases with increasing energy. The spectrum shape is most different from the other background spectrum, so the lowest flux upper limit($<$ 2.0 /cm^2/sec for above 17.3 MeV) was obtained. However, this upper limit is still larger than the predicted flux(0.3 /cm^2/sec) by almost one order of magnitude. The predicted spectrum and our limit is plotted in Figure-10.3(bottom).

According to the calculation of the "Cosmic chemical evolution model" [23], the flux should be about 0.6 /cm^2/sec. Our limit of $<$ 2.1 /cm^2/sec is still higher than the predicted flux by more than a factor of three. A comparison between our limit and the predicted spectrum is shown in Figure-10.3.

The predicted flux of the "Heavy metal abundance model" [24] is between 0.4 and 1.8 /cm^2/sec. Comparing with our flux limit($<$ 2.0 /cm^2/sec), the prediction is $\sim$ 10% smaller in the maximum case of flux prediction. This indicates our sensitivity is now close to the SRN detectable region for this model. Figure-10.3(top) shows the predicted flux both in the maximum and the minimum case, as well as our flux limit.

The "Population synthesis model" [21] predicts a large flux when integrated over all energy regions. However, the predicted flux above 17.3 MeV is the second smallest in all the models. This is because this model uses a supernova rate which drops sharply as a function of the red shift parameter, and the neutrino energy is strongly redshifted below our energy threshold before reaching the earth. The predicted flux is 0.5 /cm^2/sec, and the limit from this analysis is 2.1 /cm^2/sec. Our limit is larger than that prediction by a factor of $\sim$ 4. To dramatically increase the sensitivity for this model, we need to lower the analysis energy threshold down to at least $\sim$ 10 MeV.

The "Cosmic SF history model" [28] predicts the second highest SRN flux for above 17.3 MeV neutrino energy. This model predicts the SRN spectrum using three different effective temperature of neutrinos(4, 6 and 8 MeV). In the case of 6 MeV, which was used in our analysis, the predicted neutrino flux is 1.1 - 1.9 /cm^2/sec, above 17.3 MeV. This is not so far from our flux limit of $<$ 2.1 /cm^2/sec. As shown in Figure-10.4(top), the case of 8 MeV effective temperature is excluded by our 90% confidence level flux upper limit.

The "SFR constraint model" [29] gives a flux prediction of 0.7 /cm^2/sec, above 17.3 MeV. This is the average of the maximum case and the minimum case. Both cases are plotted in Figure-10.4(middle). Our limit of $<$ 2.1 /cm^2/sec is almost a factor of two larger than the maximum case of $\sim$ 1.1 /cm^2/sec. Comparing with the minimum case of $\sim$0.4 /cm^2/sec, the difference from our limit is a factor five.

The predicted flux from the calculation of the "Failed SN model" [30] predicts a hard spectrum due to higher energy neutrino emission from failed supernova explosions. This flux is between 0.9 and 1.2 /cm^2/sec ($>$ 17.3 MeV), depending on a fraction of failed supernovae(9-22%) and other parameters. The spectra

in the maximum and minimum cases are shown in Figure-10.4(bottom). In the case of the largest fraction of failed supernovae, the spectrum becomes hardest and then the predicted flux above our energy threshold becomes higher. Since we used the case of maximum failed supernovae fraction, the spectrum shape is hard, so that our flux limit for this model(< 2.2 /cm^2/sec) is larger than the other models. Comparing with the limit, the model prediction is smaller than our limit by a factor of ~ 2.

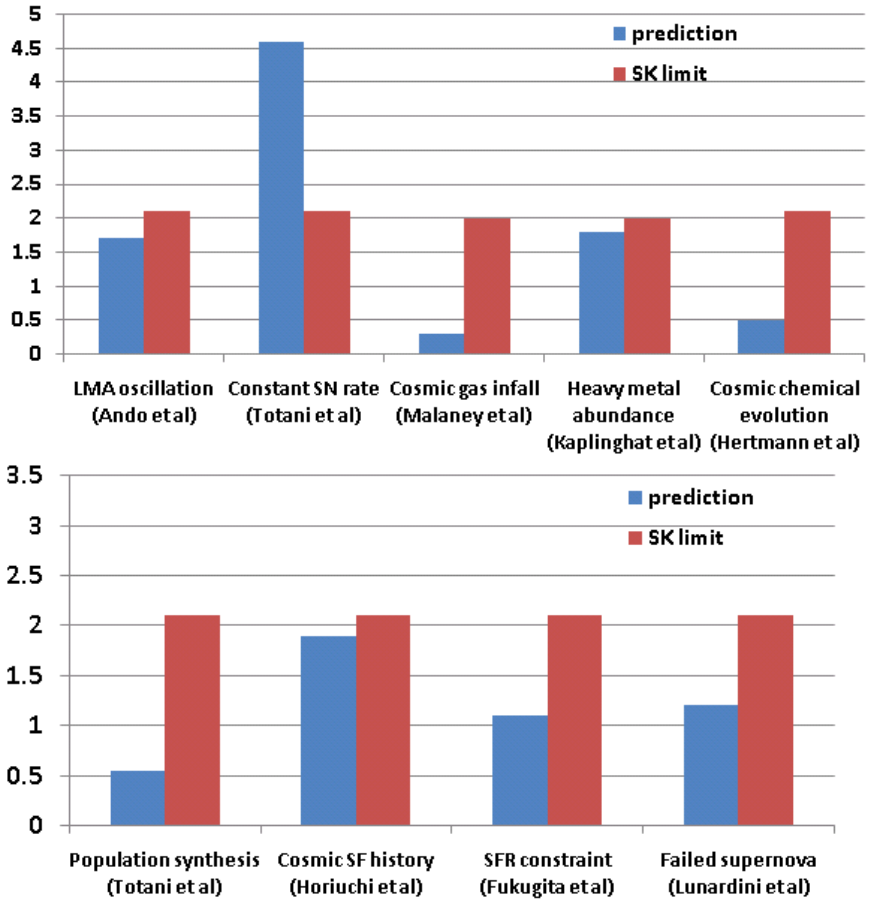

Figure 10.1: The flux upper limit and the predicted flux for each model above 19.3 MeV are shown. The uncertainty of the model prediction is represented by yellow arrows.

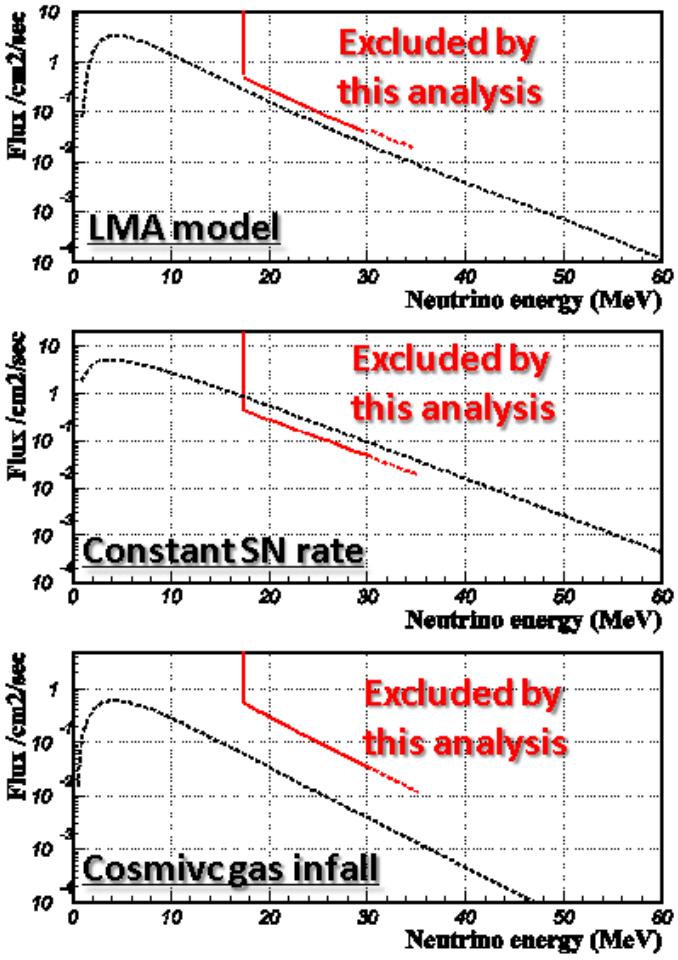

Figure 10.2: The flux limit vs the predicted SRN spectra are shown in this figure. The red line shows our 90% flux limit, obtained in the previous chapter. Since we used the spectrum shape of each model, the obtained flux limit has the same shape as each model. The black dashed line is the predicted SRN flux.

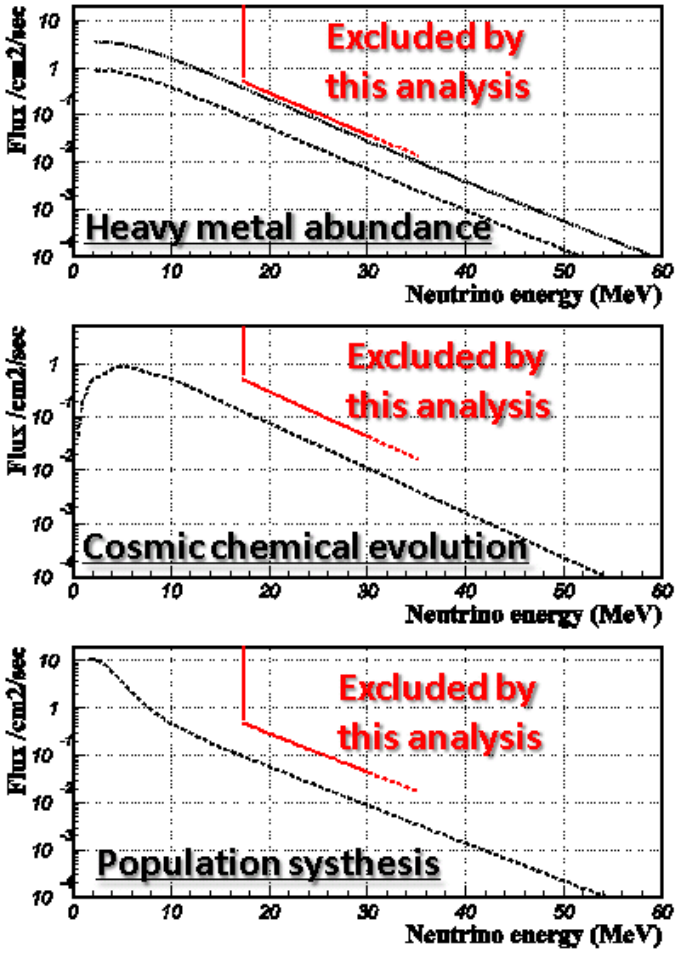

Figure 10.3: The flux limit vs the predicted SRN spectra are shown in this figure. The red line shows our 90% flux limit, obtained in the previous chapter. In the top figure, the dashed line is the minimum case of the prediction and the dotted line is the maximum case.

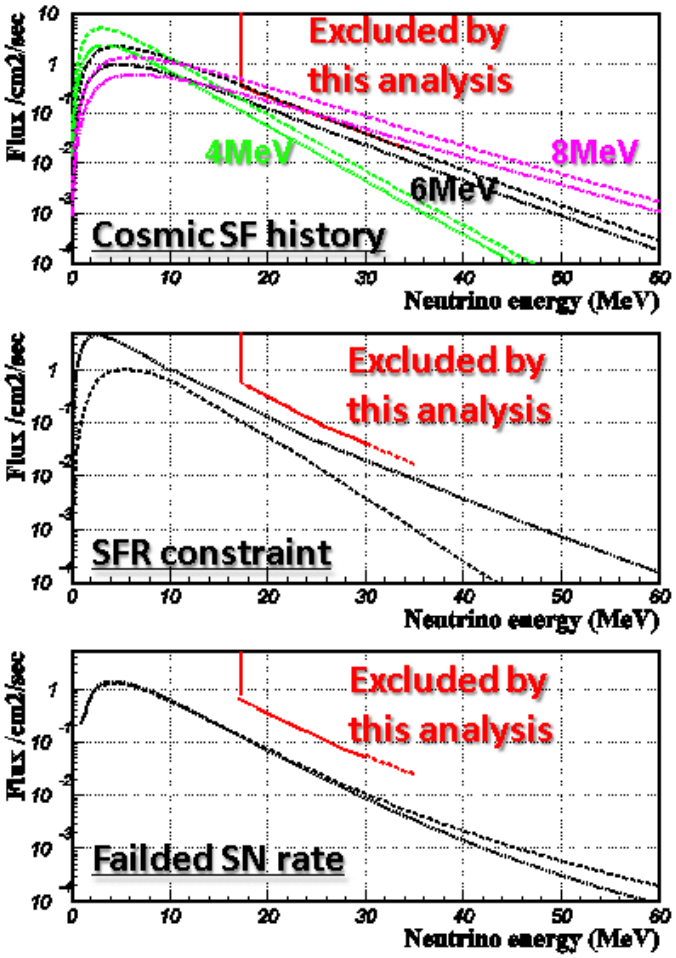

Figure 10.4: The flux limit vs the predicted SRN spectra are shown in this figure. The red line shows our 90% flux limit, obtained in the previous chapter. In the middle and bottom figures, the dashed line is the minimum case of the prediction and the dotted line is the maximum case. In the top figure, the different colors show the prediction with different effective temperatures.

Theoretical model	Predicted flux (E_ν >17.3MeV)	Flux limit (E_ν >17.3MeV)
LMA neutrino oscillation	1.7 $\bar{\nu_e}$ /cm^2/sec	< 2.1 $\bar{\nu_e}$ $/cm^2/sec$
Constant SN rate	4.6 $\bar{\nu_e}$/cm^2/sec	< 2.1 $\bar{\nu_e}$ $/cm^2/sec$
Cosmic gas infall	0.3 $\bar{\nu_e}$ $/cm^2/sec$	< 2.0 $\bar{\nu_e}$ $/cm^2/sec$
Heavy metal abundance	0.4-1.8 $\bar{\nu_e}$ $/cm^2/sec$	< 2.0 $\bar{\nu_e}$ $/cm^2/sec$
Cosmic Chemical evolution	0.5 $\bar{\nu_e}$ $/cm^2/sec$	< 2.1 $\bar{\nu_e}$ $/cm^2/sec$
Population synthesis	0.4 $\bar{\nu_e}$ $/cm^2/sec$	< 2.1 $\bar{\nu_e}$ $/cm^2/sec$
Cosmic SF history	1.1-1.9 $\bar{\nu_e}$ $/cm^2/sec$	< 2.1 $\bar{\nu_e}$ $/cm^2/sec$
SFR constraint	0.4-1.1 $\bar{\nu_e}$ $/cm^2/sec$	< 2.1 $\bar{\nu_e}$ $/cm^2/sec$
Failed supernova	0.9-1.2 $\bar{\nu_e}$ $/cm^2/sec$	< 2.2 $\bar{\nu_e}$ $/cm^2/sec$

Table 10.1: The combined 90% C.L. upper limit on the SRN flux for each model, by Poissonian method. The second column is the flux limit for the energy region above 16 MeV and the third column is for that above 18 MeV.

10.2 Comparison with other experiments

Our experimental result was compared with other experiments, e.g. Kamiokande, SNO, KamLAND etc, in this section. The 90% confidence level flux upper limits in this thesis were $<$ 2.0 - 2.2 /cm^2/sec, depending on the spectrum shape of the used SRN model. Using the LMA model, the flux limit was $<$ 2.1 /cm^2/sec, which is better than other experimental result by an order of magnitude. Figure-10.5 shows our flux limit(red line) and other experimental result in the unit of neutrino flux(/cm^2/sec/MeV), as a function of neutrino energy.

The green line shows the "KamLAND" result of $\lesssim 10^2$/cm^2/sec/, in the energy range of 8 - 14 MeV. Although the search region is different from our analysis, their limit is larger than the prediction from the LMA model by an order of magnitude or more.

The "Mont Blanc" result is shown as a light blue line. This limit is given for the same energy region as our analysis, however, our limit is better than their result by more than three orders of magnitude.

The "SNO" experiment searched for electron neutrinos in the energy region of 22.9 - 36.9 MeV. Their result showed the electron neutrino flux, for 22.9 - 36.9 MeV, is smaller than 70 /cm^2/sec. The flux of electron neutrinos, emitted from core collapse supernovae, is smaller than that of anti-electron neutrinos, above the 20 MeV region as shown in Figure-1.5. So our flux limit is much closer to the predicted SRN flux than the SNO result.

Previously, the "Kamiokande" result was the most strict limit, which was obtained using the "Constant SN rate model". The result from Kamiokande is shown as a pink line, which has a slope that is the same as the "Constant SN rate model" spectrum. Even when comparing with this result, our flux limit is better by at least an order of magnitude.

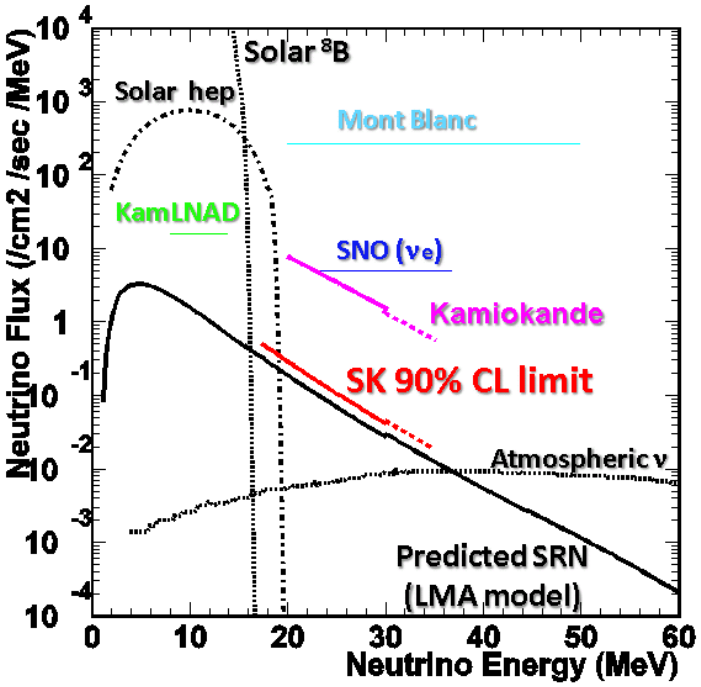

Figure 10.5: The flux upper limit of our result and other experimental results are plotted. The horizontal axis is neutrino energy and the vertical axis is neutrino flux in units of $/\mathrm{cm}^2/\mathrm{sec}/MeV$. For the SRN spectrum, the LMA model was used.

Experiment	Channel	Energy window	Flux upper limit
KamLAND	$\bar{\nu_e}$	8 - 14	$\sim 10^2$
Mont Blanc	$\bar{\nu_e}$	20 - 50	8.2×10^3
SNO	ν_e	22.9 - 36.9	70
Kamiokande	$\bar{\nu_e}$	> 19	50
Super-Kamiokande	$\bar{\nu_e}$	> 17.3	2.0 - 2.2

Table 10.2: The flux upper limit for each experiment. The third column is the search window of neutrino energy. The units of the flux upper limit are $/cm^2/sec$.

As we discussed in this chapter, the flux upper limits obtained in this analysis($<$ 2.0 - 2.2 /cm^2/sec) are already close to the model predicting SRN flux(0.3 - 4.6 /cm^2/sec). The difference between our limit and the prediction is less than one order of magnitude, even in the model which predict the smallest SRN flux. Furthermore, some of the optimistic cases of SRN predictions were excluded by this result. Comparing with other experimental results, our result is much better by orders of magnitude.

Chapter 11

Conclusion

The diffuse supernova neutrino background from all the past supernova, known to be Supernova relic neutrino (SRN), were searched for in Super-Kamiokande, which is a large water Cherenkov detector located at 1000m underground in the Kamioka mine. Three data taking phases were used in this analysis and each phase has a livetime of 1496 days (SK-I), 791 days (SK-II) and 548 days (SK-III). This is the first search for supernova relic neutrinos using SK-II and SK-III data.

From the old SK-I analysis, we developed a new statistical method based on the Poisson distribution which is more suitable for small statistics. We improved the reduction method from SK-I old analysis in order to increase the efficiency and to lower the energy threshold. This enabled us to lower the analysis energy threshold down to 16 MeV from 18 MeV with better signal efficiency.

No evidence for supernova relic neutrino signals were found in this search. The 90% confidence level upper limit on the SRN flux was obtained by the Poissonian method and improved reduction method. The flux upper limits on SRN $\bar{\nu_e}$ were obtained for nine theoretical models which predict the spectrum and absolute flux of supernova relic neutrinos. The obtained flux limits by combined analysis of SK-I, SK-II and SK-III range from 2.0 /cm^2/sec to 2.2 /cm^2/sec ($E_\nu > 17.3$ MeV) depending on the spectrum shape of the SRN model considered. Our results are now close to the predicted SRN flux ranging from 0.4 - 4.6 /cm^2/sec ($E_\nu > 17.3$ MeV).

The new result presented in this thesis supersedes the previous Super-Kamiokande limit [16] based on the improved analysis method and the increased statistics. The updated limit is an order of magnitude better than the values obtained by other experiments. Some of the optimistic predictions for the SRN are excluded by this result.

Appendix A

Comparison with previous result in SK

In this appendix, we compare the results with the previous SK-I result of < 1.2 /cm^2/sec (>18 MeV). This previous result was obtained using almost the same reduction process as for our SK-II analysis, except for the sub-event cut. In addition, the inverse beta decay cross section used in the previous analysis was overestimated, especially in the higher energy region(see section 1.2.2). This changed the result by $\sim$ 20% overall. After applying the sub-event cut and using the most recent cross section calculation, the flux upper limit becomes < 1.4/cm^2/sec using the Gaussian method and < 1.7 /cm^2/sec using the Poissonian method, both using the LMA model[27]. Since the data statistics is not high enough, the Poissonian method should be used to extract the flux upper limit, even in SK-I. So the result of < 1.7 /cm^2/sec should be compared with our new result.

Considering only the SK-I result of the new analysis, the flux upper limit is 1.9 /cm2/sec, for the LMA model. The new result is worse, meaning it is higher, than the previous analysis. In order to understand this difference, the old and new results are compared step by step. In this analysis, we improved the data reduction to increase the efficiency of the SRN signal. By this improvement, the analysis energy threshold was lowered from 18 MeV down to 16 MeV. Due to the lower energy threshold, the binning used in the energy spectrum fitting was also changed from 18 - 82 MeV, to 16 - 80 MeV, although bin width is exactly the same(4 MeV/bin).

Table-A.1 shows the change of the flux upper limit, step by step.

We started from the SK-I old result of < 1.7 /cm^2/sec, by the Poissonian method. After changing the cut criteria, but still using the same binning and energy threshold of 18 MeV, the 90% confidence level flux limit becomes < 2.3 /cm^2/sec.

Although our new reduction method achieved a better efficiency, the data

	Cut criteria	Binning	Energy threshold	Limit by Gaussian	Limit by Poissonian	αbest (unphys)
SK-I old	OLD	18-82	18MeV	<1.2	—	—
SK-I old +sub-event cut +new cross section	OLD	18-82	18MeV	<1.4	<1.7	0 (-1.1)
New cut criteria	NEW	18-82	18MeV	<2.2	<2.3	0.02
Change binning	NEW	16-80	18MeV	<1.6	<1.8	0. (-0.5)
Lower E threshold	NEW	16-80	16MeV	<1.8	<1.9	0.12

Table A.1: The change of the flux upper limit in SK-I from the previous result is summarized. Starting from the old SK-I result, a new cut criteria is applied at the second line. The binning is changed from 16-80MeV to 18-82MeV(energy threshold is still 18MeV) at the third line. At last, the energy threshold is lowered to 16MeV. The best fit α value is also listed in the right column. The number shown in parentheses is the unphysical best fit value.

increased more than expected due to the efficiency increase. The expected SRN spectrum for the LMA model in SK-I, by old reduction method(Green line), and new reduction method(Red line), are compared. Figure-A.2 shows the increasing rate of data and MC as a function of energy. The data points show the ratio of the number of events between the old and new reduction processes of the SK-I data. The green line shows the new/old ratio of MC events, which means the increase of reduction efficiency. Above 34 MeV, the signal efficiency become slightly worse due to the pion-like event cut and the multi-ring event cut, which were newly added. However, these cuts can also remove background events, making the S/N ratio better than in the old reduction method. As shown in this figure, the efficiency was increased, mainly in the region below 34 MeV. Unfortunately, the increase of data is larger than the efficiency increase, even though the change is within statistical uncertainty. The best fit α value is listed in the right column of Table-A.1. In the old result, the best fit α value was shifted to negative region by the statistical fluctuation. That is the reason why old flux upper limit was smaller than our new limit.

Next, the binning of the fitting spectrum was changed from 18-82 MeV to 16-80 MeV, both with 4 MeV bin widths. The third line shows this binning change, although the energy threshold remained at 18 MeV. By this change, the flux upper limit for energies above 18 MeV becomes > 1.8 /cm^2/sec.

At last, the energy threshold was lowered from 18 MeV to 16 MeV(see bottom line in Table-A.1). After lowering the energy threshold, a flux limit of 1.9 /cm^2/sec was obtained. This effect can be understood by noticing that there is an excess of data below 18 MeV. In our method, the flux upper limit was obtained assuming that all the events, other than invisible μ-e decay and atmospheric ν_e (and $\bar{\nu_e}$), were SRN signals. This method gives a conservative upper

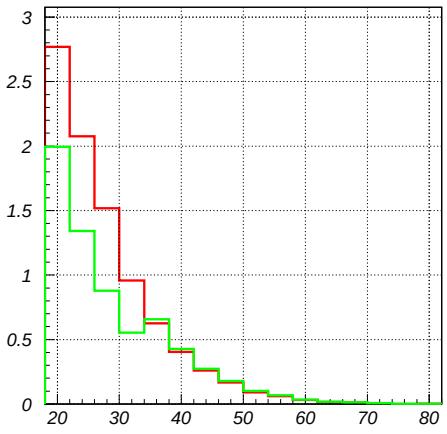

Figure A.1: The expected energy spectrum of SRN events in SK-I with the new/old reduction are compared using the LMA model. The red is the new reduction and the green is the old reduction. Events are increased mainly below 34 MeV, due to the spallation cut difference.

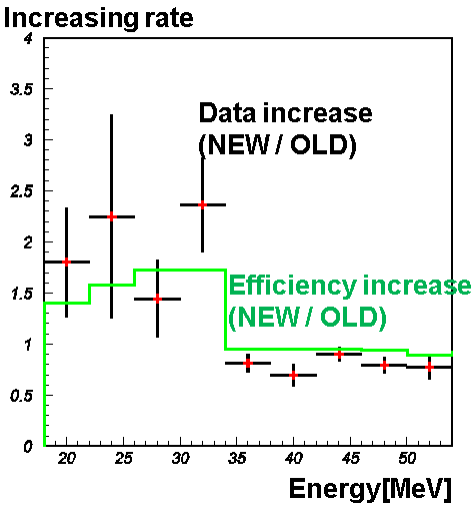

Figure A.2: The increase in number of events from the old analysis method are plotted. The efficiency increase expected from the MC is shown as the green line. The data increase is larger than expected, although it's within statistical error.

limit.

Bibliography

[1] K.S. Hirata *et al.* [The Kamiokande Collaboration], Phys. Rev. Lett. **58**, 1490 (1987).

[2] R.M. Bionta *et al.* [The IMB Collaboration], Phys. Rev. Lett. **58**, 1494 (1987).

[3] K.S. Hirata *et al.* [The Kamiokande Collaboration], Phys. Rev. D **38**, 448 (1988).

[4] C.B. Bratton *et al.* [The IMB Collaboration], Phys. Rev. D **37**, 3361 (1988).

[5] A.M. Hopkins and J.F. Beacom Astrophys. J. **651**, 142 (2006).

[6] H.A. Bethe, G.E. Brown, J.H. Applegate, J.M. Lattimer, Nucl. Phys. A**324**, 487 (1979)

[7] A. Burrows, T.J. Mazurek, Astrophys. J. **259**, 330 (1982)

[8] M. Fukugita, T. Yanagida, *Physics of Neutrinos*, (Springer), ISSN 0172-5998

[9] S. Yamada, J.-T. Janka, H. Suzuki, Astron. Astrophys. **344**, 533 (1999)

[10] T. Totani, K. Sato, H.E. Dalhed, J.R. Wilson, Astrophys. J. **496**, 216 (1998)

[11] A. Burrows *et al.*, Astrophys. J. **539**, 865 (2000)

[12] H. Suzuki, from *Physics and Astrophysics of Neutrinos* p. 763 (1994).

[13] T. Totani *et al.*, Astrophys.J. **496**, 216 (1998).

[14] K. Takahashi, M. Watanabe, and K. Sato, Phys. Lett. B **510**, 189 (2001).

[15] A. Strumia and F. Vissani Phys.Lett. B564 42-54 (2003).

[16] M. Malek [The Super-Kamiokande collaboration] Phys. Rev. Lett 90, 061101 (2003)

[17] G. S. Bisnovatyi-Kogan, S. F. Seidov, Ann. N.Y. Acad. Sci. **422**, 319 (1984).

[18] L. M. Krauss, S. L. Glashow, and D. N. Schramm, Nature **310**, 191 (1984).

[19] S. E. Woosley, J. R. Wilson, and R. Mayle, Astrophys. J. **302**, 19 (1986).

[20] T. Totani and K. Sato, Astropart. Phys. **3**, 367 (1995).

[21] T. Totani, K. Sato, and Y. Yoshii, Astrophys. J. **460**, 303 (1996).

[22] R. A. Malaney, Astropart. Phys. **7**, 125 (1997).

[23] D. H. Hartmann and S. E. Woosley, Astropart. Phys. **7**, 137 (1997).

[24] M. Kaplinghat, G. Steigman, and T. P. Walker, Phys. Rev. D **62**, 043001 (2000).

[25] L. E.Strigari, M. Kaplinghat, G. Steigman, and T. P. Walker, J. Cosm. D **62**, 043001 (2000).

[26] S. Ando, K. Sato, and T. Totani, Astropart. Phys. **18**, 307 (2003).

[27] S. Ando, NNN05 conference in Aussois, France (2005).

[28] S. Horiuchi, J.F. Beacom and E. Dwek, Phys. Rev. D **79**, 083013 (2009).

[29] M. Fukugita and M. Kawasaki Mon. Not Astron. Soc. **340**, L7-L11 (2003).

[30] C. Lunardini, Phys. Rev. Lett. **102**, 231101 (2009).

[31] A.M. Hopkins and J.F. Beacom, Astrophys. J. **651**, 142 (2006).

[32] E. Cappellaro *et al.*, Astron. Astrophys. **430**, 83 (2005).

[33] T.Dahlen *et al.*, Astrophys. J. **613**, 189 (2004)

[34] M.T. Botticella *et al.*, Astron. Astrophys. **479**, 49 (2008)

[35] M.G. Hauser and E.Dwek, Annu. Rev. Astron. Astrophys. **39**, 249 (2001)

[36] S.M. Wilkins, N. Trentham, and A.M. Hopkins, Mon. Not. R. Astron. Soc. **385**, 687 (2008)

[37] Y. Fukuda *et al.* [The Super-Kamiokande Collaboration], Phys. Rev. Lett. **81**, 1562 (1998).

[38] Y. Koshio *et al.* [The Super-Kamiokande Collaboration], Phys.Rev. D73 112001 (2006)

[39] J.P. Cravens *et al.* [The Super-Kamiokande Collaboration], Phys.Rev. D78 032002 (2008)

[40] M. Ikeda, Super-Kamiokande Collaboration meeting (2009)

[41] S. Fukuda *et al.* [The Super-Kamiokande Collaboration], Phys. Rev. Lett. **86**, 5656 (2001).

[42] W. Zhang *et al.* [The Kamiokande Collaboration], Phys. Rev. Lett. **61**, 385 (1988)

[43] K. S. Hirata, *Search for Supernova Neutrinos at Kamiokande-II* PhD thesis, University of Tokyo (1991).

[44] B. Aharmim, *et al.*, Astrophys. J. **653**, 1545 (2006)

[45] M. Aglietta *et al.*, Astropart. Phys. **1**, 1 (1992)

[46] K. Eguchi *et al.*, Phys. Rev. Lett. **92**, 7 (2004)

[47] H. Ikeda *et al.*, Nucl. Inst. and Meth. A **261**, 540 (1987)

[48] T.K. Ohsuka *et al.*, KEK Report 85-10 (1985)

[49] J. George, Ph.D Thesis, University of Washington (1998)

[50] A. Suzuki *et al.*, Nucl. Instr. and Meth. A **329** 299 (1993)

[51] S. Fukuda *et al.* [The Super-Kamiokande Collaboration], Nucl. Instrum. Methods Phys. Res. Sect. A **501**, 418 (2003).

[52] M. Nakahata *et al.* [The Super-Kamiokande Collaboration], Nucl. Instrum. Methods Phys. Res. Sect. A **421**, 113 (1999).

[53] E. Blaufuss *et al.* Nucl. Instrum. Methods Phys. Res. Sect. A **458**, 636 (2001).

[54] M. Shiozawa Ph.D. thesis, University of Tokyo (1999).

[55] E. R. Davies, *Machine Vision: Theory, Algorithms, Practicalities*, Academic Press, San Diego (1997).

[56] C. Michael Lederer and Virginia S. Shirly, *Table of Isotopes*. John Wiley & Sons.

[57] P. Vogel and J. F. Beacom, Phys. Rev. D **60**, 053003 (1999).

[58] S. Michael, Proceedings of 30th International Cosmic Ray Conference, 0213 (2007)

[59] GEANT, CERN Program Library Long Writeup W5013 (1994).

[60] M. Honda *et al.*, Phys. Rev. D **52**, 4985 (1995).

[61] G. Battistoni *et al.*, Astropart.Phys. **19** 269 (2003) [Erratum-ibid. **19** 291 (2003)]. (http://www.mi.infn.it/~battist/neutrino.html)

[62] G. Barr *et al.*, Phys. Rev. D **70**, 0423006 (2004).

[63] A. Morel *et al.*, Limnology and Oceanography **22**, 709 (1977)

[64] G. Mitsuka , Ph.D Thesis, University of Tokyo (2008)

[65] Y. Hayato, Nucl. Phys. Proc. Suppl. **112**, 171 (2002)

[66] H. Ejiri, Phys. Rev. C **48**, 1443 (1993)

[67] K. Kobayashi *et al.*, Nucl-ex / 0604006 (2006)

[68] J.O. Johnson and T.A.—Gabriel, ORNL/TM 10340, (1988)

[69] M. Gluck, E.Reya and A.Vogt, Z. Phys. C**67**, 433 (1995)

[70] J. Kameda, Ph.D Thesis, University of Tokyo (2002).